
The University of Electro-Communications
Tokyo, Japan

# PROPERTIES OF SUPERCURRENT THROUGH A SINGLE COOPER-PAIR TRANSISTOR AND ITS APPLICATION TO PHONON DETECTION

JUTARAT TANAROM

DECEMBER 2021

# Properties of supercurrent through a single Cooper-pair transistor and its application to phonon detection

Jutarat Tanarom

Department of Engineering Science
Graduate school of Informatics and Engineering
The University of Electro-Communications
1-5-1 Chofugaoka, Chofu, Tokyo 182-8585, Japan

A thesis submitted for the degree of
Doctor of Engineering

December 2021

Properties of supercurrent through a single Cooper-pair transistor and its application to phonon detection

単一クーパー対トランジスタの超伝導電流の性質とそのフォノン検出への応用

Jutarat Tanarom

Department of Engineering Science
Graduate school of Informatics and Engineering
The University of Electro-Communications
1-5-1 Chofugaoka, Chofu, Tokyo 182-8585, Japan

APPROVED BY SUPERVISORY COMMITTEE

CHAIRPERSON:

Prof. Hiroshi Shimada

MEMBERS:

Prof. Yoshinao Mizugaki

Prof. Nobuhito Kokubo

Prof. Takeshi Sakai

Prof. Yoshihiro Shimazu

# 単一クーパー対トランジスタの超伝導電流の性質とそのフォノン検出への応用

Jutarat Tanarom

## 概要

超伝導エレクトロニクス素子、とりわけジョセフソン効果に基づいた素子は、基礎的な超伝導研究ならびに量子技術への応用において重要な役割を果たしている。２個のメゾスコピックなジョセフソン接合からなる単一クーパー対トランジスタ（SCPT）は、1990年代に高感度電荷計の一種として発明された素子である。この素子は、超伝導エレクトロニクス素子に電荷の自由度の利用を導入するものと位置づけられる。特に、零バイアス近傍の超伝導電流がゲート電圧により制御され、高速の超伝導スイッチとしても動作可能である。本論文では、このSCPTを実用的なデバイスに応用する可能性を追究した。

第１部では、まずSCPTを他の従来の超伝導回路に組み合わせることを探索するために、共通ゲートをもつ多数のSCPTの並列回路を用いて、SCPT構造により変調可能な超伝導電流のスケーラビリティを研究した。それは、SCPTで変調可能な超伝導電流の大きさが、他の超伝導エレクトロニクス素子の扱う電流の大きさに比べて３桁程度小さいからである。並列回路構造を用いると、扱える最大超伝導電流は、トランジスタ数に応じて増大すること、また、それがゲート電圧によって単一SCPTの場合と同様に変調できることを示した。しかし、変調の相対的な大きさは、トランジスタ数の増大とともに減少した。これらの特性の原因を、ランダムな背景電荷の影響という側面および個々のトランジスタの中央電極に引き起こされる電荷数の量子ゆらぎの観点から定量的に調べ、後者が支配的であることを見いだした。それに基づき、変調度を改善する現実的な方法を議論した。

次に、単一磁束量子回路や超伝導量子干渉素子（SQUID）のような超伝導ループ構造をもつ素子にSCPTを組み合わせることを考えると、応用上ループ状素子にSCPTが挿入された場合の超伝導コヒーレンスが本質的に重要である。そこで、SQUID状のループにSCPTを挿入し、外部印加磁場に対する応答から超伝導コヒーレンスを確認した。また、このような素子での超伝導電流のゲート変調を調べ、電荷ゆらぎの観点から分析した。

本論文の第２部では、SCPTの変調可能な超伝導電流を用いたより具体的

な実用デバイスとして、SCPTを用いたフォノンの高感度検出を提案し、その動作を実験的に確認している。SCPTの電極を構成する超伝導体のエネルギーギャップの２倍以上のエネルギーを持つフォノンは、超伝導電極に照射されると電極中のクーパー対を破壊してボゴリューボフ準粒子を生成する。この準粒子は、SCPTの中央電極にトンネルすると、SCPTのいわゆるパリティを変化させて素子動作に大きな影響を与え、その結果、SCPTの超伝導電流を大きく変化させる。これを利用することで、フォノン検出が可能となる。

論文中では、まず、パリティ効果、別名準粒子汚染、に関して利用可能な理論を用いて、フォノン検出器の定量的な理論モデルを構築した。そして、SCPTをフォノン検出器とし、フォノン源としてSQUIDに磁場を加えた超伝導トンネル接合（STJ）型素子を用いて、フォノンのオンチップ照射・検出実験を行って、SCPT検出器の動作を確認した。そこで得られたフォノンの検出感度は、従来用いられているSTJ型検出器で得られていた感度の1000倍程度と高いものであった。また、この高い検出感度ゆえにプレーナー型配置でのフォノン伝播を検出し、その伝播特性を議論した。

また、このフォノン検出器の応用として、メゾスコピック接合からなる１次元微小ジョセフソン接合列から放出されるフォノンの検出に用いた。同じ条件下のSTJフォノン源に比べ十数倍の強度のフォノン束が検出され、まだ十分に理解されていない接合列中の電荷輸送について、重要な実験的特徴をつかむことができた。接合列中の電荷輸送過程について、従来提唱されているいくつかのモデルを検討し、クーパー対および準粒子の交互トンネルモデルの有用性を議論した。

# *Abstract*

Superconducting electron devices, particularly, those based on the Josephson effect play important roles in the fundamental superconductivity studies as well as the applications in quantum technologies. A single Cooper-pair transistor (SCPT), which is composed of two mesoscopic Josephson junctions, was invented in 1990s as a sensitive electrometer. It introduces the use of the charge degree of freedom into the superconducting electron devices.

In this thesis, a possibility to apply SCPT to practical electronic devices was studied. In the first part, to search for combining the SCPT with other superconducting circuits, the scalability of a supercurrent that can be modulated with an SCPT structure was studied using multiple SCPTs connected in parallel having a common gate electrode because the modulable supercurrent of a SCPT is by orders of magnitude smaller than those in other superconducting electronics circuits. It was found that the magnitude of the maximum supercurrent is scaled up almost linearly with the number of transistors and that it is modulated with the gate voltage as in the case of a single SCPT. The modulability, however, decreases with the increase in the number of transistors. The origin of these characteristics were quantitatively studied and a practically possible method of improving the modulability was also discussed.

When a SCPT is inserted in the superconducting loop such as in the case of rapid single flux quantum circuits and superconducting quantum interference device (SQUID), the coherent property of the supercurrent through the SCPT is essential for such applications. Thus, secondly, the coherence of the supercurrent through the SCPT inserted in a SQUID-like superconducting loop was confirmed experimentally, and also the gate modulation of the supercurrent through the loop was studied and analyzed.

In the second part, as a specific practical application of the modulable supercurrent through a SCPT, a sensitive phonon detection using a SCPT was proposed and experimentally confirmed. A phonon that has an energy greater than twice the superconducting gap of the SCPT electrode can excite quasiparticles in the elec-

trode. The quasiparticle largely influences the magnitude of supercurrent through the SCPT in terms of so called parity effect. The sensitivity of the fabricated detector is approximately 1000 times as large as that in the traditional superconducting tunnel junction detectors. This detection method was also applied to the detection of phonons from another mesoscopic-junction device.

# *Acknowledgements*

First of all, let me express my sincere gratitude to my supervisor Prof. Hiroshi Shimada who supervised my whole Ph.D student life for his full support of my study and research, for his encouragement, knowledge and patience. His guidance helped me in all the time of research and writing of the thesis. I would like to say honestly and simply he is the best Professor for me.

I would like to say thanks to my committee members for oral examination, Prof. Yoshinao Mizugaki, Prof. Nobuhito kokubo, Prof. Takeshi Sakai and Prof. Yoshihiro Shimazu, who shared and gave their ideas related with their distinguished skills and talents in their fields.

I am also grateful to members of group who let me join with them and share an incredible atmosphere and relaxing times. As a foreign student, when I miss my family, they became my second family.

I would like to acknowledge the provider of a scholarship from the Ministry of Higher Education, Science, Research and Innovation, Thailand and everybody who has coded for the LaTeX project for free.

I want to thank all my friends and EVERYONE who ever said anything positive to me, taught me something and drinking. I heard it all, and it meant something.

Lastly I would like to thank my family, particularly Mom, Dad, my younger sister and Ms. Nann Ei Khaing. You never had any doubts about my abilities. I thank you for you constant and unwavering support throughout my life, not just the last five years. I thank you for your constant love, support and encouragement. I look forward to enjoying the rest of my life with you.

Jutarat Tanarom

December 2021

# *List of Publications*

International:

1. "Scalability of supercurrent modulable with single Cooper-pair transistors connected in parallel", Jpn. J. Appl. Phys, **60**, 074003 (2021); Jutarat Tanarom, Yoshinao Mizugaki, and Hiroshi Shimada.

2. "Application of the Cooper-pair transistor as a supercurrent switch for superconducting circuits", International School and Symposium on Nanoscale Transport and phoTonics, ISNTT 2019, November 18-22, Atsugi, Japan; Jutarat Tanarom, and Hiroshi Shimada.

Domestic:

1. "単一クーパー対トランジスタによるフォノン検出 (Detection of phonons with a single Cooper-pair transistor)", the Superconducting Electronics group conference of the Institute of Electronics, Information and Communication Engineers, IEICE-SCE 2021, August 5-6, Online Virtual Meeting; Jutarat Tanarom, Yoshinao Mizugaki, and Hiroshi Shimada.

2. "Study on the Cooper-pair transistor as a fast supercurrent switch", The 81st Japan Society of Applied Physics (JSAP) Autumn Meeting 2020, September 8-11, Online Virtual Meeting ; Jutarat Tanarom, and Hiroshi Shimada.

# Contents

# List of Tables

# List of Figures

# Chapter 1

# Introduction

Superconducting electron devices play important roles in modern fundamental electronics since the discovery of the Josephson effect in 1962 by Brian Josephson and its experimental confirmation in 1963 [1]. Josephson effect is an interesting and fundamentally important phenomenon associated with the macroscopic quantum state and the coherent flow of Cooper pairs. The Superconducting Quantum Interference Device (SQUID) was proposed in 1960s [2]. The rapid single flux quantum (RSFQ) circuits were proposed in 1970s, which are very fast pulse based logic circuits. It's operation frequency can exceed 100 GHz [3]. The first quantum voltage standard based on the Shapiro step producing a voltage of up 1.2 V, which consisted of an array of 1474 Josephson junctions was produced in 1984 [4].

The first materials used for the tunnel Josephson junctions are Sn, In and Pb, as a soft superconductors, with their thermal oxidation for the barrier. In the 1980s, the more grown-up of devices based on "rigid" superconductors as Nb, were introduced combined with Al for $AlO_x$ tunnel barrier. The Al indicates as the perfect solution forming a natural, self-limiting, high-quality, insulating oxide. The Josephson junctions became integrated with thin films, which brought a possibility of their microfabrication.

In more recent years, the nano-fabrication techniques have made controlled transport of single charges in solid-state devices possible. Namely, single-charge devices, including single Cooper-pair devices, were intensively investigated in 1990s and 2000s [5, 6]. Single-charge devices have many important basic applications due

to their ability to manipulate individual electrons and Cooper-pairs. Those devices have been proposed for the practical applications such as memory and logical devices in integrated circuits. It is a famous story that, in those periods, superconducting quantum bits composed of mesoscopic Josephson junctions were invented as one of those devices [7].

In such devices, a single Cooper-pair transistor (SCPT) is a basic one that is analogous to the field effect transistor in structure. The SCPT is a three-terminal superconducting device composed of two ultra-small Josephson junctions in series and a gate electrode that capacitively couples to the electrode between the junctions. The SCPT is operated on the supercurrent branch near zero voltage in the coherent Cooper-pair transport regime and can include several incoherent hybrid quasiparticle/Cooper-pair tunneling processes at higher bias. The gate voltage $V_{\rm g}$ modulates the supercurrent through the device periodically with a period $2e/C_{\rm g}$, where $C_{\rm g}$ is the gate capacitance. It introduces a use of the charge degree of freedom into the superconducting electronic devices. However, the modulation of supercurrent through a SCPT has not been applied to practical devices much. One of the reasons is that the SCPT supercurrent's magnitude, which is typically smaller than 100 nA, is by orders smaller than those of the other superconducting electronics.

In this thesis, we studied possibilities to apply SCPTs to practical electronic devices. In the first part, we studied the possibility to combine the SCPT with other superconducting circuits such as RSFQ circuits and SQUID electronics of which operation needs supercurrents of the magnitude of the order of 100 $\mu$A in general. The scalability of the supercurrent is studied using multiple SCPTs connected in parallel ($1 \leq N \leq 100$, $N$ = the number of SCPTs) having a common gate electrode. It is found that the magnitude of the maximum supercurrent is scaled up almost linearly with the increase in $N$, and the supercurrent is modulated with the gate voltage as in the case for a single SCPT. The modulability of the supercurrent, however, decreases with the increase in $N$. Due to the real structure of the SCPT parallel circuit has capacitive coupling among them, which the main effect of the decreased modulability is caused by the charge-state fluctuations of either islands of the constituent SCPTs. A practically possible method of improving the modulability is also discussed.

When the SCPTs are inserted in the superconducting loop such as in the case of RSFQ circuits, the coherent property of the supercurrent through the SCPT is essential. In order to test the coherence through the SCPT embedded superconducting loop, we fabricated a direct current SQUID in which one of the Josephson junctions was replaced with a SCPT. The magnitude of the maximum supercurrent by way of the SQUID loop was measured by changing the magnetic flux through the loop as well as the gate voltage. The results show the periodic of supercurrent through loop dependence on the applied magnetic field with the supercurrent modulation. Therefore, the supercurrent through the SCPT maintains the superconducting coherence when it modulated with the gate voltage.

In the second part, as a specific practical application of the modulable supercurrent through a SCPT, we proposed a sensitive phonon detection. It is well known that the excitation of quasiparticles in the electrodes influences the Coulomb oscillation characteristics. When phonons of the energy $> 2\Delta$ with $\Delta$ the superconducting gap of the electrode are emitted to the SCPT, the Cooper-pairs in the electrode are broken to quasiparticles, which causes a change in the Coulomb oscillation. This process gives a possibility to use the SCPT as a phonon detector. We fabricated some devices with magnetic-field-applied SQUIDs as phonon emitters and confirmed the operation of phonons detection with a SCPT. The sensitivity of the detector is approximately 1000 times as large as that in the traditional superconducting tunnel junctions (STJ) detectors.

The developed phonon detector is applied to detect a strong phonon flux from a one-dimensional array of mesoscopic Josephson junctions and its transport processes are discussed.

## 1.1 Brief outline of thesis

The main topics of the chapters of this thesis are as follows: The theoretical background on Josephson effect, single Cooper-pair transistor and the derived structures from a Josephson junction are described in chapter 2. The chapter 3 explains the sample fabrication techniques and the measuring system. The scalability of supercurrent modulable with single Cooper-pair transistors connected in parallel

with their experimental results are described in chapter 4. The coherence of the supercurrent through a single Cooper-pair transistor and gate modulation of the supercurrent in a dc SQUID loop is discussed in chapter 5. Then, the subsequent two chapters compose the latter part of my research. The chapter 6 proposes to detect phonons by a SCPT on the basis of the parity effect associated with nonequilibrium quasiparticles and presents a quantitative model of the detector and confirmed its operation experimentally. It is found that the sensitivity of the SCPT detector was about 1000 times higher than that of traditional superconducting tunnel junction (STJ) detectors. Chapter 7 focuses on the transport process in a one-dimensional array of mesoscopic Josephson junctions through the detection of strong phonon flux with the SCPT detector.

# Chapter 2

# Single Cooper-pair transistor and background theory

This chapter presents an overview about the single Cooper-pair transistor, SCPT, and superconducting circuits. The tunneling of Cooper pairs between two superconductor is referred to as the Josephson effect. To understand the physical processes in the SCPT, the understanding of the basic physics in a fundamental unit of a single Josephson junction is needed. For device application, Josephson Junctions are used in a variety of superconductive electronic technologies. Here, some devices related to this work are also explained.

## 2.1 Josephson effect

The two superconductors separated by a thin insulating barrier is so-called a Josephson junction. The overlap of the wave functions of Cooper pair within the tunnel barrier plays an important role. In 1962, B. D. Josephson [1] suggested that it should be possible for electron pairs to tunnel between closely spaced superconductors even with no potential difference. The first experimental confirmation for the effect was made by Anderson and Rowell [8] in 1964.

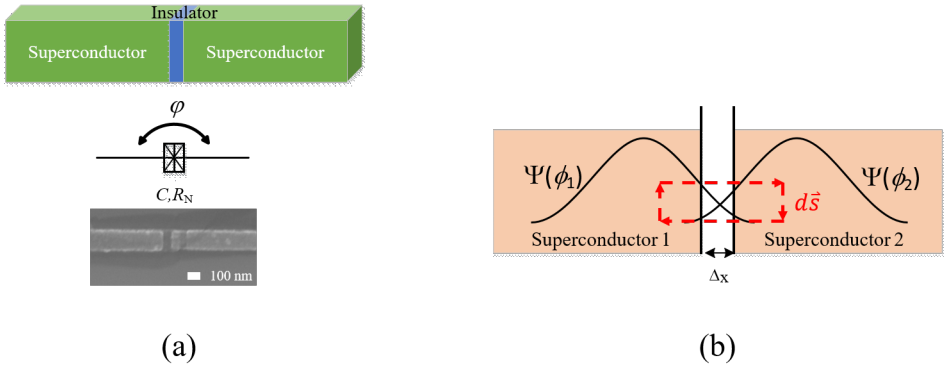


**Figure 2.1:** (a) Schematic and a symbol for the Josephson junction with scanning electron micrograph of a practical Josephson junction. (b) Schematic of overlapping macroscopic wavefunctions of superconductors across a Josephson junction. $\Delta x$ is the tunnel barrier thickness.

## Josephson equation

Consider a bulk superconductor at zero temperature. All the Cooper pairs occupy the same energy state which is separated from all higher states by the superconducting gap. The Cooper pairs form a condensate described by a wave function. It reads

$$\Psi(r) = |\Psi(r)|\, e^{i\phi(r)}, \tag{2.1}$$

where $\phi(r)$ is the microscopic condensate phase. The schematic representation of a Josephson junction is shown in Fig. 2.1. The supercurrent of Cooper pairs across the tunnel barrier follows current-phase relationship by the Schrödinger equation [9].

Josephson predicted that a flowing current through a junction would be proportional to the sine of the difference phase between the two condensates $\Psi_1(r) = |\Psi_1(r)|\, e^{i\phi_1(r)}$ and $\Psi_2(r) = |\Psi_2(r)|\, e^{i\phi_2(r)}$ (1 and 2 are the numbers assigned to the superconducting electrodes on both sides of the junction), as

$$I_\mathrm{s} = I_\mathrm{c} \sin(\varphi), \tag{2.2}$$

where the critical current $I_\mathrm{c}$ is the maximum supercurrent that can flow through the junction, and $\varphi$ the gauge invariant phase difference across the barrier $\varphi = \phi_2 - \phi_1 - \frac{2\pi}{\Phi_0} \int_1^2 \vec{A} \cdot d\vec{s}$. Here $\phi_1$ and $\phi_2$ are the quantum mechanical phases of both superconducting electrodes and the integration of the vector potential $\vec{A}$ which is

from one electrode of the weak link to the other one. The integral is to be taken across the junction from superconductor 1 to superconductor 2. The temperature dependence of the critical current is followed by Ambegaokar-Baratoff formula [10] for BCS superconductor.

$$I_{\mathrm{c}} = \frac{\pi\Delta(T)}{2eR_{\mathrm{N}}} \tanh\left(\frac{\Delta(T)}{2k_{\mathrm{B}}T}\right), \tag{2.3}$$

where $k_{\mathrm{B}}$ is the Boltzmann constant and $R_{\mathrm{N}}$ is the junction resistance in normal state. At $T \ll T_{\mathrm{c}}$, the critical current can be approximated to

$$I_{\mathrm{c}}R_{\mathrm{N}} = \frac{\pi\Delta(0)}{2e}. \tag{2.4}$$

The second equation of Josephson relation describes the voltage drop over the barrier when the phase difference $\varphi$ vary with time $t$. It reads

$$\frac{d\varphi}{dt} = \frac{2e}{\hbar}V = \frac{2\pi}{\Phi_0}V. \tag{2.5}$$

Using the derivation of Josephson current (eq. 2.2) with respect to $t$ and the second Josephson relation (eq. 2.5), one obtains

$$\frac{dI_{\mathrm{s}}}{dt} = I_{\mathrm{c}}\frac{2\pi}{\Phi_0}V\cos\varphi. \tag{2.6}$$

Reminding the induction law, $dI/dV = V/L$, one can define the non-linear inductance of Josephson junction $L_{\mathrm{J}}$ as

$$L_{\mathrm{J}} = \frac{\Phi_0}{2\pi I_0 \cos\varphi}. \tag{2.7}$$

Note that the inductance at zero bias is $L_{\mathrm{J0}} = \Phi_0/2\pi I_{\mathrm{c}}$.

The total energy of the Josephson junction can be calculated by using the relations of 2.2 and 2.5. The energy stored in the junction can be found by integrating the work done by a current source to change the phase, $(\int I_{\mathrm{c}}V dt) = \int I_{\mathrm{c}}(\hbar/2e)d\varphi)$. The potential energy in the Josephson junction is

$$U_\phi = -\frac{I_{\mathrm{c}}\hbar}{2e}\cos\varphi + \text{const.} = -E_J\cos\varphi + \text{const}, \tag{2.8}$$

where $E_{\mathrm{J}} = I_{\mathrm{c}}\hbar/2e$ is the minimum energy stored in the junction when the phase difference across the junction $\varphi$ is zero. This minimum energy is often referred to as the Josephson energy or Josephson coupling energy.

The charging energy $E_{\mathrm{c}}$ is related to the energy stored in the capacitance, $C$, composed of two overlapping superconducting electrodes. This electrostatic energy occurs from $N$ Cooper pairs located on each superconducting electrode as expressed

$$E_{\mathrm{c}}^{\mathrm{N}} = \frac{1}{2}CV^2 = \frac{1}{2}C\left(\frac{2eN}{C}\right)^2 = 4N^2E_{\mathrm{c}}, \tag{2.9}$$

where $E_{\mathrm{c}}{=}e^2/2C$ is the charging energy of a single electron. The added energy for one more Cooper pair is $\Delta E_{\mathrm{c}} \equiv E_{\mathrm{c}}^{N+1} + E_{\mathrm{c}}^{N} = 4(2N+1)E_{\mathrm{c}}$.

## Josephson Hamiltonian

The Josephson Hamiltonian in term of the Josephson equations can be expressed as

$$H = \frac{Q^2}{2C} - E_{\mathrm{J}}\cos\varphi. \tag{2.10}$$

where $Q = CV$ is the charge stored by the junction of capacitance $C$. The essential degrees of freedom in the quantum Hamiltonian are the excess number of Cooper-pairs $n$, and the phase difference $\varphi$ across the junction. The $n$ and $\varphi$ are conjugate to each other with the commutation relation

$$[\varphi, n] = i \tag{2.11}$$

and

$$[\varphi, Q] = 2ei \tag{2.12}$$

Thus, the Hamiltonian can be rewritten as

$$H = 4E_{\mathrm{c}}n^2 - E_{\mathrm{J}}\cos\varphi \tag{2.13}$$

Accordingly, the quantum Josephson Hamiltonian is expressed in terms of the phase difference as

$$\hat{H} = -4E_{\mathrm{C}}\frac{\partial^2}{\partial\varphi^2} - E_{\mathrm{J}}\cos\varphi, \quad \hat{Q} = -2ei\frac{\partial}{\partial\varphi} \tag{2.14}$$

The situation is the same as that of a particle in a periodic potential. Thus, the energy eigenvalues form a energy band structure. The energy band of a single Josephson junction was first calculated by Likharev and Zorin as in Fig. 2.2[11]. The quantity in the horizontal axis means "quasicharge" in contrast to the "crystal momentum" in the case of a particle in a periodic potential.

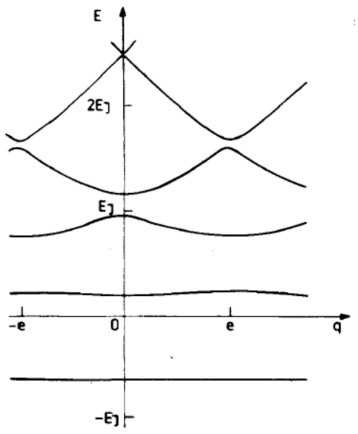


**Figure 2.2:** The energy band of the single Josephson junction for the ratio $E_{\mathrm{c}}/E_{\mathrm{J}} = 0.1$ [11].

## 2.2 Single Cooper-pair Transistor (SCPT)

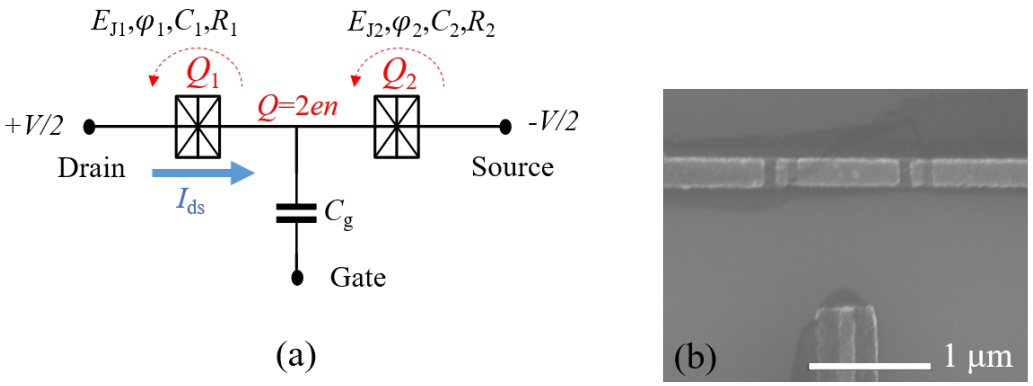


**Figure 2.3:** (a) Simplified SCPT schematic. (b) Scanning electron micrograph of a practical SCPT.

The schematic of a SCPT shown in Fig. 2.3 comprises two small Josephson junctions connected in series. In the figure, $\varphi_1$ and $\varphi_2$ are phase differences across two junctions 1 and 2, $C_1$ and $C_2$ are their capacitances, $E_{\mathrm{J1}}$ and $E_{\mathrm{J2}}$ are their Josephson coupling energies, $Q_1$ and $Q_2$ are charges which pass across two junctions, and $C_{\mathrm{g}}$ denotes a gate capacitance. A gate voltage $V_{\mathrm{g}}$ polarizes the central island between the junctions with the charge $Q_0 = C_{\mathrm{g}}V_{\mathrm{g}}$. The total phase difference $\varphi = \varphi_1 + \varphi_2$ over two junctions is fixed by the superconducting lead electrodes, while the internal variables are the island charge $Q = Q_1 - Q_2$ and semidifference phase $\theta = (\varphi_1 - \varphi_2)/2$. The Josephson coupling energy characterizes the strength of the phase correlation between two superconducting electrodes of the junction, are $E_{\mathrm{J1}} = I_{\mathrm{c1}}(h/4\pi e)$ and $E_{\mathrm{J2}} = I_{\mathrm{c2}}(h/4\pi e)$, where $I_{\mathrm{c1}}$ and $I_{\mathrm{c1}}$ are the critical current of the individual junctions. The charging energy of a Cooper pair on the island, $E_{\mathrm{c}} = (2e)^2/2C_\Sigma$, characterizes the correlation in the number of Cooper-pair tunneling with the total island capacitance, $C_\Sigma = C_1 + C_2 + C_{\mathrm{g}}$.

## Basic tunnel conditions in the SCPT

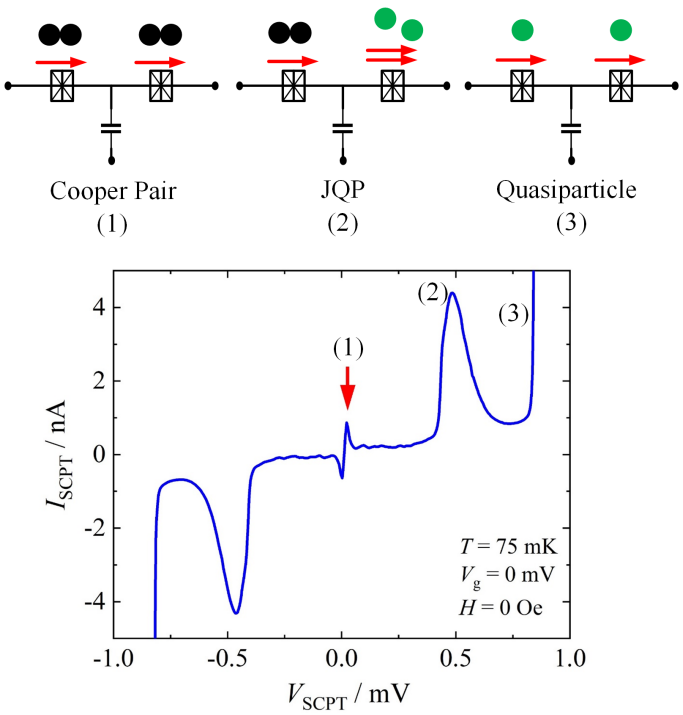


**Figure 2.4:** $I - V$ characteristic of SCPT, and illustrations of typical tunneling processes: (1) Cooper-pair tunneling, (2) Josephson quasiparticle cycle, and (3) sequential quasiparticle tunneling.

The current flows in the SCPT through the series of tunnel junctions bring charges from the drain onto the island, and then to the source lead. In the normal state, this tunneling is simply treated with first-order perturbation theory. In the superconducting state, this tunneling occurs through a variety of different combinations of Cooper pair and quasiparticle tunneling events. The basic $I$–$V$ characteristics of SCPT are shown in Fig. 2.4. First, a supercurrent flows near zero voltage, characterized by a small peak. This is due to a tunnel process with only Cooper pairs. When the voltage is further increased, a Josephson quasiparticle (JQP) cycle [12] occurs. JQP cycle is a situation where the Cooper pair is coherently vibrating at one junction (junction 1), and when one quasiparticle tunnels at the other junction (junction 2), the Cooper pair tunnels in the direction in which the vibration is stopped. Then another quasiparticle tunnels at junction 2 again and the charge state returns to the original one. Therefore, in the entire cycle, one Cooper pair tunnels through one junction and two quasiparticles tunnel through the other junction. When the voltage is further increased, sequential quasiparticle tunneling occurs in the portion where the current rapidly increases with respect to the voltage. This is a tunnel process involving only quasiparticles. Also, by applying a gate voltage, the above-mentioned characteristics can be changed periodically.

## Tunneling processes at low bias

Below the JQP threshold, there are many higher-order tunneling processes resolved. P. Hadley et al. indicated an existence of $3e$ process in 1998 [13]. Those processes can be specified in differential conductance characteristics of the SCPT such as measured by Billangeon et al. [14] and quoted in Fig. 2.5. In the figure, the bright lines corresponds to the thresholds for certain higher-order tunneling processes. The JQP threshold is 485 $\mu$eV, the bright points at approximately 0.3 mV corresponds to the double JQP cycle [14]. Between 0.3 mV to 0.35 mV, weak 3e threshold lines are visible [13]. The $e$ periodic structure just above around $V_{\mathrm{B}}$ = 0.1 mV are considered to be higher order processes involving nonequilibrium quasiparticles [14].

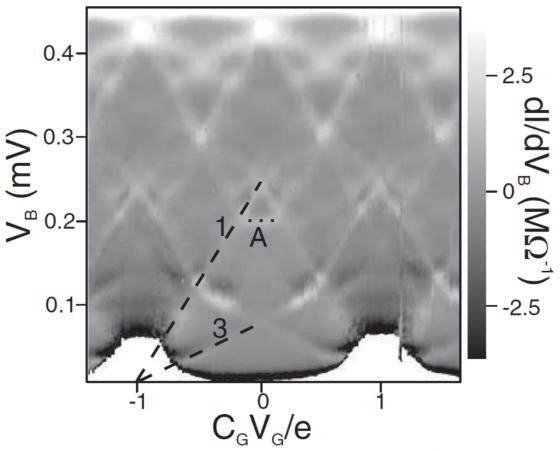


**Figure 2.5:** Differential conductance characteristics of a SCPT bellow the bias for the JQP cycle measured in ref. [14]. The white areas near the horizontal axis correspond to the $2e$ periodic supercurrent. Just above around $V_B = 0.1$ mV, there are $e$ periodic structures. They are considered higher order processes involving nonequilibrium quasiparticles [14, 15].

## Quantum Description of a SCPT and its supercurrent

At zero bias voltage, the Hamiltonian for the SCPT is expressed as

$$H = H_{\mathrm{CB}} + H_{\mathrm{J1}} + H_{\mathrm{J2}} + H_{\mathrm{qp}}. \tag{2.15}$$

The first term, $H_{\mathrm{CB}}$, is the electrostatic Hamiltonian given by

$$H_{\mathrm{CB}} = 4E_{\mathrm{c}}(n - n_{\mathrm{g}})^2, \tag{2.16}$$

where, $n$ is a number of excess Cooper pairs in the island and $n_g = C_{\mathrm{g}}V_{\mathrm{g}}/2e$ is the charge on the gate capacitance induced by the gate voltage $V_{\mathrm{g}}$.

The second term, $H_{\mathrm{J1}}$ and $H_{\mathrm{J2}}$ are the Josephson coupling Hamiltonian for each junction given by

$$H_{\mathrm{J1}} = -E_{\mathrm{J1}} \cos\varphi_1, \quad H_{\mathrm{J2}} = -E_{\mathrm{J2}} \cos\varphi_2, \tag{2.17}$$

It is convenient to have a change of variables from $\varphi_1$ and $\varphi_2$ to $\varphi$ and $\theta$. Then, the total Josephson Hamiltonian is given by

$$H_{\mathrm{J}} = H_{\mathrm{J1}} + H_{\mathrm{J2}} = -E_{\mathrm{J}}(\varphi) \cos(\theta + \chi) \tag{2.18}$$

with,

$$E_{\mathrm{J}}(\varphi) = \sqrt{E_{\mathrm{J1}}^2 + E_{\mathrm{J2}}^2 + 2E_{\mathrm{J1}}E_{\mathrm{J2}}\cos\varphi}, \qquad \chi = \tan^{-1}\left[\frac{(E_{\mathrm{J1}} - E_{\mathrm{J2}})}{(E_{\mathrm{J1}} + E_{\mathrm{J2}})}\tan\frac{\varphi}{2}\right]. \quad (2.19)$$

Assuming that the properties of two junctions are identical, $E_{\mathrm{J1}} = E_{\mathrm{J2}} = E_{\mathrm{J}}$, the total Josephson Hamiltonian of the SCPT becomes

$$H_{\mathrm{J}} = -2E_{\mathrm{J}}\cos\frac{\varphi}{2}\cos\theta. \quad (2.20)$$

The third term of the Hamiltonian for the SCPT corresponds to the quasiparticle excitations in the leads and the island. This Hamiltonian can be expressed

$$H_{\mathrm{qp}} = \sum_i \varepsilon_i^{\mathrm{qp}}\gamma_i^{\dagger}\gamma_i, \quad (2.21)$$

where $\gamma_i^{\dagger}$ and $\gamma_i$ are operators for creation and annihilation of a quasiparticle [16] and $\varepsilon_i^{\mathrm{qp}}$ is the quasiparticle energy. This term can be ignored when all electrons in the superconductor are paired (i.e. no quasiparticles at $T$=0). In this case, the Hamiltonian has the same form as that of a single junction,

$$H = 4E_{\mathrm{c}}(n - n_{\mathrm{g}})^2 - E_{\mathrm{J}}(\varphi)\cos(\theta + \chi). \quad (2.22)$$

With the basis of island charge state $\mid n\rangle$, which corresponds to $n$ excess Cooper pairs in the island, and in the case where three charge states are considered, for example, the matrix of the Hamiltonian for the island states $|\text{-}1\rangle$, $|0\rangle$ and $|1\rangle$, is obtained:

$$H = \begin{bmatrix} 4E_{\mathrm{c}}(-1 - n_{\mathrm{g}})^2 & -\frac{E_{\mathrm{J}}(\varphi)}{2} & 0 \\ -\frac{E_{\mathrm{J}}(\varphi)}{2} & 4E_{\mathrm{c}}(-n_{\mathrm{g}})^2 & -\frac{E_{\mathrm{J}}(\varphi)}{2} \\ 0 & -\frac{E_{\mathrm{J}}(\varphi)}{2} & 4E_{\mathrm{c}}(1 - n_{\mathrm{g}})^2 \end{bmatrix} \quad (2.23)$$

The eigenvalues, $\varepsilon_i$, for this matrix represent the energy bands and are functions of $n_{\mathrm{g}}$ and total phase difference $\varphi$. The energy-phase relation in the ground band for the SCPT is the equivalent of the -$E_{\mathrm{J}}\cos\varphi$ relation for the single Josephson junction. The superconducting state of the SCPT corresponds to a static solution for $\varphi$. The charge is easily localized and the corresponding external phase fluctuations become

large when the SCPT has a weak effective Josephson energy and the ratio of $E_J/E_c$ is small. Figure 2.6 shows the eigenenergies (energy surfaces over the $\varphi - n_g$ plane) of a SCPT calculated with the three band model with $E_J/E_c = 0.6$.

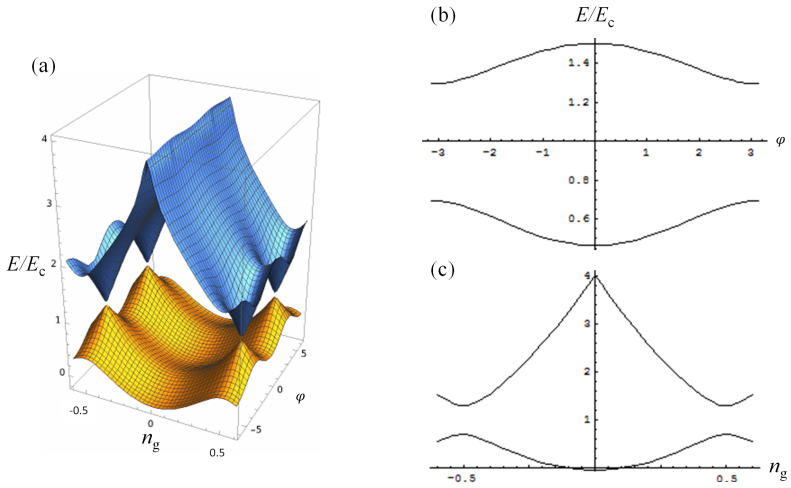


**Figure 2.6:** A 3D plot of the energy bands of the ground state (yellow) and the first excited state (blue) as functions of $\varphi$ and $n_g$ calculated for $E_J/E_c = 0.6$. The cross sectional plots of the energy bands as functions of $\varphi$ (b) and $n_g$ (c), respectively.

## Critical current modulation of a SCPT

The supercurrent $I_s$ of the SCPT can be determined from the ground state energy surface $\varepsilon_0(n_g, \varphi)$ with the relation $(2e/\hbar)\frac{\partial \epsilon_0}{\partial \varphi}$.

Zorin calculated the gate modulation of supercurrent directly by solving eq. (2.22) using Mathieu functions and using the following equation,

$$I_s(\varphi, n_g) = I_s^0 \langle \cos \eta \rangle = I_s^0 \frac{\partial \varepsilon}{\partial \lambda} \mid_{\lambda = E_J(\varphi)/E_c} \tag{2.24}$$

with $I_s^0 = (2e/\hbar)(E_J^2/E_J(\varphi)) \sin\theta$, $E_J(\varphi) = 2E_J \cos(\varphi/2)$ and $\eta = \theta + \chi$. $I_s^0$ stands for the usual $(E_J(\varphi)/E_C \to \infty)$ supercurrent of a double junction while the $\langle \cos \eta \rangle$ describes its partial suppression by charging effect. Figure 2.7 shows the characteristic of the calculated supercurrent by Zorin for several ratios of $E_J/E_c$ [17]. The calculated currents are $2e$ periodic in the applied gate charge, $C_g V_g = 2en_g$, that is the result of the Josephson coupling of Cooper pair charge state. With decreasing $E_J/E_c$ ratio the quantum fluctuations of the phase increase and the fluctuations of the charge decrease. The magnitude of the supercurrent modulation with the gate

voltage is almost the total maximum supercurrent value at lower $E_J/E_c$ ratio value. The critical current of the transistor is defined to be the maximum theoretical supercurrent that can flow through the transistor. In spite of a theoretical prediction, experimentally observed critical currents were smaller than that value [18].

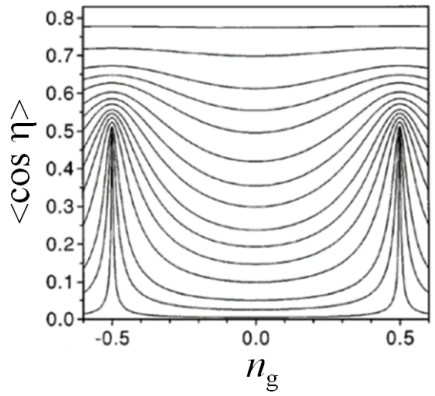


**Figure 2.7:** A plot of the suppression factor $\langle \cos \eta \rangle$ of the Josephson current due to the charging effect versus $n_g$ for $E_J/E_c$ = 0.02, 0.1, 0.2, 0.4, 0.6, 0.8, 1, 1.3, 1.6, 2, 2.6, 3.2, 4, 6, and 10 (from bottom to top) [17]

## Nonequilibrium quasiparticles in the SCPT

In the SCPT, coherent charge transport is temporarily halted while a quasiparticle is present on the SCPT island, which is called "quasiparticle poisoning". It is also called a "parity effect" because the existence of a quasiparticle on the island changes the even-odd parity of the number of electrons in the island. A model of quasiparticles poisoning was proposed by J. Aumentado [19].

A quasiparticle poisoning came from two possible sources; one is thermally induced equilibrium quasiparticles, of which density, $n_{qp}$, is expressed as [20]

$$n_{qp} = D(\epsilon_F)\sqrt{2\pi\Delta k_B T}\exp(-\Delta/k_B T). \tag{2.25}$$

$D(\epsilon_F)$ is density of state at the Fermi energy of the superconducting electrode and $\Delta$ is the superconducting gap energy. The other is nonequilibrium quasiparticles induced by unknown sources.

Figure 2.8 (a) shows the three possible quasiparticle states of the SCPT. The 0 state, the lowest energy state, assumes no quasiparticles on the island or leads of

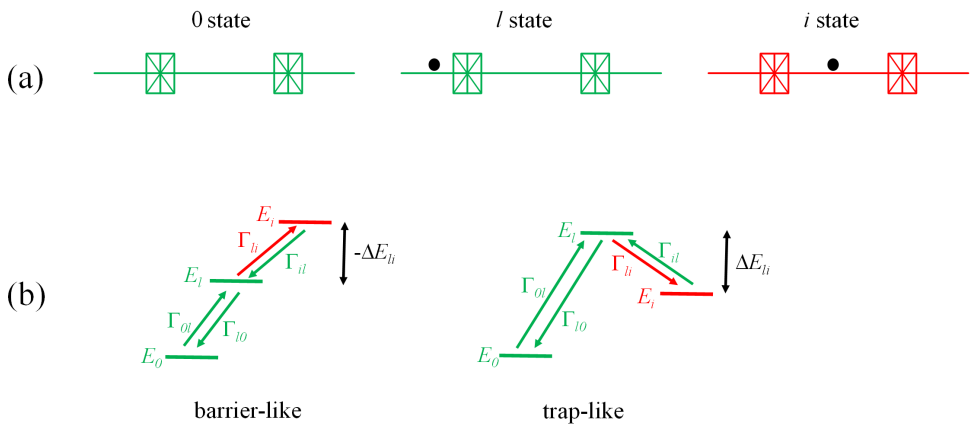


**Figure 2.8:** Model of non-equilibrium quasiparticle poisoning [21]. (a) Three possible quasiparticle states of the SCPT. (b) The energy cost of an extra quasiparticle tunnelling onto the island, the positive energy looks like a trap and the negative energy looks like a barrier.

the SCPT, with corresponding energy $\varepsilon_0(n_g, \varphi)$. The $l$ state assumes a quasiparticle on the lead with energy $E_l(n_g) = \varepsilon_0(n_g, \varphi) + \Delta_l$. The 0 and $l$ state are defined in even parity. The $i$ state assumes a quasiparticle on the island with energy $E_i(n_g) = \varepsilon_0(n_g + 1, \varphi) + \Delta_i$. This state is odd parity. Here, $\Delta_l$ and $\Delta_i$ are superconducting gap in lead and island, respectively. The quasiparticle may rapidly tunnel out of the island, depending on the energy of the poisoned state on the island. If $E_l > E_i$, the quasiparticle may stay on the island for a long time, and it will need to be activated out of the island's potential well before the SCPT can return to its even state.

The presence of a quasiparticle in the SCPT is related with two energies. The first is the appearance of a quasiparticle in the state of leads ($0 \to l$), which adds a constant energy of $\Delta_l$ to the system. The system's second critical energy, $\Delta E_{li} = E_l - E_i$, decides whether the island acts as a barrier or as a potential well for the quasiparticle in the leads. The energy change for parity switching, $l$ state to $i$ state, transitions is

$$\Delta E_{li}(n_g, \theta) \equiv E_l - E_i = \varepsilon_0(n_g, \varphi) - \varepsilon_1(n_g, \varphi) + \delta\Delta, \tag{2.26}$$

where $\delta\Delta \equiv \Delta_l - \Delta_i$. This energy $\Delta E_{li}$ is a good predictor of how a quasiparticle would behave when it gets close to the SCPT island. At $T = 0$, the sigh of this quantity determined what state it is in, i.e, $\mathrm{sgn}(\Delta E_{li}) = +1$ being even parity, as well

as, $\mathrm{sgn}(\Delta E_{li}) = -1$ being odd parity. The quasiparticles poisoning is suppressed, when $\Delta E_{li} < 0$, quasiparticles in the leads are prevented from reaching the island by a barrier and the parity state is even. The parity state is odd when $\Delta E_{li} > 0$, quasiparticles will readily tunnel onto the island and can become trapped there.

The transition rates of a quasiparticle tunneling between barrier-like and trap-like configurations of levels (Fig. 2.8(b)) can be used to calculate the probability of the SCPT in even and odd states. The transition rate of quasiparticles tunnel are defined as $\Gamma_{0l(l0)}$ for $0 \to l$ $(l \to 0)$ states, and $\Gamma_{li(il)}$ for $l \to i$ $(i \to l)$ states. The probability of the even state $(P_e = P_0 + P_l)$ and the odd state $(P_o = P_i)$ in steady state can be written as [19]

$$\frac{P_e}{P_o} = \left(1 + \frac{\Gamma_{l0}}{\Gamma_{0l}}\right) \frac{\Gamma_{il}}{\Gamma_{li}} = \left(1 + \frac{\Gamma_{l0}}{\Gamma_{0l}}\right) e^{-\Delta E_{li}/kT}. \tag{2.27}$$

The probability of the SCPT in an even state can be expressed in terms of the even and odd state lifetimes, $t_e$ and $t_o$ as [20]

$$P_e = \frac{t_e}{t_e + t_o}. \tag{2.28}$$

## Application of SCPT

The SCPT is applied to the microwave spectroscopy in 2012 [22] and to a sensitive electrometer which could be used to measure the delicate quantum superpositions of charge states in a superconducting island connected by a tunnel junction to a superconductor with a sensitivity $10^{-7}e/\sqrt{\mathrm{Hz}}$ in 2019 [23]. The SCPT has been extensively researched in terms of its applicability to quantum computing [7, 24, 25].

## 2.3 Josephson-effect related circuits

### 2.3.1 SQUID

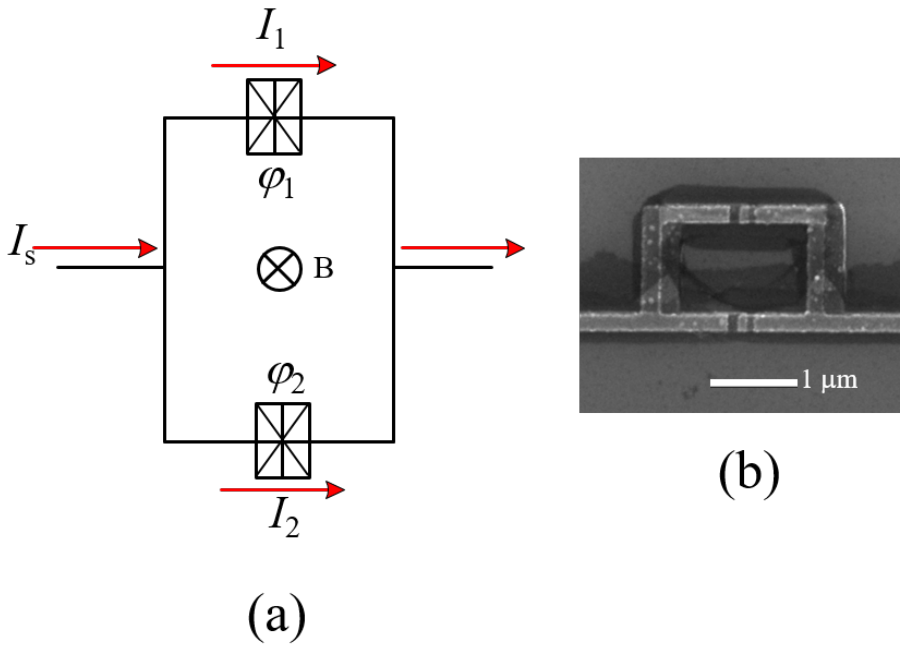


**Figure 2.9:** (a) Schematic of a dc-SQUID: The applied current splits into two parts $I_1$ and $I_2$. In the presence of magnetic field, the phase difference for both junctions is $\varphi_1$ and $\varphi_2$, respectively., (b) Scanning electron micrograph of a practical dc-SQUID.

A direct current superconducting quantum interference device (dc-SQUID) consists of a superconducting loop interrupted by two Josephson junctions connected in parallel as shown in Fig. 2.9. The SQUID is used as a practical, very sensitive magnetometer.

The physics of a dc SQUID can be considered as the phase interference of the wave functions in its two branches. To make the description for the dc-SQUID simple, we assume both junctions are identical and small compared to the size of the loop. Moreover, both junctions have the same critical current $I_c$ and effects of magnetic flux penetrating the junctions can be neglected. The SQUID is biased with a dc current, which splits into two current $I_1$ and $I_2$ through the Josephson junction 1 and 2, respectively. The phase differences across the junctions 1 and 2 are denoted by $\varphi_1$ and $\varphi_2$, respectively.

According to Kirchhoff's law. the bias current must be equal to the sum of $I_1$

and $I_2$. The current yields

$$I_s = I_c[\sin\varphi_1 + \sin\varphi_2] = 2I_c \cos\left(\frac{\varphi_1 - \varphi_2}{2}\right) \sin\left(\varphi_2 + \frac{\varphi_1 - \varphi_2}{2}\right) \tag{2.29}$$

The gauge invariant phase difference across the Josephson junction can be express as $\varphi_1 - \varphi_2 = 2\pi n + \pi\Phi/\Phi_0$, $\Phi_0 = h/2e$ is the superconducting flux quantum. One obtains

$$I_s = 2I_c \cos\left(\pi\frac{\Phi}{\Phi_0}\right) \sin\left(\varphi_2 + \pi\frac{\Phi}{\Phi_0}\right) \tag{2.30}$$

The flux in the contour is $\Phi = \Phi_{ext} + LI_{cir}$, the circulating current is given by $I_{cir} = (I_1 - I_2)/2$ and $L$ is the inductance of the loop. The total flux can then be written as

$$\Phi = \Phi_{ext} + \frac{LI_c}{2} \sin\left(\pi\frac{\Phi}{\Phi_0}\right) \cos\left(\varphi_2 + \pi\frac{\Phi}{\Phi_0}\right) \tag{2.31}$$

For a bias current below the critical current, the phase $\varphi_2 + \pi(\Phi/\Phi_0)$ will adjust. In this case $\Phi = \Phi_{ext}$, the inductance of SQUID can be ignore. The maximum current is obtained for $\sin(\varphi_2 + \pi(\Phi/\Phi_0)) = \pm 1$,

$$I_s^{max} = 2I_c \left|\cos\pi\frac{\Phi}{\Phi_0}\right|. \tag{2.32}$$

In Fig. 2.10, the critical current is a periodic function of the external magnetic flux with the period given by the flux quantum $\Phi_0$. Maxima in critical current occur whenever $\Phi_{ext} = n\Phi_0$, while zero for $\Phi_{ext} = (n + 1/2)\Phi_0$. The modulation depth $\Delta I_{max}$ is given by $2I_s^{max}$.

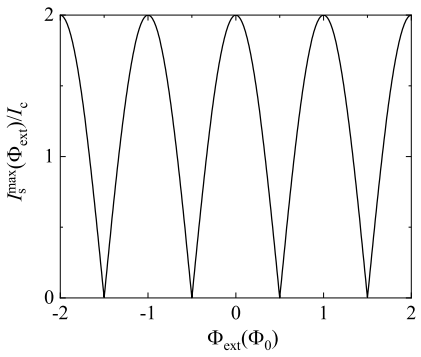


**Figure 2.10:** Critical current $I_s^{max}$ of a DC SQUID versus external magnetic flux in units of the flux quantum for negligible SQUID inductance.

The Josephson coupling energy $E_{\mathrm{J}}$ relates proportionally with the supercurrent $I_{\mathrm{s}}^{\max}$. $E_{\mathrm{J}}$ can be modulated periodically by applying magnetic field $\Phi_{\mathrm{ext}}$ perpendicular to its loop area and is given as

$$E_{\mathrm{J}}(B) = E_{\mathrm{J}} \left|\cos(\pi\Phi/\Phi_0)\right| = E_{\mathrm{J}} \left|\cos(\pi B A_{\mathrm{loop}}/\Phi_0)\right|, \tag{2.33}$$

$A_{\mathrm{loop}}$ is area of the dc-SQUID loop.

### 2.3.2 Overdamped junction and RSFQ

#### Overdamped junction

The resistively and capacitively shunted junction (RCSJ) model of a Josephson junction (as shown in Fig. 2.11 (a)) combines the junction with a shunt resistance $R$ and capacitance $C$. The $R$ explains the dissipative voltage mode and $C$ explains the geometric capacitance between two superconductor electrodes. The bias current $I_{\mathrm{b}}$ is equal to the sum of the fractions of the current flowing through the different paths of Josephson junction and is presented by

$$I_{\mathrm{b}} = I_{\mathrm{c}} \sin\varphi + \frac{V}{R} + C\frac{dV}{dt}, \tag{2.34}$$

where $V$ is the voltage across the Josephson junction. By substituting $V$ of the second Josephson relation equation, one can derive the dynamic equation for the phase.

$$\ddot{\varphi} + \frac{1}{RC}\dot{\varphi} + \omega_{\mathrm{p}}^2(\sin\varphi - \frac{I_{\mathrm{b}}}{I_{\mathrm{c}}}) = 0, \tag{2.35}$$

where $\omega_{\mathrm{p}} = (2eI_{\mathrm{c}}/\hbar C)^{1/2}$ is the plasma frequency for a Josephson junction. The differential equation can be rewritten in term of the potential energy $U(\varphi) = -E_{\mathrm{J}}\cos\varphi - (\hbar/2e)I_{\mathrm{b}}\varphi$. The equation is similar to the equation of motion for a particle of mass $m$ moving in one dimension and affected by a potential and damping. The mass of the phase particle $m$ is $m = (\hbar/2e)^2 C$ and the damping is inversely proportional to $R$, in term of $(\hbar/2e)^2/R$.

$$\left(\frac{\hbar}{2e}\right)^2 C\ddot{\varphi} + \left(\frac{\hbar}{2e}\right)^2 \frac{1}{R}\dot{\varphi} + \frac{\partial U(\varphi)}{\partial(\varphi)} = 0 \tag{2.36}$$

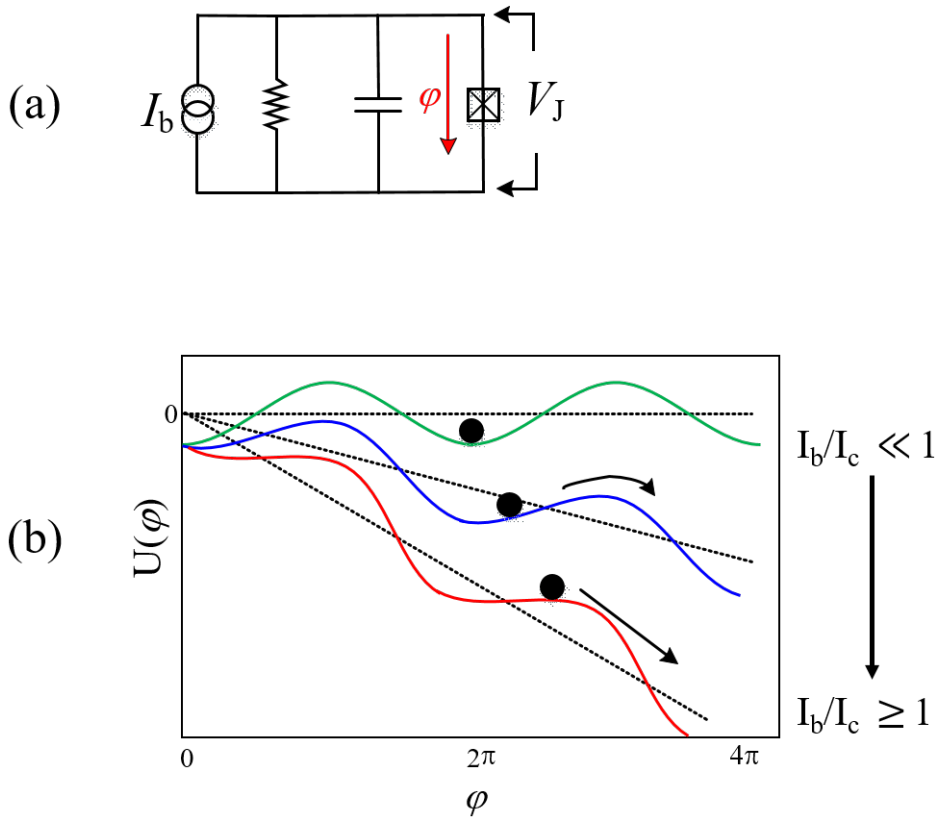


**Figure 2.11:** (a) Equivalent circuit of the RCSJ model for a Josephson junction. (b) Washboard potential profile for different biasing currents. The dashed lies indicate the current bias part of tilted washboard potential.

Figure 2.11 (b) depicts a particle in the a tilted washboard potential $U(\varphi)$. When the bias current is small, $I_b \ll I_c$, the particle sits in the potential minimum of the washboard. When the bias current is increased to $I_b \geqslant I_c$, the momentum of the particle is enough to overcome the potential minimum. The particle will start to run down the washboard potential. The moving of particle acquires some average velocity proportional to the dc-current. When the bias current is gradually lowered, and once the tilt of the washboard potential reaches its critical limit, ($I_b = I_c$), the particle is in equilibrium between stable and slide state, it will continue to move unless the viscous drag is sufficient to stop it. This viscous drag is determined by the damping parameter $\beta_c$, which is called Stewart-McCumber parameter and given by the equation

$$\beta_c = (\omega_p RC)^2 = \frac{2\pi I_c R^2 C}{\Phi_0}. \tag{2.37}$$

Here, $I_c$ is the critical current, $R$ and $C$ are the normal resistance and capaci-

tance. The Stewart-McCumber [16] parameter describes the quality factor $Q = \sqrt{\beta_c}$ of Josephson junction. The junctions dynamic is classified between $\beta_c \ll 1$ the overdamped and $\beta_c \gg 1$ the underdamped cases.

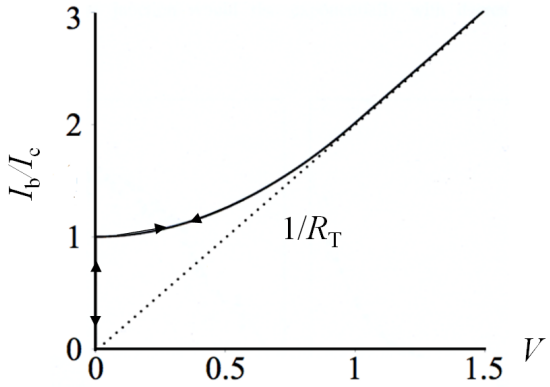


**Figure 2.12:** Normalized current - Voltage characteristic of the Josephson junction in the case of $\beta_c \ll 1$.

To describe an overdamped junction, in the case of $\beta_c \ll 1$, the simplified RSJ model can be adopted to describe the Josephson dynamics. For a bias current $I_b$ greater than $I_c$, the second derivative of the phase can be neglected (eq.((2.35)) compared to the damping term for a low quality factor ($Q \ll 1$). The displacement current is negligibly small. The differential equation governing the dynamics of a pendulum in the presence of a viscous force (eq. (2.35)) for the phase reduce to

$$\frac{\mathrm{d}\varphi}{\mathrm{d}t} = \frac{2eI_cR}{\hbar}\left(\frac{I_b}{I_c} - \sin(\varphi)\right) \tag{2.38}$$

The solution for the phase difference :

$$\varphi = 2\arctan\left(\frac{\tan\left(\frac{eR\sqrt{I_b^2 - I_c^2}}{\hbar}(t+k)\right)\sqrt{I_b^2 - I_c^2} + I_c}{I_b}\right), \tag{2.39}$$

where $k$ is a constant of integration. The period can be given be

$$T = \frac{\pi\hbar}{eR\sqrt{I_b^2 - I_c^2}} \tag{2.40}$$

The average voltage over a time period $T$,

$$\bar{V} = \frac{\hbar}{2e}\frac{\mathrm{d}\bar{\varphi}}{\mathrm{d}t} = \frac{\hbar}{2e}\frac{2\pi}{T} = R\sqrt{I_\mathrm{b}^2 - I_\mathrm{c}^2} \tag{2.41}$$

The $\mathrm{d}\bar{\varphi}/\mathrm{d}t$ is refer to the average change of phase. When the current is equal to $I_\mathrm{c}$, we have no voltage across the system. At higher currents, the voltage increases, and the $I-V$ characteristics approach the usual Ohmic behavior as shown in Fig 2.12.

**RSFQ**

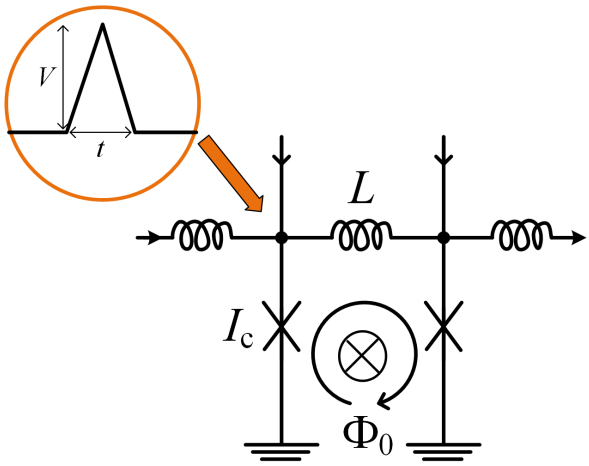


**Figure 2.13:** Equivalent circuit for the RSFQ unit circuit with a SFQ voltage pulse.

The Rapid Single flux quantum (RSFQ) pulses circuit is generated by a two-junction interferometer composed of overdamped Josephson junctions. It stores and propagates an information on a superconducting transmission line in the form of single flux quantum (SFQ) ($\Phi_0 = h/2e \simeq 2.07 \times 10^{-15}$).

When the SFQ propagates, it is transmitted in the form of a short voltage pulse $V(t)$ at the junction with the area

$$\int V(t)dt \leq \Phi_0 \tag{2.42}$$

The RSFQ pulse shapes and amplitudes depend on McCumber-Stewart parameter $\beta_\mathrm{c}$. For the short RSFQ pulses, the system requires $\beta_\mathrm{c} \leq 1$.

### 2.3.3 Superconducting Tunnel Junctions

In 1960, the Superconducting Tunnel Junctions (STJs) were first used by Giaever [26] to study quasiparticle densities in Sn. The superconductor-insulator-superconductor (SIS) structure is the basis of a STJs. STJs are used as photon-counting detectors in a wide range of photon energies from near infrared to X ray. They are based on the quasiparticle tunneling, and the Josephson effect is usually suppressed with a magnetic field.

For a STJ at zero temperature, the current is strictly zero for all voltages less than $2\Delta/e$. At finite temperatures, however, a finite current flows due to the tunneling of thermal quasiparticles. The tunnel current is given by [27]

$$I_{\mathrm{STJ}} = \frac{1}{eR_{\mathrm{N}}} \int_{\infty}^{-\infty} \frac{|E|}{[E^2 - \Delta_1^2]^{1/2}} \frac{|E + eV|}{[(E + eV)^2 - \Delta_2^2]^{1/2}} [f(E) - f(E + eV)] dE, \quad (2.43)$$

where the integral is assumed to exclude values of $E$, where $|E| < \Delta_1$ and $|E + eV| < \Delta_2$, $R_{\mathrm{n}}$ is the normal tunnel resistance in the absence of superconductivity, and $\Delta_{1,2}$ is the superconducting gap of each superconductor electrode. At $T = 0$, the quasiparticle density of states is strictly zero for $|E| < \Delta$. The number of thermal quasiparticles at a finite temperature may be calculated by assuming occupation probability given by a Fermi distribution, $f(E) = 1/(1 + e^{E/k_{\mathrm{B}}T})$.

As a photon detector, the two superconducting electrodes act as radiation absorbers. The charge carriers can be detected through the tunnel-current pulse with amplitude proportional to the incoming photon's energy when the STJ is under a finite voltage bias. The number of charge carriers generated is proportional to the energy of the absorbed photon.

The STJ also can be a phonon detector or a phonon generator as shown in Fig. 2.14. The STJ phonon detector is biased below its superconducting gap with voltage $V_{\mathrm{detector}} < 2\Delta_{\mathrm{detector}}/e$. Phonons incident on the detector electrode with energy greater than or equal to $2\Delta_{\mathrm{detector}}$ will break Cooper pairs into quasiparticles in the detector electrodes, and the resulted quasiparticles may tunnel to the other superconducting electrode (Fig. 2.14 (a)). The continuous pair breaking and the recombination of quasiparticles with the absorption of phonons lead to an increase in the tunneling current through the detector.

As depicted in Fig. 2.14 (b), when quasiparticle tunnelings occur across a STJ, the tunneled quasiparticles relax in energy emitting phonons down to the edge of the energy gap quickly because the density of states there is very large. Then, they recombine to Cooper pairs also emitting phonons. The former phonons are called *relaxation phonons*, and the latter phonons are called *recombination phonons* [28]. Thus, a STJ can be a phonon generator. It is well known since 1960's that, in these energy emitting processes, phonon emission is dominant and photon emission is negligible [29, 30].

The generation and detection of phonons with STJs was first demonstrated by using a $Sn/SnO_2/Sn$ STJs on both faces of a sapphire single-crystal cylinder of a length of approximately 1 cm by Eisenmenger and Dayem in 1967 [31]. Recently, a group in Cornell University used mesoscopic STJs to investigate phonon propagation through Si crystals using mesoscopic STJs [32–35].

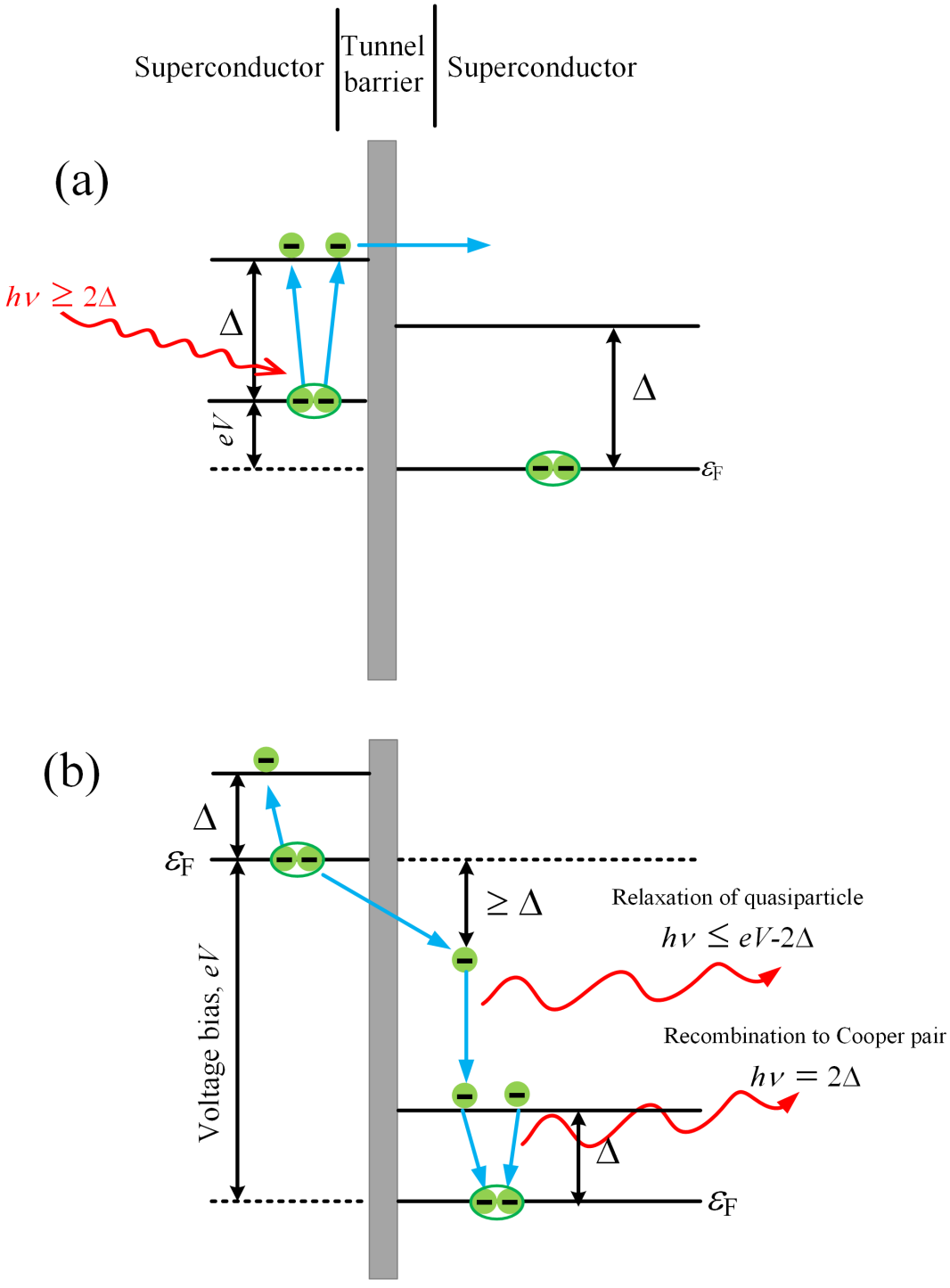


**Figure 2.14:** (a) Energy diagram illustrating phonon detection with superconducting tunnel junctions at $V < 2\Delta/e$. (b) Energy diagram illustrating phonon emission with superconducting tunnel junctions at $V \geq 2\Delta/e$.

# Chapter 3

# Device fabrication and measurement techniques

## 3.1 Introduction

Nowadays, the advancement of electron beam lithography (EBL) technique allows fabrication of nano-scale devices. This chapter explains device fabrication methods and describes the measurement techniques used in this study. It describes the nano-scale device fabrication techniques used to fabricate SCPT devices and other superconducting circuits as well as the cryogenic techniques such as a dilution refrigerator required to study the superconducting circuit performance.

## 3.2 Device fabrication techniques

### 3.2.1 Wafer preparation

Wafer preparation is the initial stage of the fabrication processes. The wafer was made from $Si/SiO_2$ and was cleaned with acetone to remove impurities from substrate then passed into isopropanol to be washed. And it was blown to be dried using a Nitrogen gun. After the cleaning process, the positive resist was spun onto the wafer. Firstly, Microchem LOR 3A, the bottom layer of positive resist was spun onto the wafer to set a 500 nm [36] thickness based on the curves of spin coating characteristic. Then the wafer was baked on a hot plate for 15 minutes at 200 °C

to harden the resist. Secondly, Microposit S1813, the top layer of positive resist was spun on top with a 1200 nm [37] thickness and baked for 2 minutes on a hot plate at 115 °C. In the next step, the two layers of resists were UV-exposed for 8 seconds through a chromium patterned glass mask. The pattern was developed for 80 second by Microposit MF CD-26 developer. During this time, it can be tuned and checked by optical microscopy if the undercut in the bottom resist is sufficiently large or not.

A thermal evaporator was used to deposit materials under vacuum. NiCr and Au were deposited on the wafer to form the bonding pads and leads (using an oil-diffusion-pump based vacuum system in this study). First, the NiCr, 0.5 nm thickness, was evaporated onto the wafer. NiCr was used to become an adhesion layer between $SiO_2$ and Au. Secondly, Au was also evaporated in the same way and at the same rate, its thickness was about 30 nm typically. After the deposition, the resist and the deposited material on it were lifted off in KAYAKU PG remover for approximately 15 minutes at room temperature.

The next process is dicing. The wafer can be cut into small chips of the size 6x6 $mm^2$ by scratching it with a diamond tip. The small chips with the gold pads and leads or a sets of such chips before individual cutting are ready for the fabrication of nano-scale devices composed of small Josephson junctions using an electron beam lithography.

### 3.2.2 Creation of the device structure using electron beam lithography

The high-resolution technique for fabrication of the nano-scale devices is electron beam lithography (EBL) technique. In this study, we used an EBL machine model Beaw Draw by Tokyo Technology based on JEOL JSM-7100F scanning electron microscope with field electron emission. In the EB writing, we used its maximum acceleration voltage of 30 kV. The chips were inserted into acetone and then in isopropanol for cleaning the surface and blow-dried using a dry nitrogen gun. The samples with $Al/AlO_x/Al$ Josephson junctions were fabricated by using the two-angle shadow evaporation [38]. The shadow evaporation technique is a different

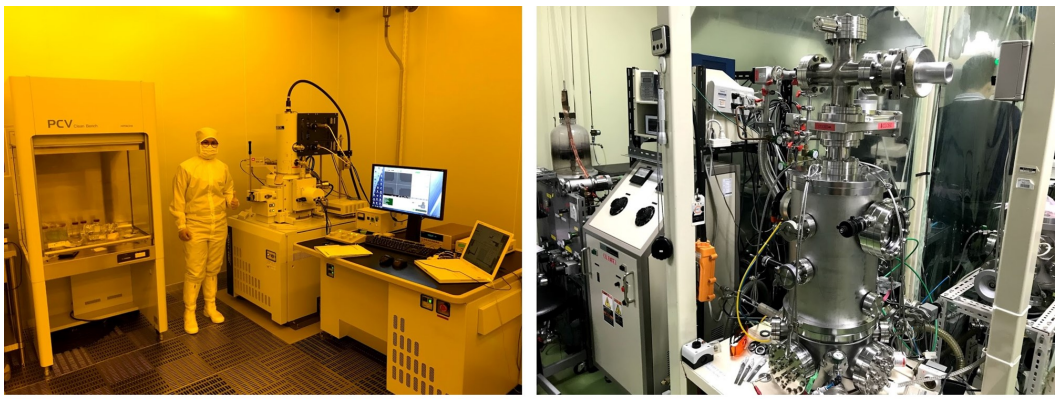

(a) EBL system (b) E-beam evaporation system

**Figure 3.1:** Photographs of the device fabrication instruments. (a) electron beam lithography (EBL) (JEOL JSM-7100F + BEAMDRAW (Tokyo Technology)) and (b) electron beam evaporation system.

oblique angle thin-film deposition evaporation technique in which nanoscale thin-film structures are produced by using an electron-beam lithography technique. For the two-angle shadow evaporation, the making of an undercut is necessary. The first layer, an organic copolymer resist (NANO Copolymer 11% in Ethyl Lactate, Copolymer 11%) was spun with a spin speed 4000 rpm which produced 500 nm thickness [39] to the chips and baked on a hot plate at 170 °C for 3 minutes. A second organic resist (NANO 950k PMMA 2% Anisole, PMMA 2%) was spun with a spin speed 4000 rpm which produced 60 nm thickness [39] and baked at 170 °C for 5 minutes.

The device structure was designed with a software VectorWorks program and was drawn by the electron beam on a chip. The device structure in Fig. 3.2 had written on each chip which has a 200 x 200 $\mu m^2$ central area. It had to assign a dose factor to every geometrical object and set a suitable low beam current for both the resist layers.

After the electron beam exposure, the bi-layer resists were developed together with a mixture of isopropanol and deionized water of the volume ratio of 10 part to 1. The immerse time can be at least 45 seconds and up to 2 minutes. It depends on the size of the undercut (Fig. 3.3(b)) that can be checked again by using an optical microscope.

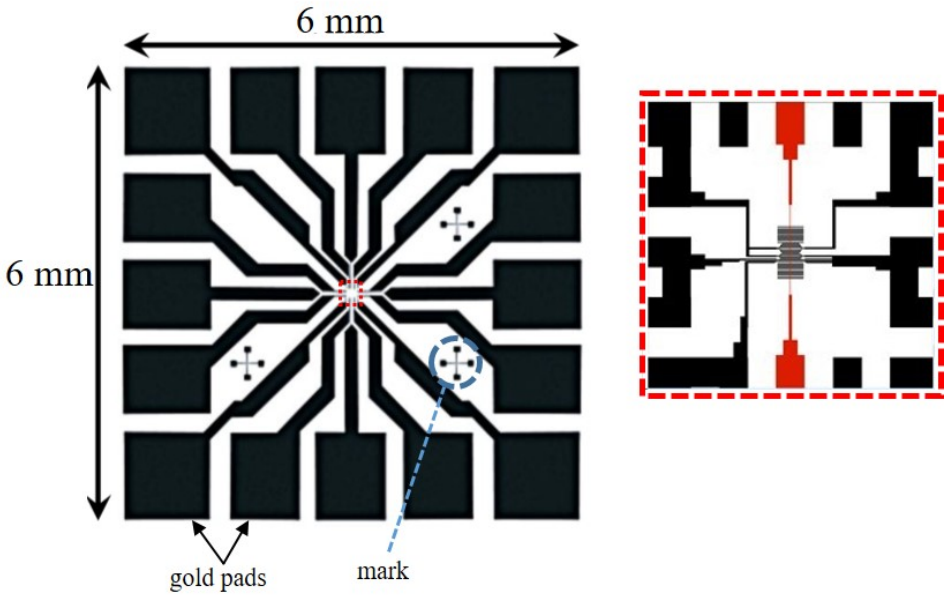


**Figure 3.2:** The picture of the fabricated gold leads pattern on the substrate. The leads connect the 16 contact pads to the small structure which, is fabricated inside 200 x 200 $\mu m^2$ area by EBL, of the device of this study. The dashed circles show the alignment markers for small structure fabrication step.

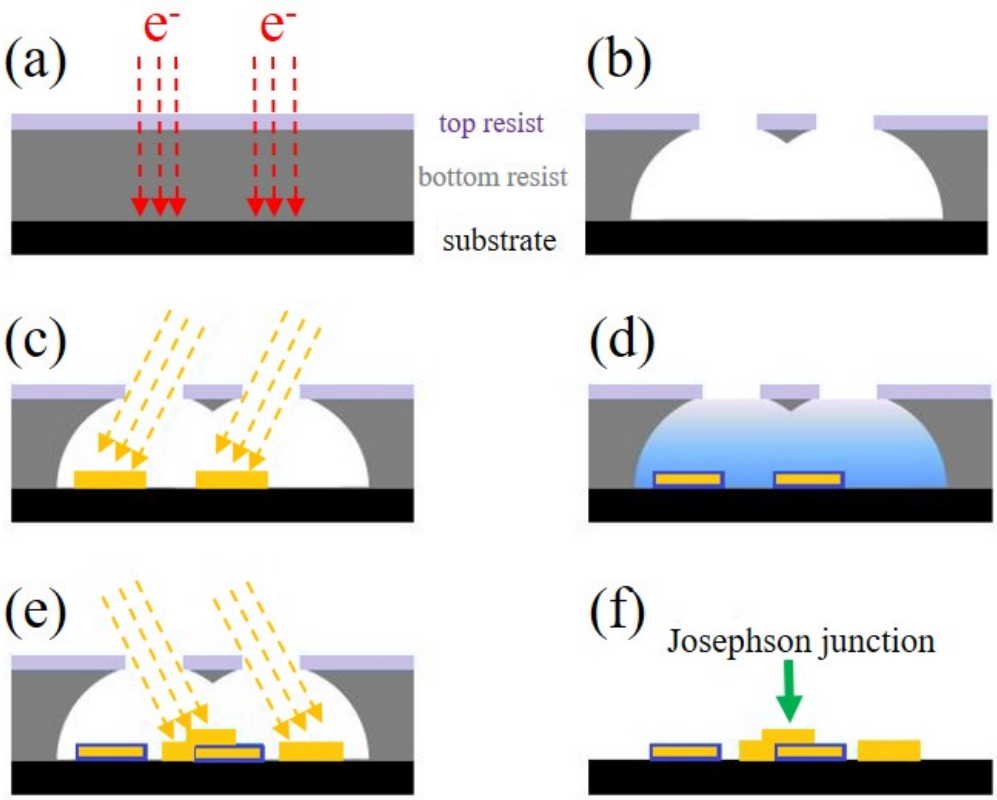


**Figure 3.3:** The schematic of the fabrication process for Josephson junction with the EBL. a) Exposure process by electron beam, b) Development process for creation of an undercut, c) The Al evaporation (first layer), d) Oxidation, e) The Al evaporation (second layer); it creates overlap between two aluminium layers. f) Lift off process.

### 3.2.3 Metal deposition with subsequent lift-off

The fabrication of small $Al/AlO_x/Al$ Josephson junction was performed by using electron beam evaporation. After heating up the source until a stable rate of 0.18 - 0.2 nm/sec was reached, 25 nm of aluminum layer was evaporated under an angle of $+11^\circ$ of the chip surface, typically, at first. Secondly, exposing the deposited Al surface to the pure oxygen with a pressure around $10^{-2}$ Torr for 2-3 minute for $AlO_x$ layer. Next, the second layer of aluminum was deposited in the same way as the first layer but at an angle -8° and a thickness of 40 nm, typically. The steps follow the figure 3.2 (c)-(f).

The final step in the chip fabrication process is lift-off. The remaining resist was dissolved by immersing the chip in acetone for nearly an hour. After this treatment, the chip was dipped into isopropanol and then to dry the chip with the nitrogen gun. The lift-off is complete. It can be checked with an optical microscope. The $Al/AlO_x/Al$ junctions formed through this technique are stable.

Small Josephson junctions are very sensitive to electrostatic discharges which can destroy the junctions. Therefore, one need to be very careful about the handling of the chip in the room temperature characterization. The normal state resistance was measured using a dedicated handheld multimeter. Now the sample is ready and one can do experiments on it.

## 3.3 Measurement techniques

### 3.3.1 Compact dilution refrigerator

The junction those fabricated with the 200 nm x 100 nm junction area results in a capacitance in fF unit. This results in a charging energy $E_c$ of the order of 1K. To reduce the thermal fluctuations, the sample temperature should be kept at lower than 1K. The low temperature can be easily achieved using a $^3$He-$^4$He dilution refrigerator [40]. In this study, we used a laboratory-made compact dilution refrigerator of a top-loading type [41]. It had a mixing chamber of a volume of approximately 4 $cm^3$ with a calibrated Cernox thermometer and sample holder. The thermometer was measured using Picowatt AVS-47 resistance bridge. A schematic

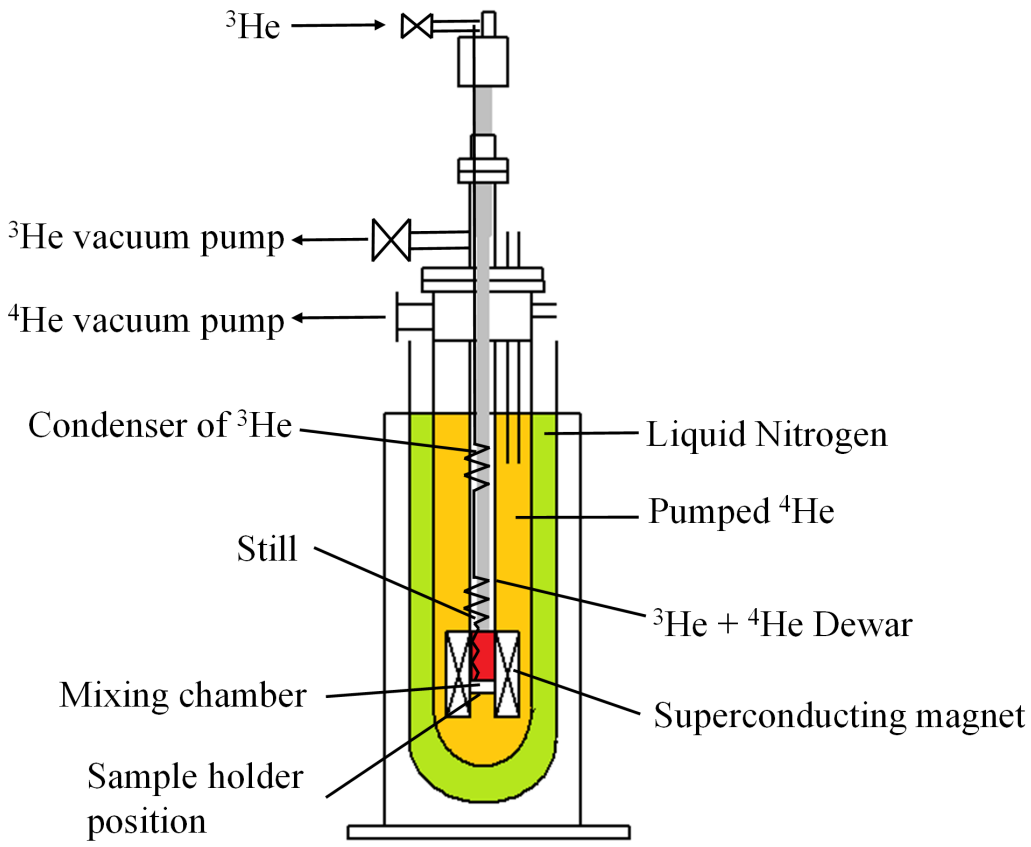


**Figure 3.4:** A schematic of a dilution refrigerator

diagram of the compact dilution refrigerator is shown in Fig. 3.4.

It will take less than 3 hours to reach base temperature from room temperature. The refrigerator is surrounded by a 5-liter capacity isolated glass dewar for $^4$He liquid. This dilution refrigerator can operate about 3 hours at base temperature 80 mK by filling the $^4$He liquid from the external dewar. A compact dilution refrigerator is very useful in an electromagnetic shielded room to avoid disordered interference from radio frequencies and mobile frequencies in all the electrical transport measurements.

The system was set up with 12 dc-leads down to mixing chamber. Each lead contains an L-type electromagnetic compatibility filter at room temperature and a RLC low-pass filter between the mixing chamber and the 1K stage which were to avoid the transmission of electrical noise to the sample. Magnetic field can be applied to the sample using a superconducting magnet. The fabricated sample was glued onto a socket. The Au-pads of the sample were connected to the signal lines in

the mixing chamber of the dilution refrigerator. The sample was directly immersed in the dilute phase of the helium mixture in the mixing chamber.

### 3.3.2 Measurement station

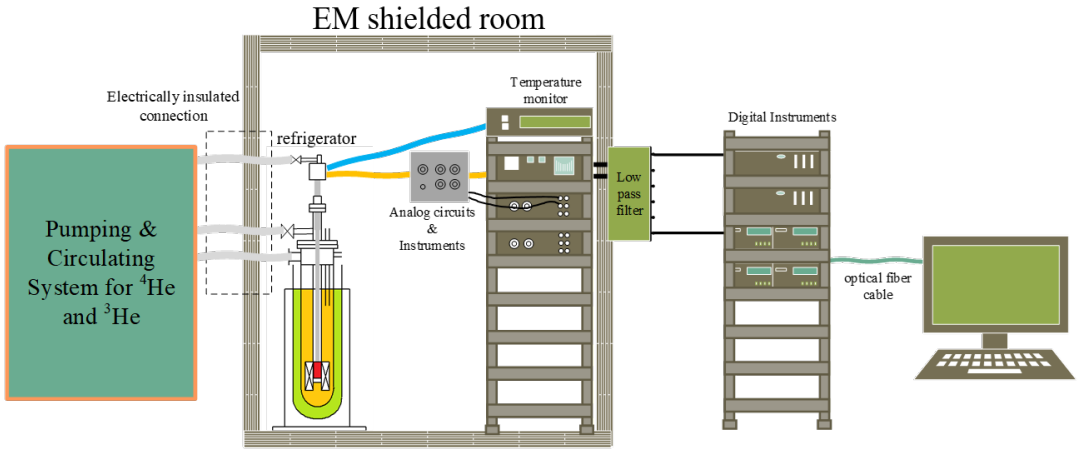


**Figure 3.5:** Schematic of the measurement station.

Figure 3.5 shows the structure of the measurement system. The compact dilution refrigerator and the analog circuits and instruments are in an electromagnetically shield room. The pumping and circulating system for $^3$He and $^4$He is connected with the compact dilution refrigerator via electrically insulated connections. The electrical signals are measured with analog circuits and passed to the digital instruments outside the shielded room via low pass filters. The measured data from the digital instruments, which link via the optical fiber cable is recorded by the developed program for measurement using LabVIEW software.

### 3.3.3 Analog circuits and instruments

Generally, the $I$–$V$ characteristics of the Josephson junctions are non-ohmic at low temperature. Intended for tracing the curves accurately, it is necessary to design a suitable load line for the bias circuit as in Fig. 3.6. If sample resistance $R_{\mathrm{x}}$ is much larger than the bias resistance $R_{\mathrm{b}}$, the sample will be in a voltage biasing. In this situation, the load line shows a vertical characteristic line. Conversely, when $R_{\mathrm{b}}$ is much larger than $R_{\mathrm{x}}$, the sample will be in a current biasing. In this current biasing, the load line is horizontal. $R$-bias is other biasing for $I$–$V$ characteristics

where $R_x$ is comparable with $R_b$, and then the load line has a finite slope. All of these three biasing situation with the load lines are shown in Fig. 3.7 schematically.

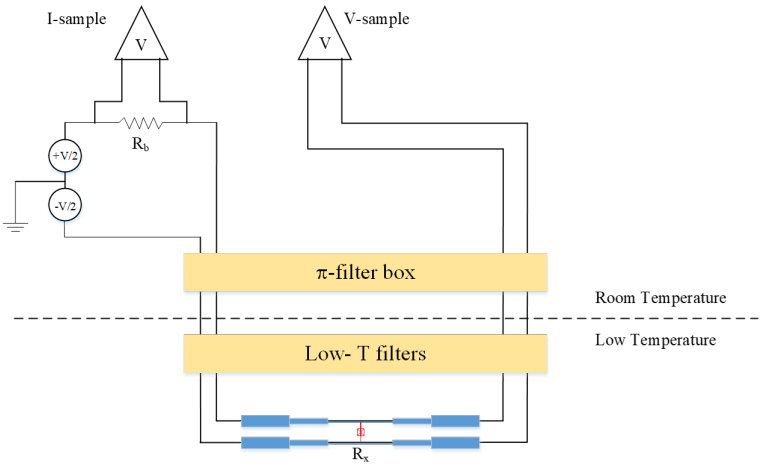


**Figure 3.6:** Schematic of an experimental setup to measure $I - V$ characteristics of samples. The schematic shows the used filters in the dilution refrigerator.

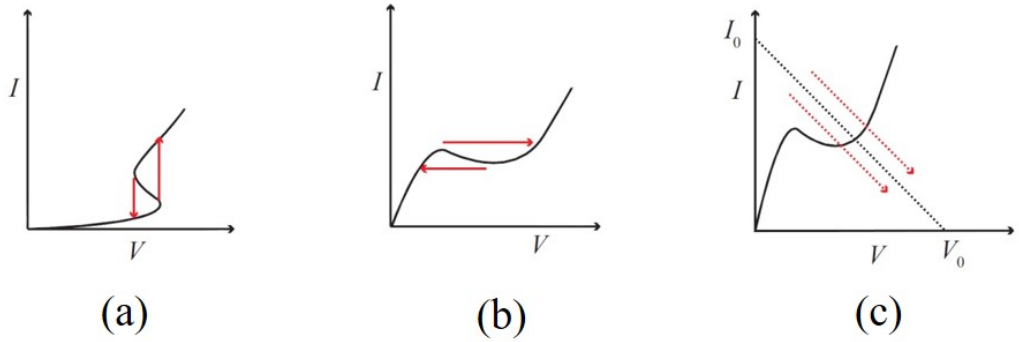


**Figure 3.7:** Tracking of sample $I$–$V$ characteristics in the (a) voltage bias condition, $R_b \ll R_x$, (b) current bias, $R_b \gg R_x$, and (c) R-bias condition, $R_b \leq R_x$. The red arrows show the unstable tracking points of the curves while the dotted black line shows the finite slope of $R$-bias tracking condition.

The equivalent circuit of the used R-bias scheme is shown in Fig. 3.8. A serial resistor $R_b$ which can be changed from 1kΩ to 1GΩ symmetrically bias the sample so that the lope of the load line can be appropriately chosen. The instrumentation amplifiers used in the circuit comprise INA116 ultra low bias current instrumentation amplifiers from Texas Instruments in combination with Linear Technologies low noise op amp LT1012. As depicted in Fig. 3.8, we apply bias voltage symmetrically with respect to ground. For that purpose, we used a voltage symmetrizer. A Keithley 213 quad voltage source supply $V_b$ through an appropriate voltage division.

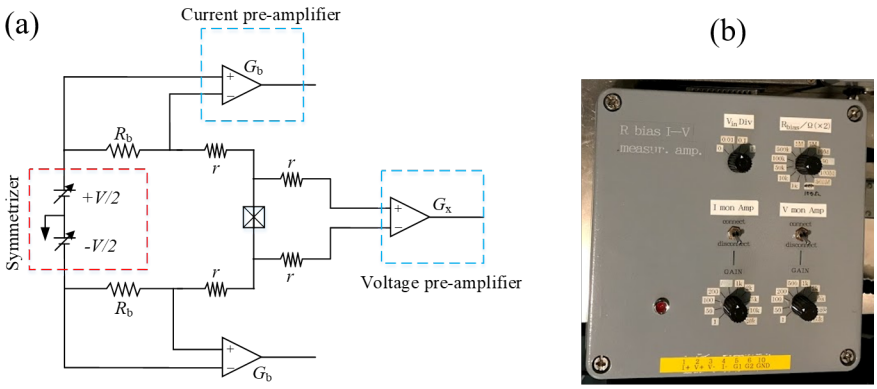


**Figure 3.8:** Simplified circuit diagrams of the measurement. (a) the symmetric R-bias scheme, the current pre-amplifier and the voltage pre-amplifier for current and voltage measurement, respectively, are indicated. (b) one channel laboratory made instrumentation amplifier box for current and voltage measurement.

In the voltage bias scheme, the voltage across the sample is measured in the same way as the R-bias scheme. The current through the sample is measured using a Stanford Research low noise current pre-amplifier SR570. The used SR570 has been modified so that bias voltage is applied externally. SR570 has an input resistance whose magnitude depends on the selected current/voltage conversion ratio. The input resistance has the same role as $R_b$ in the circuit. So the conversion ratio need to be appropriately chosen for the specific measurement. The current amplifiers give an output voltage proportional to the current through the sample.

The measured and amplified current and voltage are dispatched to data acquisition apparatus outside of the shielded room through low-pass filters.

### 3.3.4 Digital instruments

The digital instruments are located outside of the electromagnetically shield room. We used Keithley 213 quad voltage source for the source of the bias voltage for the measurement. Its output voltage ranges from 0 to 10V. The Keithley 2000 digital multimeters were used measure the analog signals from the shield room. All of the digital instruments are controlled by the PC controller via an optically isolated GPIB.

# Chapter 4

# Scalability of supercurrent modulable with single Cooper-pair transistors connected in parallel

## 4.1 Introduction

As described in 2.2, SCPT is a basic element for many basic applications such as quantum computing, sensitive electrometry, etc [7, 21, 24, 42, 43]. The most distinct characteristics of a SCPT in contrast to a single-electron transistor (SET) [44] is a supercurrent flow, that is modulated with a gate voltage showing a $2e$ periodicity in the gate induced charge as explained in 2.2. The Cooper-pair tunneling through the junction is a coherent process because of the Josephson coupling between superconducting electrodes in contrast to the case in a SET, where the electron tunneling is stochastic. The Cooper pairs tunnel through the junction back and forth with a frequency of $E_{\mathrm{J}}/h$ [45, 46]. With $E_{\mathrm{J}}$ of 100 $\mu$eV, for example, the frequency of the coherent oscillation becomes larger than 20 GHz. Thus, SCPT can work as a fast supercurrent switch. Thus far, direct applications of such a feature are few. Born et al. [47] and Zangerle et al. [48] inserted a SCPT in a superconducting loop and measured the state of the SCPT itself as a charge-phase qubit at tens of

MHz range on the basis of the theoretical analysis by Zorin [49, 50].

On the other hand, the magnitude of the supercurrent which can flow through a SCPT is typically smaller than 100 nA [51–55] by orders of magnitude smaller than those in the other superconducting electronics technologies such as SFQ circuits [56], SQUID electronics [57] etc. Figure 4.1 shows a gate modulation curve of a supercurrent in an Al-based SCPT obtained by Agren et al. [51]. It is one of the examples in which a large supercurrent was obtained with a fairly large modulation of it with a gate voltage. The magnitude of the maximum supercurrent is above 11 nA, and its modulation depth is approximately 35 %. The device was fabricated using EBL and shadow evaporation techniques. The parameters of the junctions are $R_{\mathrm{T}} = 4.9$ kΩ, $C_{\Sigma} = 1.3$ fF, $E_{\mathrm{J}} = 129$ $\mu$eV, $E_{\mathrm{c}} = 62$ $\mu$eV, and $E_{\mathrm{J}}/E_{\mathrm{c}}$ ratio is 2.1. In order to combine a SCPT with other superconducting electronics, it is desirable to increase the magnitude of the supercurrent through the SCPT.

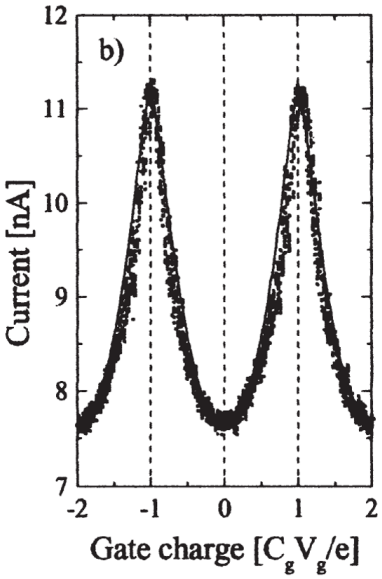


**Figure 4.1:** Switching currents versus gate charge number $C_{\mathrm{g}}V_{\mathrm{g}}/e$, for SSET at 35 mK. The switching current is $2e$ periodic. The solid line shows simulation assuming proportionality between the switching current and the critical current [51].

### Attainable supercurrent magnitude with a single SCPT

Here, we examine a possibility to enlarge the modulable supercurrent through a single SCPT, first. As described in 2.2, the supercurrent through a SCPT is proportional to $E_{\mathrm{J}}$ (see the Zorin's expression in eq. (2.26)), and $E_{\mathrm{J}} = (R_{\mathrm{Q}}/2)(\Delta/R_{\mathrm{T}})$

at low temperatures ($k_{\mathrm{B}}T \ll \Delta$) according to Ambegaokar-Baratoff formula. Thus, if one wants to enlarge the supercurrent, it is required to increase the factor $\Delta/R_{\mathrm{T}}$. For a fixed material, one needs to decrease the tunnel resistance of the junction $R_{\mathrm{T}}$. On the other hand, the gate modulation is due to the charging effect, and the modulation depth depends on the $E_{\mathrm{J}}/E_{\mathrm{c}}$ ratio as shown in Fig. 2.6. The $E_{\mathrm{J}}/E_{\mathrm{c}}$ ratio is expressed as $E_{\mathrm{J}}/E_{\mathrm{c}} = (R_{\mathrm{Q}}/e^2)(C_{\Sigma}\Delta/R_{\mathrm{T}})$. Thus, if one simply increases the factor $\Delta/R_{\mathrm{T}}$ to enlarge the supercurrent, it also increases $E_{\mathrm{J}}/E_{\mathrm{c}}$ ratio, and the modulation amplitude decreases. For example, to obtain a modulation depth to be larger than 50 %, $E_{\mathrm{J}}/E_{\mathrm{c}} < 1$ according to Fig. 2.6. To maintain the modulation amplitude large and increase the magnitude of the supercurrent, one has to decrease $C_{\Sigma}$ as well as $R_{\mathrm{T}}$ at the same time to keep the factor $C_{\Sigma}/R_{\mathrm{T}}$ unchanged.

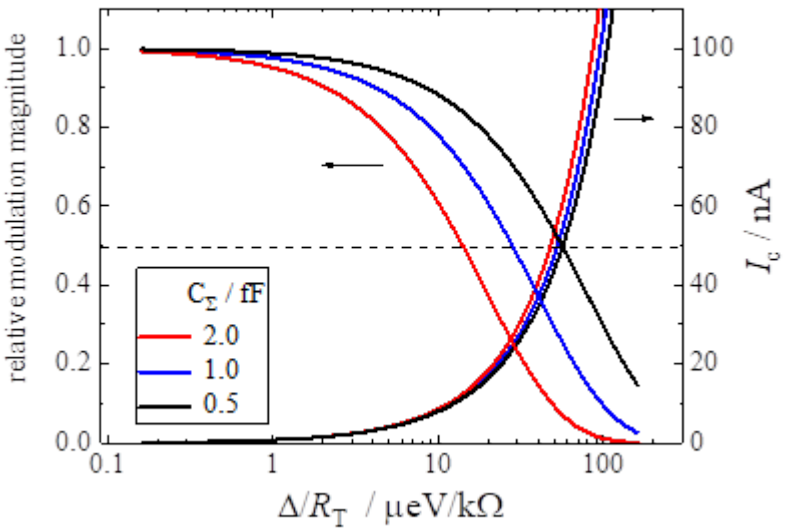


**Figure 4.2:** Calculated supercurrent and relative modulation magnitude according to the Ambegaokar-Baratoff relation and the suppression factor $\langle \cos \eta \rangle$ of the Josephson current due to the charging effect base on Zorin's estimation [17]. $C_{\Sigma}$ are defined 0.5, 1.0 and 2.0 fF.

To satisfy this required condition, one needs to use smaller-area junctions to make $C_{\Sigma}$ smaller and also use thinner tunnel barriers to make $R_{\mathrm{T}}$ smaller. With a standard EBL technique, it is not easy to make well defined junctions with the area smaller than 10 nm × 10 nm. Their size will be between 100 nm × 100 nm and 10 nm × 10 nm. The resultant SCPT capacitance $C_{\Sigma}$ will be around 1 fF as in the case of the device for Fig. 4.1. Consequently, $E_{\mathrm{c}} \simeq 80$ $\mu$eV and $E_{\mathrm{J}}$ is also ∼80 $\mu$eV for

$E_J/E_c = 1$, for example. This corresponds to a supercurrent of approximately 40 nA according to the Ambegaokar-Baratoff relation, and, considering the suppression factor due to the charging effect $\langle \cos \eta \rangle$ (eq. (2.26)), the maximum theoretical value will become approximately 20 nA as in Fig. 4.2. In real devices, the supercurrent often becomes smaller because of the influence from the measurement environment [51]. This estimated case roughly corresponds to that of Fig. 4.1. Thus, with a standard fabrication technique, it is impossible to obtain a well modulable supercurrent larger than 100 nA for a single SCPT.

### The adopted approach

As an alternative method, multiple SCPTs connected in parallel, thus, give an easily accessible method to increase the gate modulable supercurrent which surpasses that of a single SCPT. In this chapter we study the possibility to increase the modulable supercurrent by using multiple SCPTs connected in parallel having a common gate. Such a structure was adopted in parallel superconductor/normal metal/superconductor turnstiles to increase an accurate current produced by single-electron pumping [58].

We find that the supercurrent which can flow through the parallel SCPTs is scaled up with the increase in the number of SCPTs. However, its relative modulation amplitude and, therefore, the modulability decreases with the increase in the number of SCPTs for the used device structure. We discuss the origin of the amplitude decrease and possible methods to improve the modulability.

## 4.2 Experimental methods

We produced three samples with various number $N_0$ of parallel SCPTs on one chip: sample 1 with $N_0 = 1$, 2, 5 and 10, sample 2 with $N_0 = 1$ and 100, and sample 3 with $N_0 = 1$, 10 and 50. The size of junctions were approximately 0.02 $\mu$m$^2$ for the former two samples and approximately 0.005 $\mu$m$^2$ for sample 3. Figure 4.3(a) shows an optical micrograph of sample 1, and Fig. 4.3(b) is an scanning electron microscopy (SEM) image of the SCPTs. The schematic diagram of the sample is depicted in Fig. 4.3(c). Each sample has a long thin electrode for the common gate

with a thick oxide layer on it, and parallel SCPTs are overlaid with their island electrodes aligned on it.

The samples were fabricated in two steps. In the first step, the gate electrode was constructed on a thermally oxidized Si substrate by standard EBL and subsequent electron-beam evaporation of Al. The thickness of the deposited Al film was 20 nm. After the lift-off process, the surface of Al electrodes was oxidized by the air at 24 °C for 20 hours. An $AlO_x$ layer of approximately 10 nm thickness [1] was formed on the surface of the electrodes with this treatment. In the second step, the circuits of parallel SCPTs with $Al/AlO_x/Al$ tunnel junctions, as shown in Fig. 4.3(b), were fabricated by EBL and the shadow evaporation technique as described in 3.2.2 [38]. The width and length of the island electrode were 200 nm and 2 $\mu$m, respectively. The thickness of the lower and upper electrodes were 25 and 40 nm, respectively. The tunnel barrier was formed after the first evaporation by oxidizing the surface of the lower electrode in an $O_2$ atmosphere at 3 Pa for 1 min.

In the electrical measurement of the sample, a bias voltage was applied to the sample symmetrically with respect to the ground using a symmetrized voltage source [Fig. 4.3(c)], and the four terminal point scheme was used for the measurement of $I$–$V$ characteristics of the sample.

[1] The thickness of the $AlO_x$ layer, $d$, was estimated with a parallel plate capacitor model for the gate capacitor as $d = (\epsilon_0 \epsilon_r A)/C_g$, where $C_g$ is the gate capacitance, $A$ the coupling area, $\epsilon_0$ the dielectric permittivity of vacuum, and assuming a relative permittivity of $AlO_x$, $\epsilon_r$, to be 8.5.

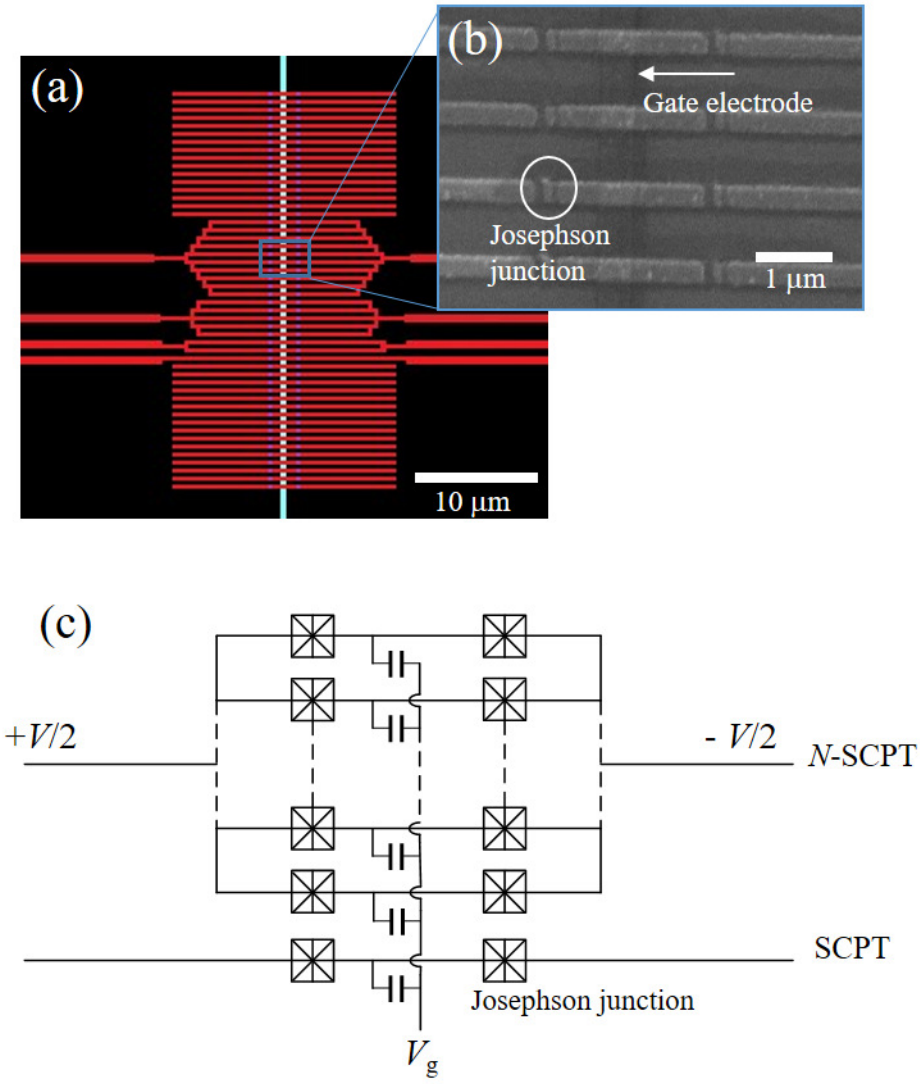


**Figure 4.3:** (a) False color optical microscopy image of the fabricated sample (sample 1). The sample has a single, two, five and ten SCPTs in the central part. The single vertical electrode (white) is the common gate electrode. The simple thin line electrodes above and below the SCPT part are dummy electrodes. (b) Scanning electron microscopy (SEM) image of the SCPTs. (c) Equivalent circuit of the parallel SCPTs. A common gate electrode is capacitively coupled to the island electrode of each SCPT. The method of applying a bias is also shown.

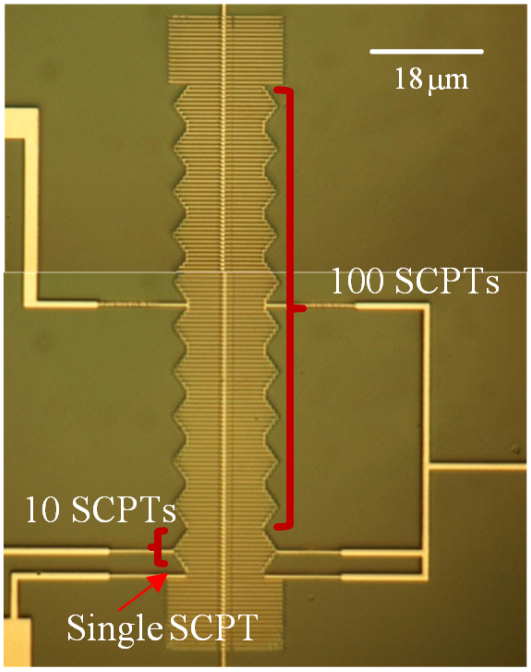


(a) Sample 2

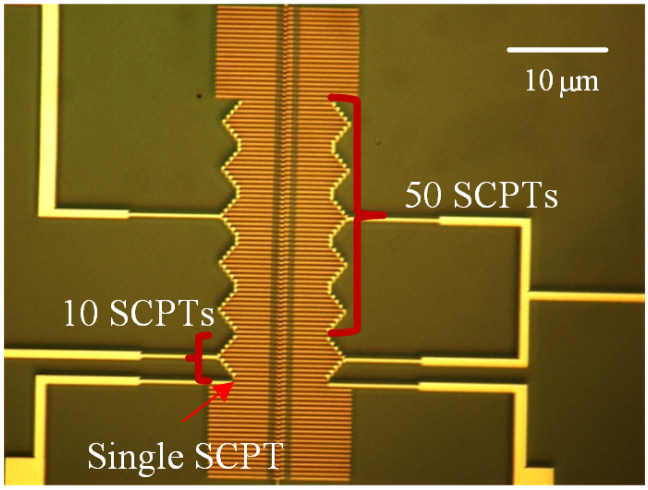


(b) Sample 3

**Figure 4.4:** Optical microscopy image of the fabricated samples; (a) sample 2[1]and (b) sample 3.

[1]We fabricated 10 SCPT-device in sample 2. However, its characteristics changed during the measurement and didn't give consistent data. Thus, we didn't use this device in the study.

## 4.3 Experimental results

### 4.3.1 Effective number of SCPTs and sample parameters

Table 4.1: Parameters of the samples: nominal number of SCPTs $N_0$, differential conductance of the device $G_{\infty,N_0}$, effective number of SCPTs $N_{\rm eff}$, tunnel resistance $R_{\rm T}$ of the junction, junction capacitance $C$, Josephson coupling energy $E_{\rm J}$ of the junction, charging energy $E_{\rm c}$, the $E_{\rm J}$ to $E_{\rm c}$ ratio, and gate capacitance $C_g$. The values with parentheses are assumed values on the basis of those of the single SCPT.

| sample/ device | $N_0$ | $G_{\infty,N_0}$ ($\mu$S) | $N_{\rm eff}$ | $R_{\rm T}$ (k$\Omega$) | $C$ (fF) | $E_{\rm J}$ ($\mu$eV) | $E_{\rm c}$ ($\mu$eV) | $E_{\rm J}/E_{\rm c}$ | $C_g$ (fF) |
|---|---|---|---|---|---|---|---|---|---|
| 1-a | 1 | 25.1 | 1 | 19.9 | 0.85 | 24 | 38 | 0.63 | 0.40 |
| 1-b | 2 | 51.2 | 2 | 19.5 | (0.85) | 24 | (38) | (0.63) | 0.39 |
| 1-c | 5 | 130 | 5 | 19.3 | (0.85) | 24 | (38) | (0.63) | 0.39 |
| 1-d | 10 | 249 | 10 | 20.1 | (0.85) | 24 | (38) | (0.63) | 0.39 |
| 2-a | 1 | 23.0 | 1 | 21.7 | 0.89 | 25 | 32 | 0.78 | 0.72 |
| 2-b | 100 | 1410 | 61 | 21.5 | (0.89) | 25 | (32) | (0.78) | 0.71 |
| 3-a | 1 | 42.0 | 1 | 11.9 | 0.32 | 42 | 83 | 0.51 | 0.33 |
| 3-b | 10 | 364 | 9 | 12.4 | 0.32 | 42 | (83) | (0.51) | 0.33 |
| 3-c | 50 | 1680 | 40 | 11.9 | 0.32 | 42 | (83) | (0.51) | 0.32 |

First we measured an asymptotic $I$–$V$ curve at high bias ($V \gg 2\Delta/e \simeq 400\mu$V) of each device of $N_0$ parallel SCPTs to obtain the differential conductance $G_{\infty,N_0}$ in the quasiparticle tunneling regime. Because we could not examine the properties each of the SCPTs separately in the parallel connection, we estimated an effective number, $N_{\rm eff}$, of active SCPTs in each parallel connection as $N_{\rm eff} \simeq G_{\infty,N_0}/G_{\infty,1}$ assuming the same tunnel resistance between the single SCPT and each of the parallelly connected SCPTs on the basis that the quasiparticle-tunneling process in each SCPT is stochastic, independent of those of the other SCPTs in this regime and their conductance is additive. The estimated $N_{\rm eff}$ is tabulated in Table 4.1. It turns out that some devices, have $N_{\rm eff} < N_0$, likely because of an accidental failure during the fabrication process. We regarded that there were some open circuits instead of active SCPTs in the parallel circuits in those devices.

The important parameters of all devices are shown in Table 4.1. For the single SCPT, the tunnel resistance $R_T$ and the capacitance $C$ of the junction were obtained from the slope in the asymptotic $I$–$V$ curve of SCPT at high bias and the offset voltage assuming identical two junctions in the SCPT. The Josephson cou-

pling energy was calculated using the Ambegaokar-Baratoff formula [10] with the superconducting gap $\Delta \simeq 150$–$170$ $\mu$eV of our Al film, which was obtained using the differential conductance characteristics of the SCPT considering the offset voltage because of the charging effect. The gate capacitance, $C_g$, was obtained from the Coulomb oscillation (described below). The charging energy $E_c$ was calculated using the relation $E_c = e^2/2C_\Sigma$ with $C_\Sigma = 2C + C_g$.

For the parallel $N_0$ SCPT samples ($N_0 > 1$), the average value of $R_T$ of the constituent SCPTs in each device was calculated using $G_{\infty,N_0}$ and $N_{\rm eff}$. The $C$ and $E_c$ values of the junction for these devices were assumed to be the same as those of the single SCPT and are indicated with parentheses in the table.

### 4.3.2 Current-voltage characteristics and Coulomb oscillations

Figure 4.5 shows typical $I$–$V$ curves of the parallel SCPTs in sample 1. They have common features: a supercurrent ($I_p$) peak is observed near $V = 0$ $\mu$V followed by a shoulder at $V \simeq 40$ $\mu$V, on further increasing voltage, a secondary current peak ($I_s$) is observed at $V \simeq 80$ $\mu$V. The value of the maximum supercurrent $I_p$ is scaled up with the increase in the number of SCPTs in the circuits. All the devices in sample 2 and 3 also showed $I-V$ curves with the same features as shown in Fig. 4.8(a) and (b), and Fig. 4.9(a), (b) and (c), respectively.

Figure 4.6 shows typical Coulomb oscillations of the supercurrent $I_p$ of the parallel SCPTs in sample 1, and Fig. 4.7 shows those of the secondary peak $I_s$. As can be seen, the period $\Delta V_g$ for $I_p$ is twice that of $I_s$ in all the single and parallel SCPTs. The secondary current peak $I_s$ is due to a higher-order tunneling process involving nonequilibrium quasiparticles as assigned by Billangeon et al. [14], its period corresponds to a single electron charge $e$. Thus, the period of $I_p$ is $2e$ in gate charge $C_gV_g$. The periods $\Delta V_g$ were almost the same in all the devices on a single chip. The $I_p$ oscillation peak for the single SCPT in Fig. 4.6(a) has a width of 200 $\mu$V. However, with the increase in $N_{\rm eff}$, the peak width increases. Moreover, the relative magnitude of the oscillation decreases. Although the parallel SCPTs have many loops in structures, we did not observe an interference effect while sweeping

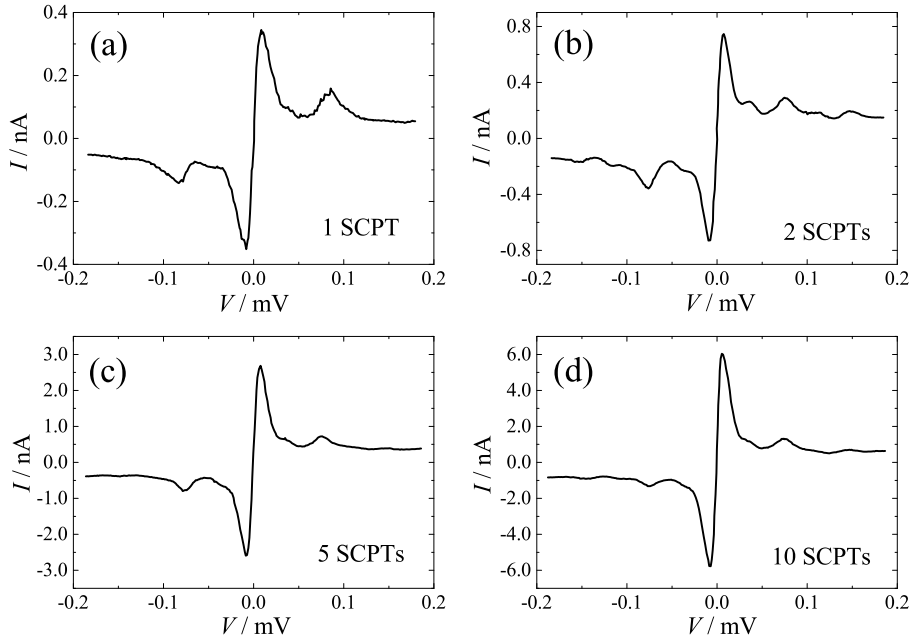


**Figure 4.5:** The current-voltage characteristics of the single SCPT and parallel SCPTs of sample 1 measured at 75 mK. (a) single SCPT (b) two SCPTs (c) five SCPTs (d) ten SCPTs.

$V_g$. It was presumably because the induced phase shifts across either constituent SCPTs, if there were, were almost the same for their identical structures.

The Coulomb oscillations of $I_p$ for samples 2 and 3 are presented in Figs. 4.8(c), 4.8(d) and 4.9(d)-4.9(f). Those for $I_2$ are presented in Figs. 4.8(e), 4.8(f) and 4.10(a)-4.10(c).

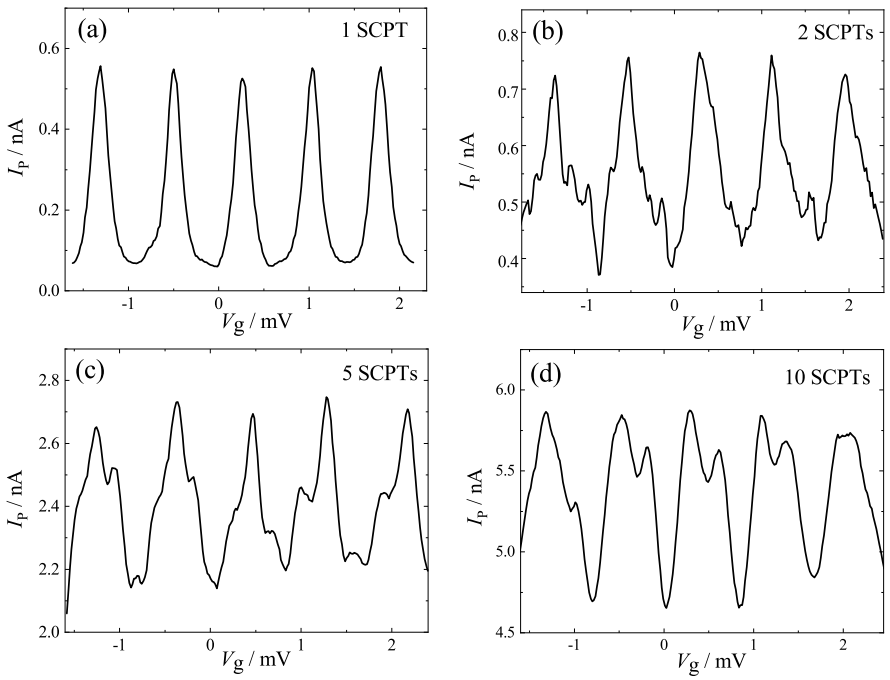


**Figure 4.6:** The Coulomb oscillations of the supercurrent $I_\mathrm{p}$ for the single and multiple SCPTs in sample 1 at 75 mK. (a) single SCPT (b) two SCPTs (c) five SCPTs (d) ten SCPTs. The observed periodicity is $2e$ in $C_gV_g$.

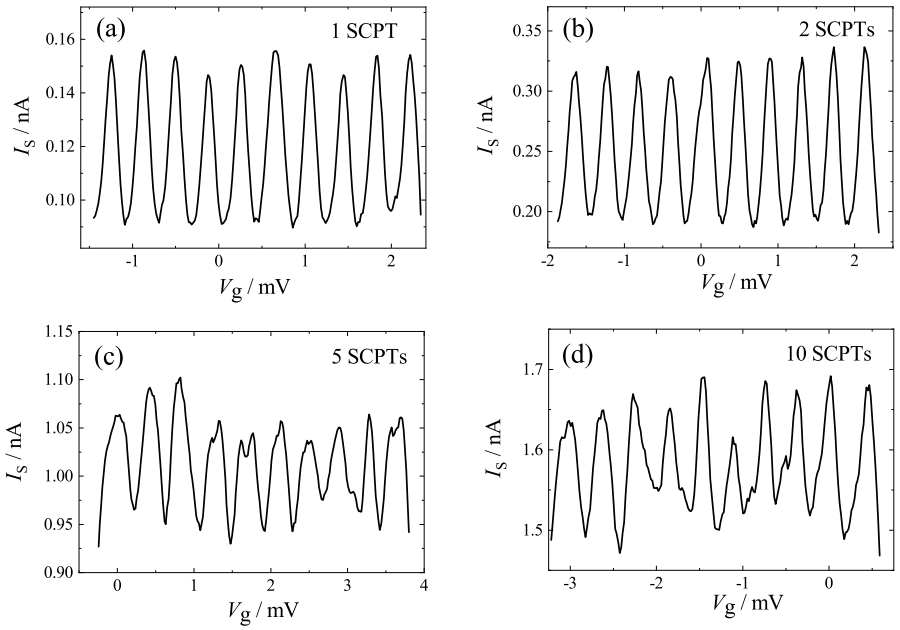


**Figure 4.7:** The Coulomb oscillations of the supercurrent $I_\mathrm{s}$ for the single and multiple SCPTs in sample 1 at 75 mK. (a) single SCPT (b) two SCPTs (c) five SCPTs (d) ten SCPTs. The observed periodicity is $e$ in $C_gV_g$.

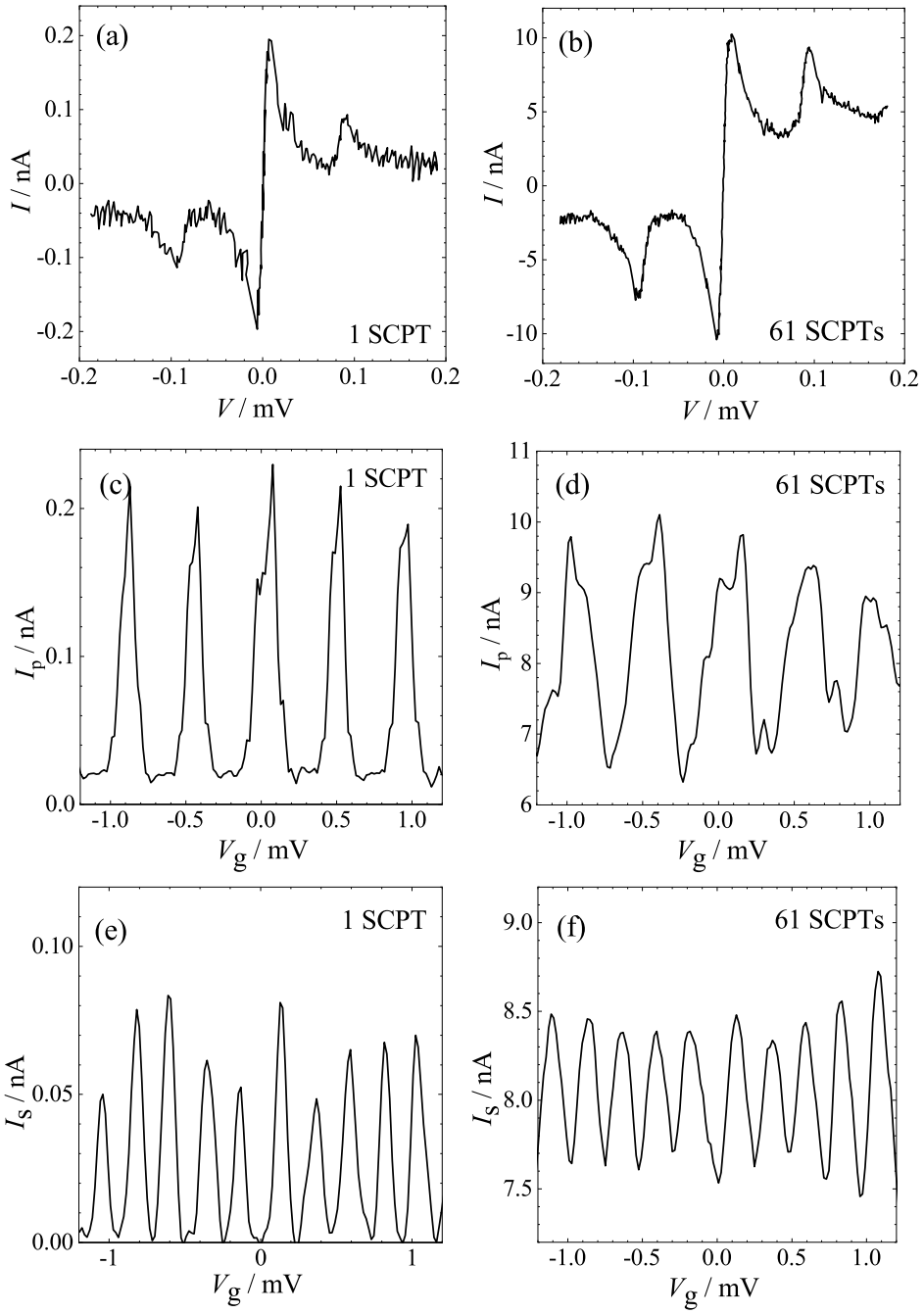


**Figure 4.8:** The current-voltage characteristics and the Coulomb oscillation characteristics for the devices in sample 2. The current-voltage characteristics of the single SCPT and parallel SCPTs measured at 75 mK. (a) single SCPT (b) 61 SCPTs. The Coulomb oscillations of the supercurrent $I_{\mathrm{p}}$ for the single and multiple SCPTs at $V_{\mathrm{bias}} = 7\mu$V, (c) single SCPT (d) 61 SCPTs. The observed periodicity is $2e$ in $C_g V_g$. The Coulomb oscillations of the supercurrent $I_{\mathrm{s}}$ at $V_{\mathrm{bias}} = 90\mu$V, (e) single SCPT (f) 61 SCPTs. The observed periodicity is $e$ in $C_g V_g$.

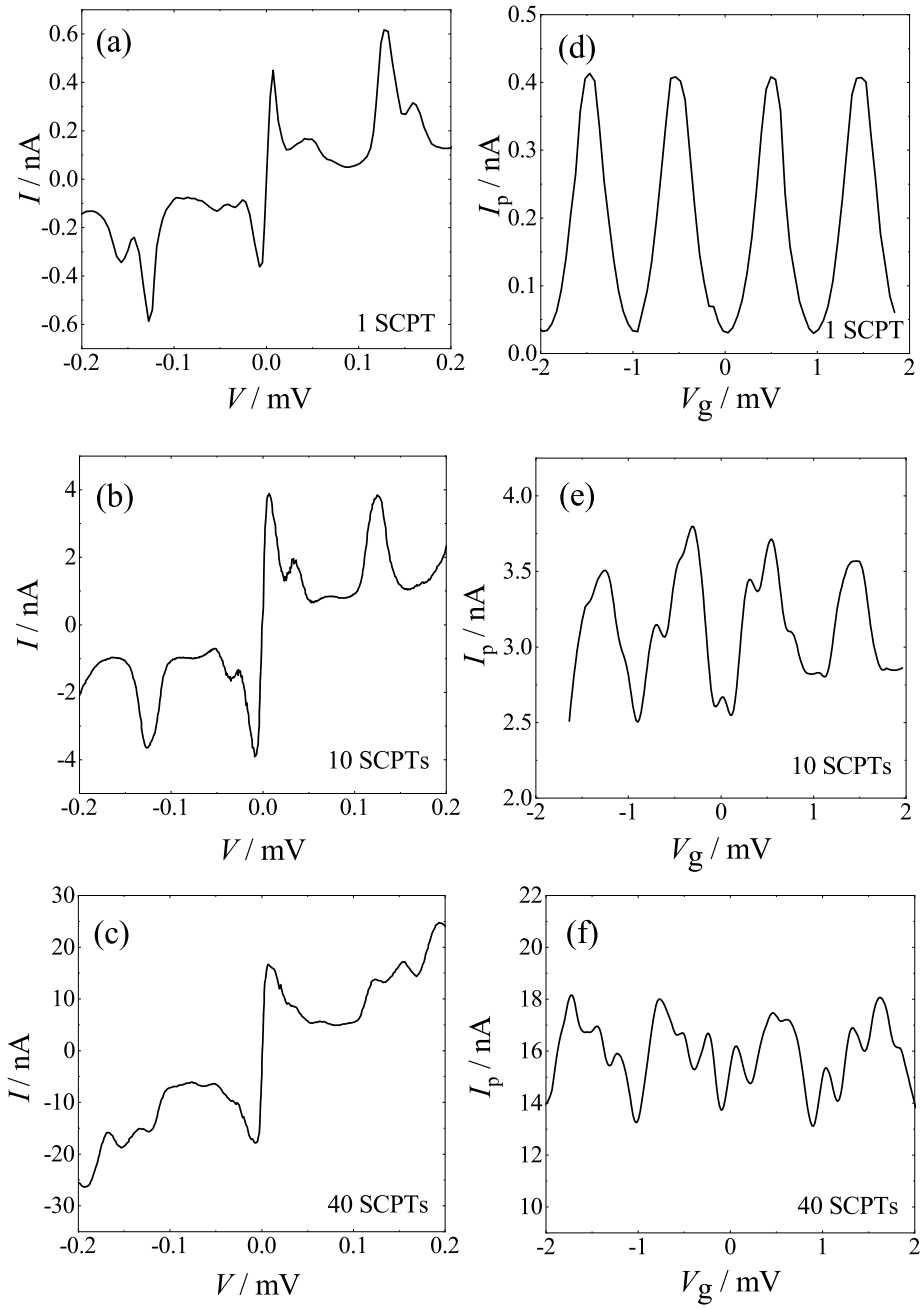


**Figure 4.9:** The current-voltage characteristics and the Coulomb oscillation characteristics for the devices in sample 3. The current-voltage characteristics of the single SCPT and parallel SCPTs measured at 75 mK. (a) single SCPT (b) 10 SCPTs (c) 40 SCPTs. The Coulomb oscillations of the supercurrent $I_{\mathrm{p}}$ for the single and multiple SCPTs at $V_{\mathrm{bias}} = 7\mu$V. (d) single SCPT (e) 10 SCPTs (f) 40 SCPTs. The observed periodicity is $2e$ in $C_g V_g$.

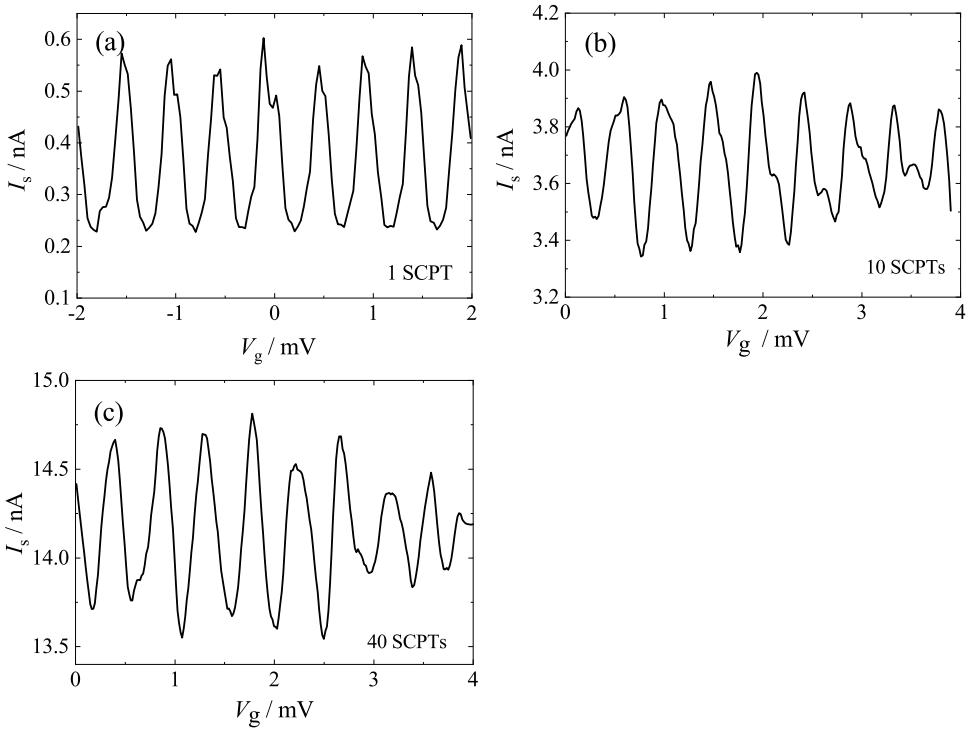


**Figure 4.10:** The Coulomb oscillations of the supercurrent $I_s$ at $V_{bias} = 120\mu V$ for the single and multiple SCPTs in sample 3 at 75 mK (a) single SCPT (b) 10 SCPTs (c) 40 SCPTs. The observed periodicity is $e$ in $C_g V_g$.

Figure 4.11(a) indicates the dependence of the maximal supercurrent (with respect to $V_g$), $I_{pp}$, normalized with $I_{pp1}$ of the single SCPT upon $N_{eff}$ for the three samples. A nearly linear increase in $I_{pp}$ as a function of $N_{eff}$ up to $N_{eff} > 10$ is clearly observed. We then assumed a Gaussian shape for a single Coulomb oscillation peak (with respect to $V_g$) and fitted a sum of the Gaussian functions spaced by $\Delta V_g$s to the measured $I_p$ oscillations to extract the width (the full width at half maximum), $w_p$, of the peak. Figure 4.11(b) shows the dependence of $w_p$ on $N_{eff}$. In the figure, we also plotted the width, $w_s$, of the Coulomb-oscillation peak for $I_s$ (the current peak in the $I$–$V$ curve at $V \simeq 80\mu V$) obtained in the same way as a reference. The increase in the widths, $w_p$ and $w_s$, with the increase in $N_{eff}$ is clear. However, $w_p$ and $w_s$ behave in a different fashion, and $w_p$ increases more rapidly than $w_s$ with the increase in $N_{eff}$.

We also plotted normalized peak and valley currents of the Coulomb oscillation as functions of $N_{eff}$ up to $N_{eff} = 10$ for samples 1 and 3 in Fig. 4.11(c). Here, the valley current ($I_{pv}$) means the lowest current of the Coulomb oscillation curve. We used $N_{eff} I_{pp1}$ as a normalization factor here. The nearly linear scaling of $I_{pp}$

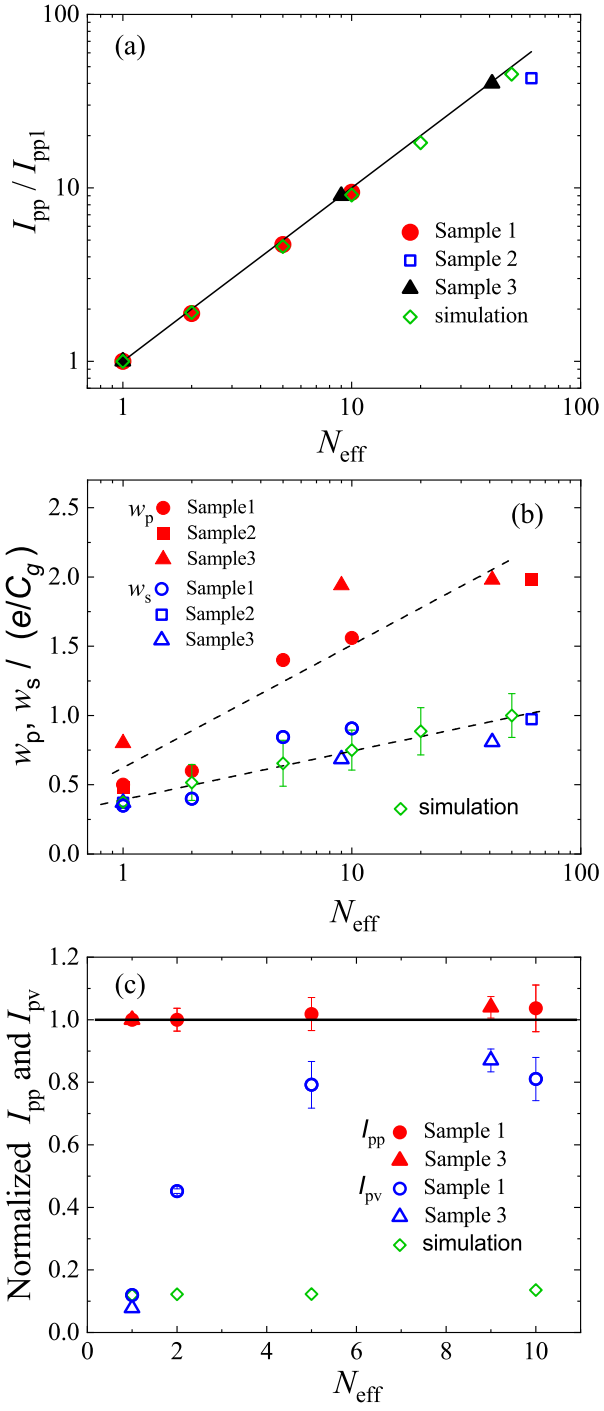


**Figure 4.11:** (a) Dependence of the normalized supercurrent peak $I_{pp}$ on $N_{eff}$ for three samples. The normalization factor is $I_{pp1}$, i.e., $I_{pp}$ for the single SCPT. The solid line indicates the dependence $I_{pp} = N_{eff} I_{pp1}$. Simulation results assuming random offset charges with a standard deviation of $0.22\,e$ are also plotted. (b) dependence of the width $w_p$ of the Coulomb-oscillation peak of $I_p$ on $N_{eff}$ for three samples. The width is in the unit of induced-charge number. $N_{eff}$ dependence of similar width for $I_s$, $w_s$, as well as simulation results with random offset charges for $w_s$ are also plotted. The broken lines are guides for the eyes. (c) Normalized $I_{pp}$ and $I_{pv}$ as functions of $N_{eff}$ for sample 1 and 3. The normalization factor is $N_{eff} I_{pp1}$.The solid line indicates $I_{pp} = N_{eff} I_{pp1}$. Simulation results for $I_{pv}$ with random offset charges are also plotted.

with respect to $N_{\mathrm{eff}}$ is also clear with this plot, and it is also observed that $I_{\mathrm{pv}}$ systematically increases rapidly with the increase in $N_{\mathrm{eff}}$ decreasing the relative oscillation amplitude.

### 4.3.3 Modulability of the supercurrent

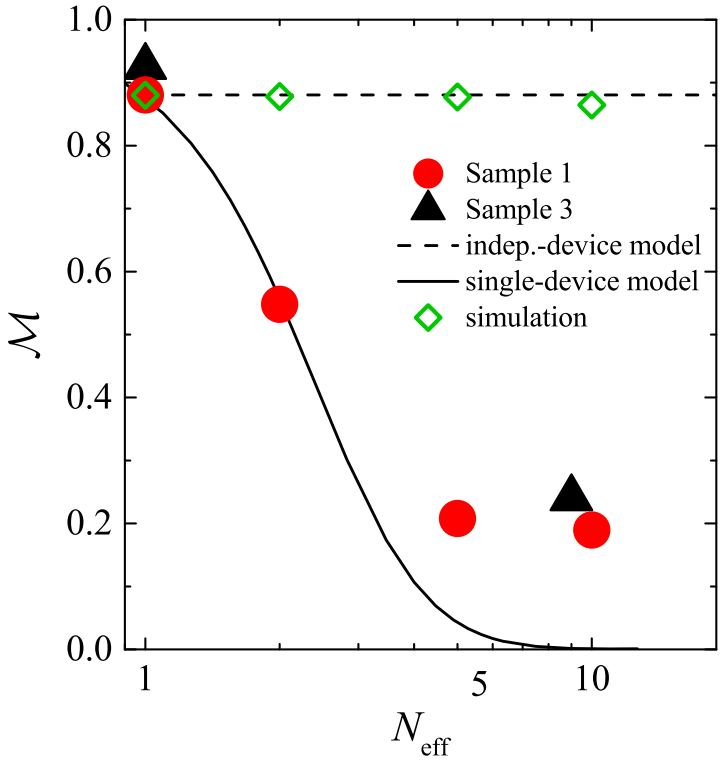


**Figure 4.12:** Dependence of the modulability $\mathcal{M}$ on the number $N_{\mathrm{eff}}$ of parallel SCPTs for samples 1 and 3. The broken and solid lines show the dependences for the independent-device and single-device models for sample 1, respectively. Simulation results assuming only the random offset-charge effect are also plotted showing almost negligible contribution to the modulability decrease.

Here, we define the modulability of the supercurrent, $\mathcal{M}$, as the oscillation amplitude $\Delta I_{\mathrm{p}} = I_{\mathrm{pp}} - I_{\mathrm{pv}}$ divided by $I_{\mathrm{pp}}$: $\mathcal{M} = \Delta I / I_{\mathrm{pp}}$. Figure 4.12 shows a semi-log plot of the dependence of $\mathcal{M}$ on $N_{\mathrm{eff}}$ for samples 1 and 3. We observe that the modulability of the supercurrent with the gate voltage decreases nearly logarithmically with the increase in $N_{\mathrm{eff}}$.

## 4.4 Discussion

### 4.4.1 Offset charge

A possible reason for the increase in the Coulomb-oscillation peak width for the multiple parallel SCPTs is the existence of random offset charges, $q_0$, in the device. They may shift the phases of the Coulomb oscillations of the individual SCPTs, widening oscillation current peak. However, the observed nearly linear dependence of $I_{\rm pp}$ on $N_{\rm eff}$ contradicts with this scenario. Further, if the random offset charges are the main source for the widening of the peak width, the dependences of the widths $w_{\rm p}$ and $w_{\rm s}$ should show the same behavior quantitatively, however the observed results in Fig. 4.11(b) show different behaviors for $w_{\rm p}$ and $w_{\rm s}$.

Because, if the offset charges are randomly distributed, we can not observe any $2e$ ($e$) periodic modulation of $I_{\rm p}$ ($I_{\rm s}$) for large $N_{\rm eff}$. Thus, we assumed a normal distribution of random offset charges with a mean offset charge $\bar{q}_0 = 0$ and a standard deviation $\sigma_q$. Because $I_{\rm s}$ showed an $e$ periodic Coulomb oscillations [Fig. 4.6(c)], it involves a quasiparticle tunneling [14] which is a stochastic process, the observed $I_{\rm s}$ for multiple parallel SCPTs is expected to be a simple addition of the currents in either SCPTs, and the increase in the width $w_{\rm s}$ is expected to be mostly caused by the random offset charges. Thus, we simulated the $N_{\rm eff}$ dependence of $w_{\rm s}$ to obtain the specific $\sigma_q$ value for the samples. (See below for the detail.) We obtained a result, $\sigma_q = 0.22\,e$, to reproduce the measured results as plotted in Fig. 4.11(b) ($\diamond$).

With this offset-charge distribution, we simulated the behavior of $I_{\rm pp}$. As shown in Fig. 4.11(a) ($\diamond$), we obtained a nearly linear dependence of $I_{\rm pp}$ on $N_{\rm eff}$, which is consistent with the experimentally observed result. We also estimated $I_{\rm pv}$ from the simulation results and plotted them in Fig. 4.11(c) ($\diamond$). The simulated $I_{\rm pv}$ shows only small increase with the increase in $N_{\rm eff}$. Accordingly, the simulated modulability $\mathcal{M}$ also shows only small dependence on $N_{\rm eff}$ as plotted in Fig. 4.12 ($\diamond$).

Thus, the effect of the random offset charges are effectively small, and there should be another origin for the rapid increases in $w_{\rm p}$ and $I_{\rm pv}$ with the increase in $N_{\rm eff}$. These two aspects are the features of the expected origin. Zorin theoretically calculated the Coulomb oscillation of $I_{\rm p}$ of a single SCPT and demonstrated that,

with the increase in the $E_{\rm J}/E_{\rm c}$ ratio, the valley current $I_{\rm pv}$ increases and the width of the Coulomb oscillation peak increases [17].

### Simulation method of the effect of the random offset charges

We assumed a shape function $f^{(\rm s)}(q_g)$ of $q_g = C_g V_g$ for the current peak centered at $q_g = 0$ in the Coulomb oscillation of $I_{\rm s}$ of a single SCPT. If an offset charge $q_0$ exists in the island, the function will be shifted by this amount to give a shape $f^{(\rm s)}(q_g - q_0)$ for the current peak which centers at $q_g = q_0$. For $N$ parallel SCPTs with random offset charges $q_{0i}$ $(i = 1, \cdots, N)$, the shape of the current peak will become

$$f_N^{(s)}(q_g) = \sum_{i=1}^{N} f^{(\rm s)}(q_g - q_{0i}). \tag{4.1}$$

We assumed a normal probability distribution for $q_0$ with a standard deviation of $\sigma_q$ as described in the main text:

$$p(q_0) = \frac{1}{\sqrt{2\pi}\,\sigma_q} \exp\left(-\frac{q_0^2}{2\sigma_q^2}\right). \tag{4.2}$$

We numerically generated 1000 random offset charges $q_{0i}$ that obey the above distribution, made peak shapes $f^{(\rm s)}(q_g - q_{0i})$ $(i = 1, \cdots, 1000)$ and made $f_N^{(\rm s)}(q_g)$ by taking $N$ (= 2, 5, 10, 20, and 50) from the generated $f^{(\rm s)}(q_g - q_{0i})$ and making the sum of them according to (4.1). For the generation of $q_{0i}$, we used the transformation [59, 60]

$$\sigma_q \sqrt{-2 \ln U_1} \cos(2\pi\, U_2). \tag{4.3}$$

with two independent, uniformly distributed random draws on (0,1), $U_1$ and $U_2$.

As a shape function $f^{(\rm s)}$, we used a Gaussian function fitted to the current peak of the single SCPT. With the generated $f_N^{(\rm s)}$ curves ($N$=2, 5, 10, 20, and 50), we calculated their full width at half maximum, $w(N)$. We produced 100 $f_N^{(\rm s)}$'s for each $N$ to obtain the average $\bar{w}(N)$. Then we compared $\bar{w}(N)$ with the measured result and adjusted $\sigma_q$ so that $\bar{w}(N)$ followed the straight line fitted to the measured $w_{\rm s}(N_{\rm eff})$ in Fig. 4.5 (b) (the lower broken line) within a 5% error for all the points. The obtained result for $\sigma_q$ is $\sigma_q = 0.22\,e$.

Then, we also assumed as a shape function for $I_{\rm p}$, $f^{(\rm p)}$, a Gaussian function in

the same way as shown in Fig. 4.7, generated 100 $f_N^{(\mathrm{p})}$'s for $N$=2, 5, 10, 20, and 50 using the same distribution of the offset charge with $\sigma_q = 0.22\,e$ as shown in Fig. 4.8, and calculated the average and the standard deviation of $I_{\mathrm{pp}}$ of them for each $N$ [the plot points ($\diamond$) in Fig. 4.5 (a)]. Finally, using typical $f_N^{(\mathrm{p})}$ curves for each $N$ that had $I_{\mathrm{pp}}$ value of the obtained average, we estimated the $I_{\mathrm{pv}}(N)$ values [the plot points ($\diamond$) in Fig. 4.5 (c)].

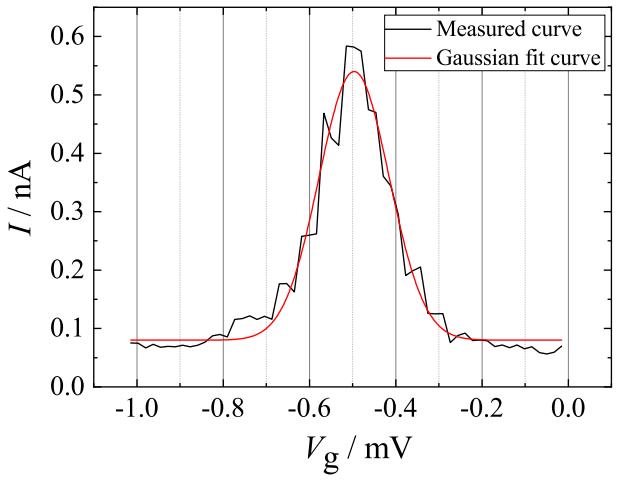


**Figure 4.13:** (a) The Gaussian fit of the shape of the current peak to the measured current peak $I_{\mathrm{p}}$.

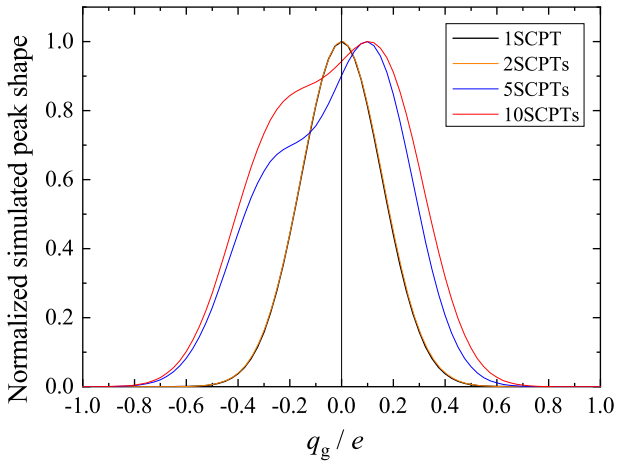


**Figure 4.14:** Examples of the simulated peak curves for the parallel $N_{\mathrm{eff}}$ SCPTs with the standard deviation for the distribution $\sigma_{\mathrm{q}} \simeq 0.22e$.

### 4.4.2 Charge-state fluctuation

At the valley of the Coulomb oscillation, the most probable charge state is fixed by the gate voltage in terms of the charging effect with the charging energy, $E_c(2n - C_gV_g/e)^2$ with $n$ being an integer corresponding to the number of excess Cooper pairs in the island. The valley current $I_{pv}$ is induced because of fluctuation of the charge state, such as caused by the Josephson coupling between the electrodes. Thus, the observed increase in $I_{pv}$ as a function of $N_{eff}$ indicates the increase in the charge-state fluctuation of each SCPT with the increase in $N_{eff}$.

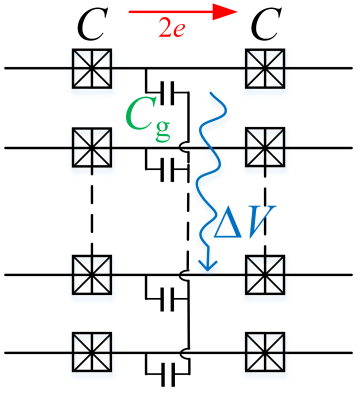


**Figure 4.15:** The electrostatic potential of SCPT's island oscillation induces a gate charge fluctuation on the coupled islands of the neighboring SCPTs of the device structure with the common gate to each SCPT.

In the adopted device structure with the common gate to each SCPT, the islands of the constituent SCPTs are coupled through the gate capacitances to each other. When a supercurrent of a magnitude $i$ passes through one of the SCPT, the electrostatic potential of its island oscillates with the amplitude of $\sim 2e/C_\Sigma$ with an average frequency of $i/2e$. This induces a gate charge fluctuation of the magnitude $\sim e(C_g/C_\Sigma)^2$ on the coupled islands of the neighboring SCPTs according to a circuit analysis. On increasing $N_{eff}$, the fluctuations of $N_{eff} - 1$ neighboring SCPTs add up, and the resultant gate charge fluctuation is enhanced. If the Cooper-pair tunnelings in the different SCPTs of the device are uncorrelated, they will give a charge fluctuation of $\sim \sqrt{N_{eff} - 1}\, e\, (C_g/C_\Sigma)^2$ to each of the SCPTs, resulting in the increase in the valley current.

Thus, the situation of the device can be considered as the one schematically shown in Fig. 4.16(a), and it is between the two limiting models, namely, an inde-

pendent device model in Fig. 4.16(b) and a single-device model in Fig. 4.16(c). The former is the case where all the SCPTs are independent, and the latter is the case where the islands of all the SCPTs are directly connected to each other and make a single superconducting island. In the latter case, the superconducting phase should have a single value over the single island, and the fluctuation of the charge number in each constituent SCPT island becomes $\gg 1$ [61]. In the independent device model without the consideration of the offset charge, the total current is a simple addition of all the currents in the constituent SCPTs. Thus, with $N$ SCPTs, $I_{\mathrm{pp}N} = NI_{\mathrm{pp1}}$ and $I_{\mathrm{pv}N} = NI_{\mathrm{pv1}}$, and the modulability $\mathcal{M}$ has no $N$ dependence (broken line in Fig. 4.12).

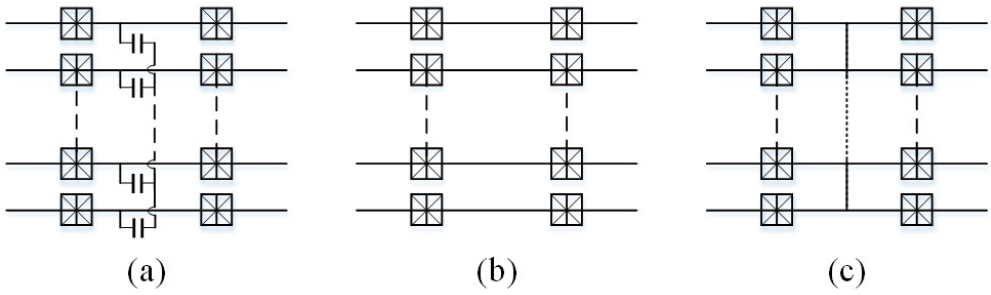


**Figure 4.16:** (a) The equivalent circuit of the actual device situation. All the island electrodes are coupled with each other through the gate capacitances. (b) the independent-device model. All the SCPTs are independent and the total current is a simple sum of the currents in the individual SCPTs. (c) the single-device model. All the islands of the SCPTs are directly connected to each other and make a single island electrode.

In the case of the single-device model with $N$ input (output) junctions, the tunnel resistance between the island and the lead is $R_{\mathrm{T}}/N$ while the capacitance between the island and each lead is $NC$, where $R_{\mathrm{T}}$ and $C$ are tunnel resistance and capacitance of one junction, respectively. Hence, the effective Josephson coupling energy, $E_{\mathrm{J}}^*$, between the island and the lead is $NE_{\mathrm{J}}$, the effective charging energy, $E_{\mathrm{c}}^*$, of the device $E_{\mathrm{c}}^* = E_{\mathrm{c}}/N$, and their ratio becomes $E_{\mathrm{J}}^*/E_{\mathrm{c}}^* = N^2E_{\mathrm{J}}/E_{\mathrm{c}}$. Thus, the charge-state fluctuation of the island grows rapidly with the increase in $N$. We numerically calculated $I_{\mathrm{pp}N}$ and $I_{\mathrm{pv}N}$, and obtained $\mathcal{M}$ as a function of $N_{\mathrm{eff}}$ for this model. (See below for the detail of the calculation method.) The solid line in Fig. 4.12 shows the calculated dependence.

The measured results for $\mathcal{M}$ fall between the two theoretical curves based on the independent- and single-device models. This result supports the viewpoint regarding the actual device to be between the two limiting models. Further, the curve for the single-device model explains the observed tendency of $\mathcal{M}$ quantitatively well. Thus, we can conclude that, in our devices, the charge-state fluctuation caused by the capacitive coupling between the island electrodes increases $I_{\mathrm{pv}}$ and decreases the modulability $\mathcal{M}$ with the increase in $N_{\mathrm{eff}}$.

### Calculation method of the effective number dependence of the modulability for the single-device model

Here we consider a symmetric SCPT that has equivalent small Josephson junctions between the island and the two leads on the basis of the experimental situation. We denote the phase differences across the junctions as $\phi_1$ and $\phi_2$, also the overall phase difference across the two junctions as $\varphi = \phi_1 + \phi_2$ and the semidifference phase $\theta = (\phi_1 - \phi_2)/2$, and the number of excess Cooper pairs in the island, $n$ as in 2.2. The Hamiltonian of a SCPT is expressed as [17]

$$H = \frac{(2ne - q_g)^2}{2C_\Sigma} - E_{\mathrm{J}}(\varphi)\cos\theta \tag{4.4}$$

with

$$E_{\mathrm{J}}(\varphi) = 2E_{\mathrm{J}}\left|\cos\frac{\varphi}{2}\right| \tag{4.5}$$

and $C_\Sigma = 2C + C_g$. The phase $\theta$ and $n$ are canonically conjugated variables $[\hat{\theta}, \hat{n}] = i$, which fluctuate quantum mechanically. By using the charge state $|\mathrm{n}\rangle$ that is an eigen state of $\hat{n}$ and represents the state with $n$ excess Cooper pairs in the island, the Hamiltonian is rewritten as

$$H = E_{\mathrm{c}}\left(2\hat{n} - \frac{q_g}{e}\right)^2 - \frac{E_{\mathrm{J}}(\varphi)}{2}\sum_n(|n+1\rangle\langle n| + |n-1\rangle\langle n|). \tag{4.6}$$

We used this Hamiltonian to calculate the current through the device using $E_{\mathrm{J}}^*$ and $E_{\mathrm{c}}^*$ values of the single-device model for $E_{\mathrm{J}}$ and $E_{\mathrm{c}}$, respectively.

Because the eigen energy is periodically modulated with respect to $q_g$ with a period of $2e$, to calculate the peak (valley) current at $q_g = (2n+1)e$ ($q_g = 2ne$) for

a given $E_{\rm J}^*/E_{\rm c}^*$ value, we took $n = 1$ ($n = 0$) and used eight (seven) lowest-energy charge states with $n = -3, \cdots, 4$ ($n = -3, \cdots, 3$) to express the Hamiltonian as a matrix. We then obtained an expression, $\varepsilon_{\rm p}(\varphi)$ ($\varepsilon_{\rm v}(\varphi)$), of the ground state energy of the system as a function of phase $\varphi$ from the matrix, calculated the current with the relation

$$I(\varphi) = \frac{2e}{\hbar}\frac{\partial \varepsilon}{\partial \varphi},$$

and, then, numerically evaluated its maximum with respect to $\varphi$ to obtain $I_{\rm pp}$ ($I_{\rm pv}$). The modulability was calculated with $\mathcal{M} = (I_{\rm pp} - I_{\rm pv})/I_{\rm pp}$.

### 4.4.3 Possible improvement method

As discussed in the previous subsections, the dominant origin of the rapid increase in $I_{\rm pv}$ when $N_{\rm eff}$ is increased is the enhancement of the charge-state fluctuation via the capacitive coupling between the islands of the SCPTs connected in parallel. Therefore, the reduction of the coupling between the islands may improve the modulability of the supercurrent.

A direct method for this purpose is to reduce the gate capacitance. As discussed in 4.4.2, the magnitude of gate-charge fluctuation is $\sim \sqrt{N_{\rm eff} - 1}\, e\, (C_g/C_\Sigma)^2$ and, thus, proportional to $(C_g/C_\Sigma)^2$. Therefore, the reduction of $C_g$ by decreasing the area of the gate capacitance and/or increasing the thickness of the oxide layer on may effectively decrease the coupling and the gate-charge fluctuation. Recently, a well controlled fabrication of an $Al_2O_3$ layer with the use of atomic layer deposition (ALD) technique in combination with a lithographic process has been realized [62]. One needs caution, however, for the reduction of the area of the gate capacitance too much, because of the increase of a fluctuation of $C_g$ values among the constituent SCPTs.

To substantiate the discussion, we examine the case of sample 1. The original gate capacitance of sample 1 is $C_g = 0.4\,\mathrm{fF}$. If it is decreased by a factor 10 by making the oxide thickness $\sim 50\,\mathrm{nm}$ and the area of the gate capacitance half, for example, $C_g' = 40\,\mathrm{aF}$, and $(C_g'/C_\Sigma')^2/(C_g/C_\Sigma)^2 \simeq 0.015$. Here, the quantity with a prime denotes that after decreasing the gate capacitance. Thus, the expected charge fluctuation $\sqrt{N_{\rm eff} - 1}\, e\, (C_g'/C_\Sigma')^2$ for a single constituent SCPT becomes 1.5%

of the original one, and the charge-state fluctuation should be largely decreased. Conversely, when the original charge fluctuation is acceptable, then we can increase $N_{\rm eff}$ and, therefore, $I_{{\rm pp}N_{\rm eff}} (\simeq N_{\rm eff} I_{\rm pp1})$ with an extension factor $\alpha \sim (C_g/C_g')^4$ by decreasing $C_g'$ with the same level of the charge fluctuation.

Further, when independent gate electrodes can be used, resistive gate electrodes [63] with an impedance $Z$ may improve the situation as shown in Fig. 4.17. Assuming an impedance of the gate terminal to the ground, $Z_0$, the effect of the voltage fluctuations of the other island is decreased by a factor $\sim |Z_0/(Z+Z_0)|$. However, there appears a charging time constant $\tau \sim |Z| C_g$ by introducing a resistive gate electrode. Thus, we should choose suitable combination of $Z$ and $C_g$ for particular applications.

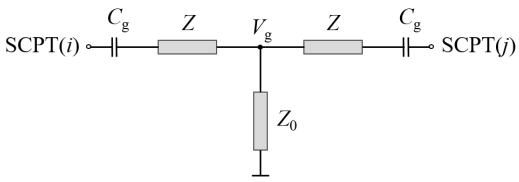


**Figure 4.17:** The assumed circuit of the resistive gate electrodes with an impedance $Z$ to the gate terminal. $Z_0$ is the impedance of the gate terminal to the ground.

In a single SCPT, $\mathcal{M}$ is dominantly determined by the value of $E_{\rm J}/E_{\rm c}$, and $I_{\rm pp1}$ is determined by $E_{\rm J}$, therefore, for a given $\Delta$, by $R_{\rm T}$ [17]. Thus, by decreasing $R_{\rm T}$ and holding the $E_{\rm J}/E_{\rm c}$ value by making the junction capacitance $C$ small at the same time, we can increase $I_{\rm pp1}$ for a single SCPT with a fixed $\mathcal{M}$, or, conversely, by holding $R_{\rm T}$ and decreasing the $E_{\rm J}/E_{\rm c}$, a larger $\mathcal{M}$ with a fixed $I_{\rm pp}$ is obtained. In the literature, a modulation of the supercurrent $I_{\rm pp1} \simeq 10\,{\rm nA}$ with $\mathcal{M} \simeq 0.5$ in a single SCPT consisting of Al/$\rm AlO_x$/Al junctions was demonstrated for $R_{\rm T} \lesssim R_{\rm Q} = h/(2e)^2$, $E_{\rm J}/E_{\rm c} \simeq 1$ and a comparable $C$ value with our samples [51]. Thus, adjustment of the sample parameters would readily realize $I_{\rm pp1} \simeq 10\,{\rm nA}$ and $\mathcal{M} \sim 1.0$ for a single SCPT. On the basis of our experimental results and the discussions above, two such SCPTs in parallel with the same structure in our experiment will manipulate a supercurrent $I_{\rm pp2} \simeq 20\,{\rm nA}$ with $\mathcal{M} \simeq 0.5$. Decreasing $C_g$ by a factor 10 with holding other parameters, for example, would extend the number of SCPTs by a factor $\alpha > 1000$ retaining $\mathcal{M} \sim 0.5$. This indicates a possibility to obtain the

gate-modulable supercurrent above 10 $\mu$A. The effect of random offset charges, on the other hand, remains small even for a large number of parallel SCPTs as far as their distribution is a normal distribution and its standard deviation is as small as that obtained in this work. Our simulation on the random offset charges for sample 1 typically gives $\mathcal{M} > 0.8$ even for $N_{\mathrm{eff}} \geq 100$.

## 4.5 Conclusions

We examined the scalability of the supercurrent $I_{\mathrm{p}}$ that was modulated with the SCPT structure using parallelly connected multiple SCPTs that had a common gate electrode. We found that the maximum supercurrent $I_{\mathrm{pp}}$ that flew through $N$ parallel SCPTs was scaled up almost linearly with the increase in $N$ for $N \lesssim 60$ and that the gate voltage modulated $I_{\mathrm{p}}$ as in a single SCPT to give the Coulomb oscillation. However, the width of the current peak of the Coulomb oscillation as well as the relative magnitude of valley current $I_{\mathrm{pv}}/I_{\mathrm{pp}}$ of the oscillation increased with the increase in $N$. The resultant modulability $\mathcal{M}$ of $I_{\mathrm{p}}$ showed a nearly logarithmic decrease with the increase in $N$.

By comparing the observed results of $\mathcal{M}(N)$ with a theoretical calculation for the limiting single-device model, we showed that the main origin for the reducting of modulability is the charge-state fluctuation caused by the capacitive coupling between the islands of the SCPTs . The effect of random offset charges, that could be a possible origin of the reduction of modulability, on the other hand, turned out to be small with the used device structure. We discussed a possible improvement method for $\mathcal{M}$ by decreasing the coupling gate capacitance. With careful design of the gate capacitance, the parallely connected multiple SCPTs with a common gate can provide a way to enlarge the well modulable supercurrent by orders larger than that of a single SCPT.

# Chapter 5

# Coherence of the supercurrent through a single Cooper-pair transistor and its modulability in a dc SQUID loop

## 5.1 Introduction

This chapter presents a study of the characteristics of SCPT, when it is inserted in a SQUID-like loop. The aim of this study is to examine the phase coherence through the SCPT when the Josephson current flows and to examine the modulation of supercurrent of SCPT in the loop with gate voltage. Because the RSFQ circuits and SQUID circuits use superconducting loop structures, understanding the behavior of the SCPT in such a loop structure is important for its combination with other superconducting electronics circuits. We embedded a SCPT in one branch of a dc-SQUID loop and measured the $I$–$V$ characteristic of the loop with the applied magnetic field and gate voltage as parameters.

## 5.2 The supercurrent as a function of gate voltage in the loop

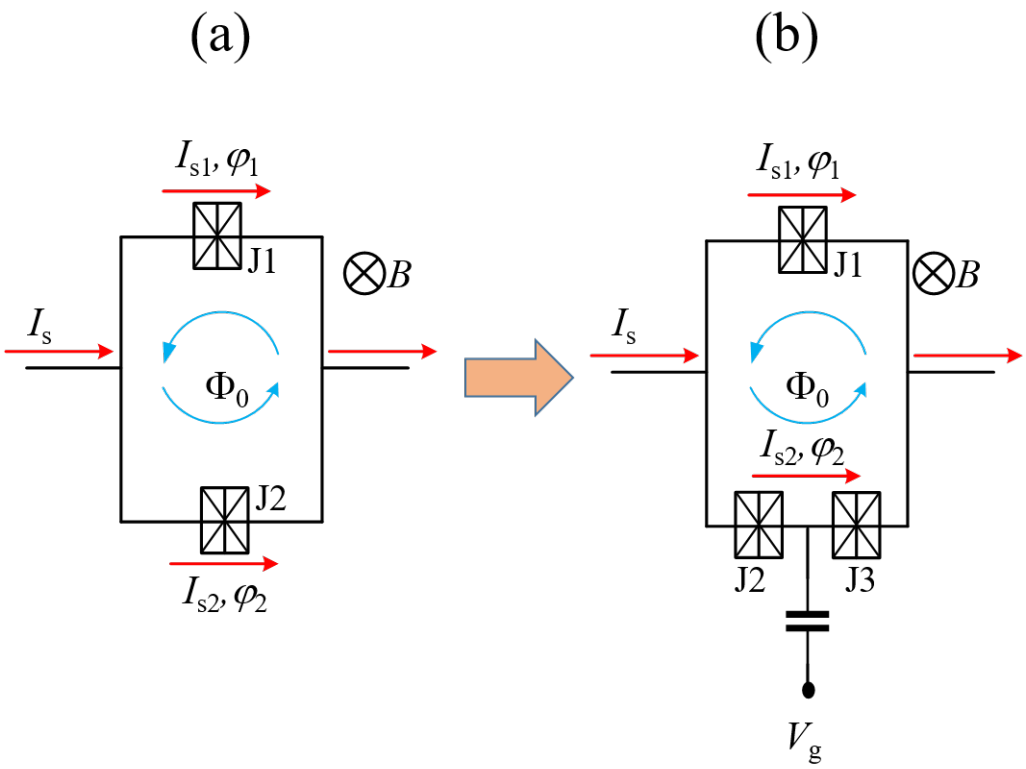


**Figure 5.1:** (a) The equivalent circuit of dc-SQUID with two Josephson junction. (b) The equivalent circuit of a dc-SQUID-like loop where a SCPT is embedded into one branch.

As explained in 2.3.1, the total Josephson current through the simple dc-SQUID circuit as shown in Fig. 5.1(a) is

$$I_s = I_{s1} + I_{s2} = I_{c1} \sin \varphi_1 + I_{c2} \sin \varphi_2, \tag{5.1}$$

where $I_{c1}$ and $I_{c2}$ are the critical current of the Josephson junctions 1 and 2 respectively. $\varphi_1, \varphi_2$, are the phase difference across the junctions 1 and 2 respectively.

If the flux $\Phi$ is threading in the loop due to an the external flux $\Phi_{ext}$, and $I_{c1} = I_{c2} = I_c$, the maximum supercurrent is given by

$$I_s^{max} = 2I_c \left| \cos \pi \frac{\Phi_{ext}}{\Phi_0} \right|. \tag{5.2}$$

The relation between the maximum supercurrent and the external flux for dc-SQUID with two Josephson junction is shown in Fig. 2.10.

Next, we consider the case where a SCPT is embedded in one of the branches of the SQUID instead of a single junction as shown in Fig. 5.1(b). We call the two junctions in the SCPT as junction 2 and 3, and assume that the Josephson coupling energies of the two junctions to be $E_{\rm J2}$ and $E_{\rm J3}$, respectively, the phase differences across the two junctions to be $\varphi_{\rm J2}$ and $\varphi_{\rm J3}$, respectively, and $\varphi_{\rm J2} + \varphi_{\rm J3} = \varphi_2$. The junctions have capacitances $C_2$ and $C_3$, and the gate capacitance is $C_g$. The sum of them is $C_\Sigma (= C_2 + C_3 + C_g)$ When $E_{\rm J2,J3} \ll E_{\rm c}$, a simple expression for $I_{\rm s2}$ is obtained with a perturbation theory [18]:

$$I_{\rm s2} = \frac{2e}{\hbar} \frac{E_{\rm J2} E_{\rm J3} \sin\varphi_2}{4\sqrt{(eC_{\rm g}/C_\Sigma)^2 (V_{\rm g} - V_{\rm g}^{(n)})^2 + E_{\rm J}^2(\varphi_2)/4}}, \tag{5.3}$$

where $E_{\rm J}(\varphi_2) = [E_{\rm J2}^2 + E_{\rm J3}^2 + 2E_{\rm J2}E_{\rm J3}\cos\varphi_2]^{1/2}$.

We assume here $E_{\rm J2} = E_{\rm J3} = E_{\rm J}$ for simplicity, then we obtaine $E_{\rm J}(\varphi_2) = 2E_{\rm J}\,|\cos(\varphi_2/2)|$. The right-hand side is equal to $2E_{\rm J}\cos(\varphi_2/2)$, for $0 \le \varphi_2 \le \pi$, and to $-2E_{\rm J}\cos(\varphi_2/2)$, for $\pi \le \varphi_2 \le 2\pi$. Replacing of $E_{\rm J}(\varphi_2)$ in eq. (5.3), the current $I_2$ is

$$\begin{aligned} I_{\rm s2} &= \left(\frac{eE_{\rm J}}{2\hbar}\right) \sin(\varphi_2/2), \quad 0 \le \varphi_2 \le \pi \\ &= -\left(\frac{eE_{\rm J}}{2\hbar}\right) \sin(\varphi_2/2), \quad \pi \le \varphi_2 \le 2\pi. \end{aligned} \tag{5.4}$$

In eq. (5.4), the supercurrent $I_{\rm s2}$ through the SCPT is determined with respect to total phase difference $\varphi_2$ of the two Josephson junction in the SCPT. The $I_{\rm s2}$ characteristic is shown in Fig. 5.2,

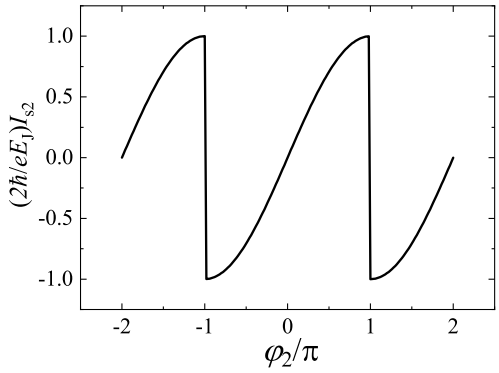


**Figure 5.2:** The characteristic of the supercurrent through the SCPT with respect to $\varphi_2$.

When an external magnetic flux is applied through the loop, a relationship between $\varphi_1$ and $\varphi_2$ becomes

$$\varphi_2 - \varphi_1 = 2\pi n + 2\pi \frac{\Phi_{\rm ext}}{\Phi_0}, \tag{5.5}$$

where $\Phi_0 = h/2e$ is the flux quantum. The total current through the loop is

$$I_{\rm s} = I_{\rm c1} \sin\left(\varphi_2 - \frac{2\pi\Phi_{\rm ext}}{\Phi_0}\right) + I_{\rm c2} \sin\left(\frac{\varphi_2}{2}\right), \tag{5.6}$$

where $I_{\rm c2}$ is equal to $eE_{\rm J}/2\hbar$ for $0 \leq \varphi_2 \leq \pi$, and to $-eE_{\rm J}/2\hbar$ for $\pi \leq \varphi_2 \leq 2\pi$. With a external magnetic flux density $B_{\rm ext}$, $\Phi_{\rm ext}/\Phi_0$ is expressed as $B_{\rm ext}/B_0$, where $\Phi_0 = B_0 A$ with $A$ the area of the loop. Thus the total Josephson current (Fig. 5.1(b)) is periodic in the applied magnetic field, $B_{\rm ext}$. At zero voltage, the critical supercurrent $I_{\rm s}^{\rm max}$ is found by maximizing eq. (5.6) with respect to $\varphi_2$.

Figure 5.3 shows the calculated result of the critical supercurrent $I_{\rm s}^{\rm max}$ through the loop as a function $B_{\rm ext}$. The red curve shows the case where $I_{\rm c1} = I_{\rm c2}$ and the blue curve corresponds to the case with $I_{\rm c2} = 0$. The green curve shows the case in between. For the case with $I_{\rm c2} = 0$, it can be regarded that the supercurrent loop is open in one branch because magnetic field modulation is absent. Thus, by using a SCPT with a large modulability $\sim 1$, one may open and close the superconducting loop with a gate voltage. We examine this supercurrent-switching function of a SCPT in this chapter.

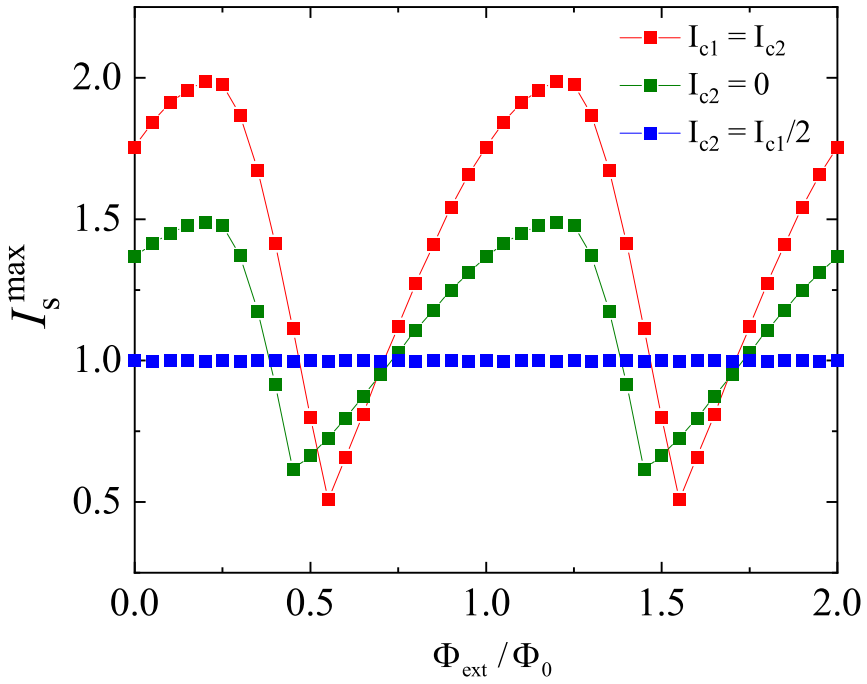


**Figure 5.3:** The calculated behavior of the critical supercurrent in the SCPT-embedded loop as a function of the external magnetic flux.

## 5.3 Experimental methods

We used a dc SQUID structure with one of the Josephson junction replaced with a SCPT. We fabricated the two samples of the SQUID loop with the inserted SCPT, i.e. sample A and sample B. The superconducting loop area is 800 $\mu$m$^2$. The size of Al/AlO$_x$/Al Josephson junctions of the SCPT for both sample were approximately 0.02 $\mu$m$^2$ and island's dimensions were 200 nm wide $\times$ 1 $\mu$m long. The gate electrode in central position was 1 $\mu$m far from the island. The single Josephson junctions size of another branch in loop for samples A and B, were approximately 0.02 $\mu$m$^2$ and 0.0048 $\mu$m$^2$, respectively. The design pattern of the samples are shown in Fig. 5.4 for sample A and in Fig. 5.5 for sample B. In sample A, the size of the three Josephson junctions were designed to be the same in order for all the junctions to have the same $E_J$ value, while, in sample B, we designed the size of the single junction half of those of the SCPT to balance the resistance of the two branches so that $E_J$ for the SCPT junction is twice that of the single junction. We can also compare the cases with different $E_J/E_c$-ratio ranges with the two samples.

In the measurement, a bias voltage was applied to the SQUID loop symmetrically with respect to the ground using a symmetrized voltage source, and the four terminal probes scheme was used for the measurement of $I - V$ characteristics of the circuit. A superconducting solenoid was used to apply a magnetic field $B$ perpendicular to the sample substrate for the SQUID loop. This experiment measured the periodic change in supercurrent through the SQUID loop with magnetic field $B$ and the modulation of supercurrent of SCPT in the loop with a gate voltage.

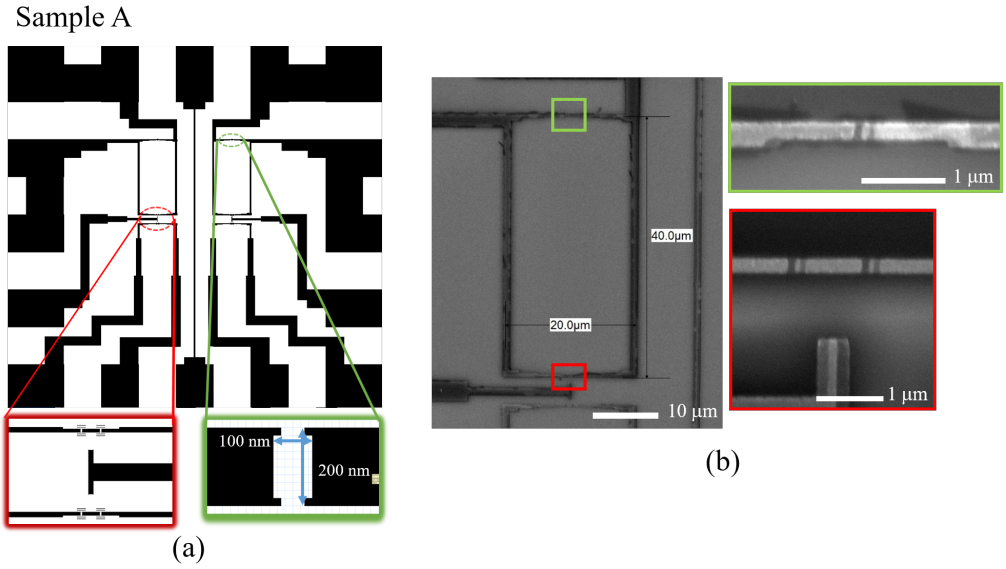


**Figure 5.4:** The pattern design of sample A (a) and (b) Scanning electron microscope (SEM) micrograph of SCPT and single Josephson junction in another branch of SQUID loop.

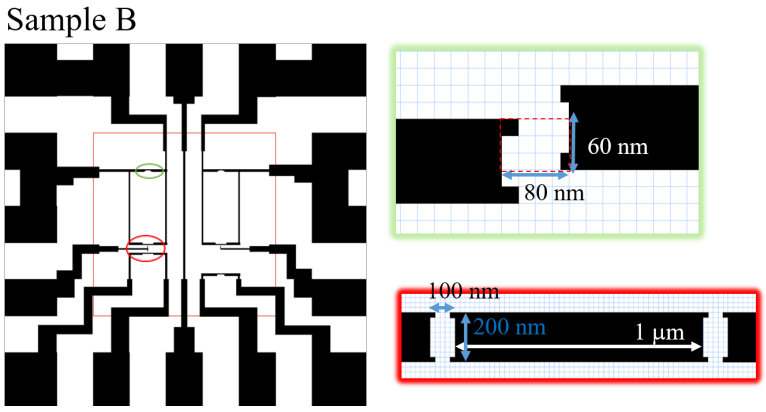


**Figure 5.5:** The pattern of sample B with SCPT and single Josephson junction in another branch of SQUID loop: size design.

## 5.4 Experimental results

Table 5.1: Parameters of the samples: tunnel resistance $R_{\mathrm{T}}$ of the junction, Josephson coupling energy $E_{\mathrm{J}}$ of the junction, charging energy $E_{\mathrm{c}}$, the $E_{\mathrm{J}}$ to $E_{\mathrm{c}}$ ratio, junction capacitance $C$, gate capacitance $C_g$ and junction area $A$

| sample | device | $R_{\mathrm{T}}$ (kΩ) | $E_{\mathrm{J}}$ ($\mu$eV) | $E_{\mathrm{c}}$ ($\mu$eV) | $E_{\mathrm{J}}/E_{\mathrm{c}}$ | $C_g$ (aF) | $A$ ($\mu$m$^2$) |
|---|---|---|---|---|---|---|---|
| A | single junction | 10.7 | 60 | 160 | 0.37 | | 0.02 |
| | SCPT | 10.7 | 60 | 80 | 0.74 | 16 | 0.02 |
| B | single junction | 76.7 | 9 | 200 | 0.05 | | 0.0048 |
| | SCPT | 40.1 | 17 | 64 | 0.26 | 26 | 0.02 |
| | indep. double junction | 40.1 | 17 | 64 | 0.26 | - | 0.02 |

The parameters of all devices are shown in Table 5.1. An asymptotic $I-V$ curve at high bias ($V \gg 2\Delta/e \simeq 400\mu$V) allow us to estimate the resistance of the junctions of the loop and the junction areas. The gate capacitance, $C_{\mathrm{g}}$, was obtained from the $2e$ periodic Coulomb oscillation curves with a relation $C_{\mathrm{g}} = 2e/\Delta V_{\mathrm{g}}$, where $\Delta V_{\mathrm{g}}$ is the period voltage on the Coulomb oscillation curve. The magnitude of the superconducting gap of the Al electrodes is 197 $\mu$eV for sample A and 208 $\mu$eV for sample B, which was derived from the differential conductance characteristics and the offset voltage.

Figures 5.6 and 5.7 show respectively, the $I-V$ characteristic and the Coulomb oscillation of the SQUID loop with SCPT at $B$=0 G and $T$=75 mK. The supercurrents for the loops are about 10 nA in Fig. 5.6(b) and 120 pA in Fig. 5.7(b) for sample A and B, respectively. Gate modulation of the supercurrent of the loop with an embedded SCPT in one branch for samples A and B at $B = 0$ G are shown in Fig. 5.6(c) and Fig. 5.7(c), respectively. Both show Coulomb oscillations with the periodicity of $2e$ in $C_{\mathrm{g}}V_{\mathrm{g}}$.

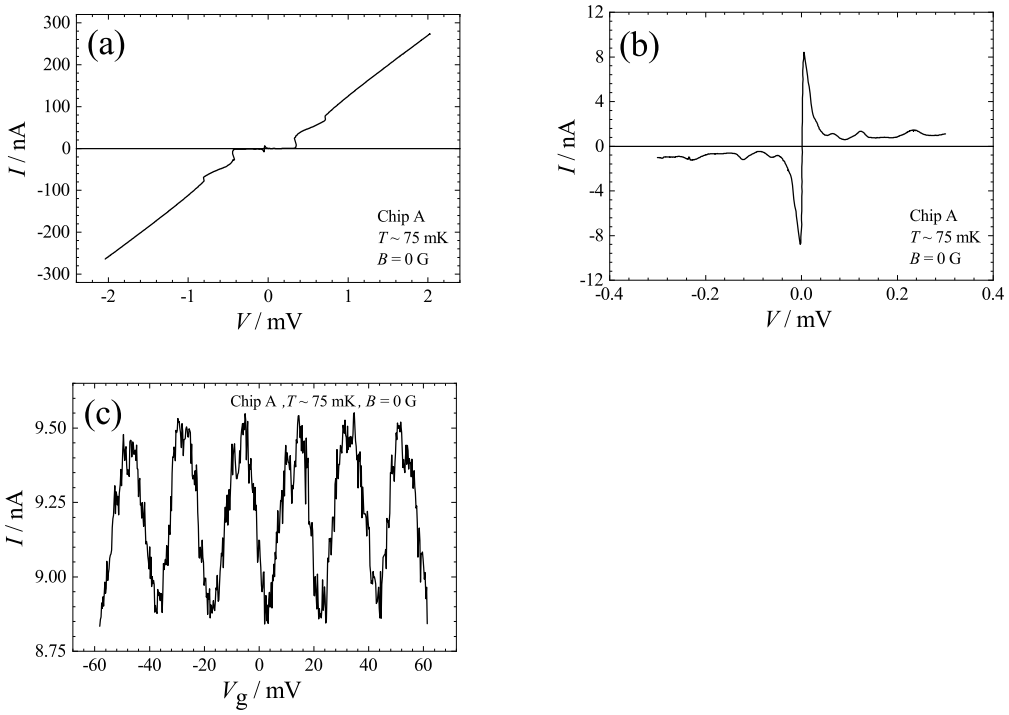


**Figure 5.6:** The $I - V$ characteristic (a),(b) and the Coulomb oscillation (c) of SQUID loop with an embed SCPT in one branch for sample A.

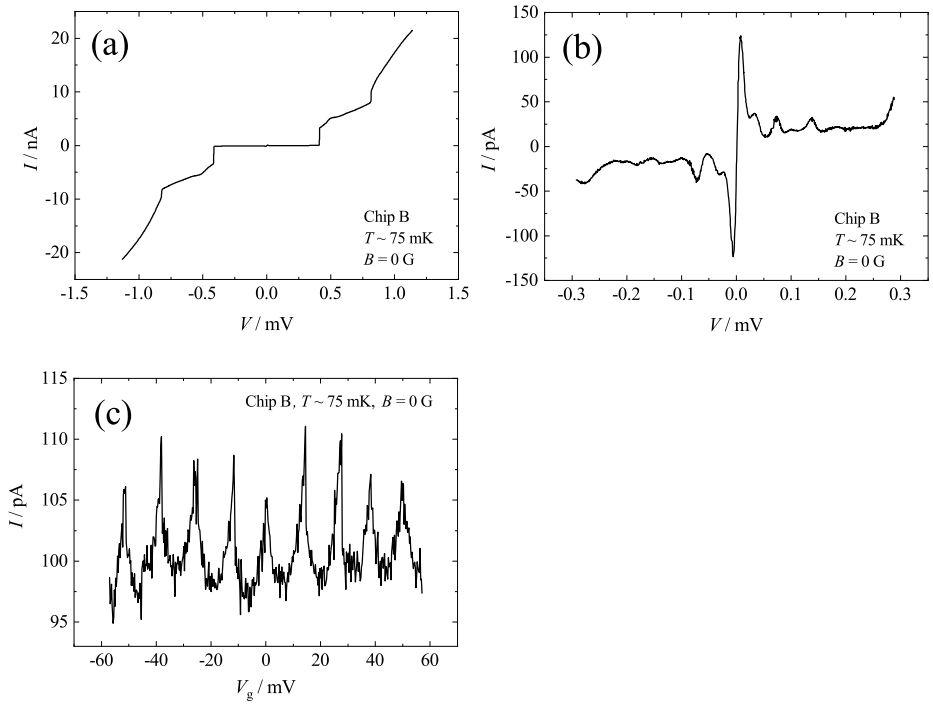


**Figure 5.7:** The $I - V$ characteristic (a),(b) and the Coulomb oscillation (c) of SQUID loop with an embed SCPT in one branch for sample B.

Figures 5.8 and 5.9 show the magnetic field dependence of the supercurrent through the SCPT-embedded loop in samples A and B, respectively. They show clear periodic dependences on $B$ with a period $\Delta B$ of 0.0258 G. With the fabricated area of the loop $A_{\rm loop} = 800\ \mu{\rm m}^2$, $\Delta B A_{\rm loop} = 2.06 \times 10^{-15}$ Wb, which is close to $\Phi_0$. Thus we confirm a periodic modulation of supercurrent through the loop with a period of applied flux of $\Phi_0$. This indicates that the supercurrent through the SCPT maintains the superconducting coherence when a change in gate voltage modulation.

The fixed two values of the gate voltage in each case correspond to the states where the SCPT is turned on and off, namely, with maximum (ON state) and minimum (OFF state) supercurrent through the loop. In sample A, the difference in the supercurrent between ON and OFF states is 1 nA. In sample B, it is 10 pA. The modulation with respect to the gate voltage is not as large as we had expected even for the sample B where the junctions of the SCPT have $E_{\rm J}$ approximately twice that of the single junction and the $E_{\rm J}/E_{\rm c}$ ratio of the SCPT is as small as 0.26. We will discuss this point in the next section.

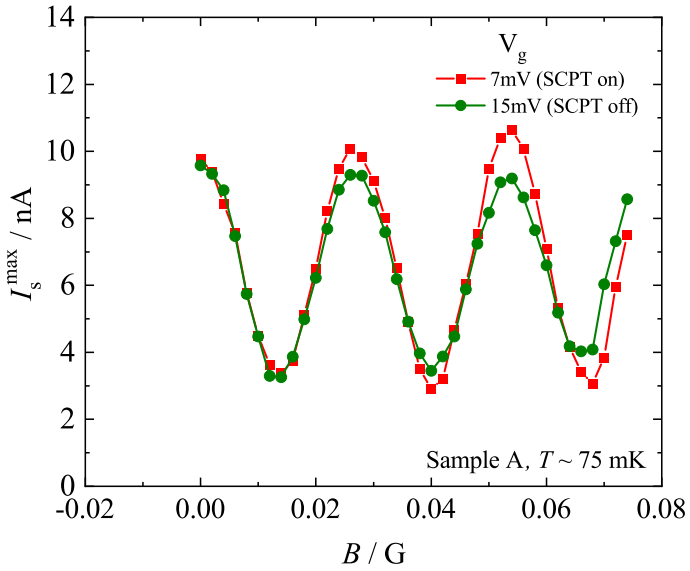


**Figure 5.8:** Sample A, the $I_s^{max} - B$ characteristics of loop which has a SCPT in one branch showing the periodic dependence on applied magnetic field with the current modulation at the gate voltage $V_g$ with the fix values of gate voltage $V_g$= 7 and 15 mV.

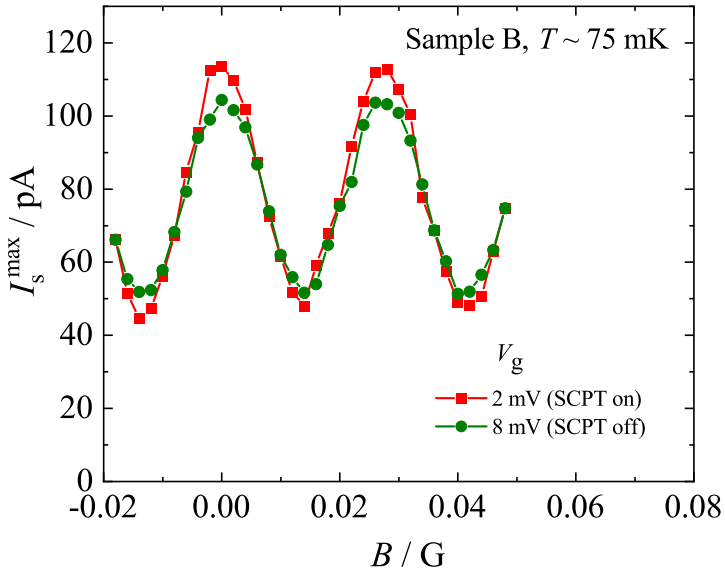


**Figure 5.9:** Sample B, the $I_s^{max} - B$ characteristics of loop which has a SCPT in one branch showing the periodic dependence on applied magnetic field with the current modulation at the gate voltage $V_g$ with the fix values of gate voltage $V_g$= 2 and 8 mV.

## 5.5 Discussion

### Theoretical consideration on the SCPT-embedded loop device

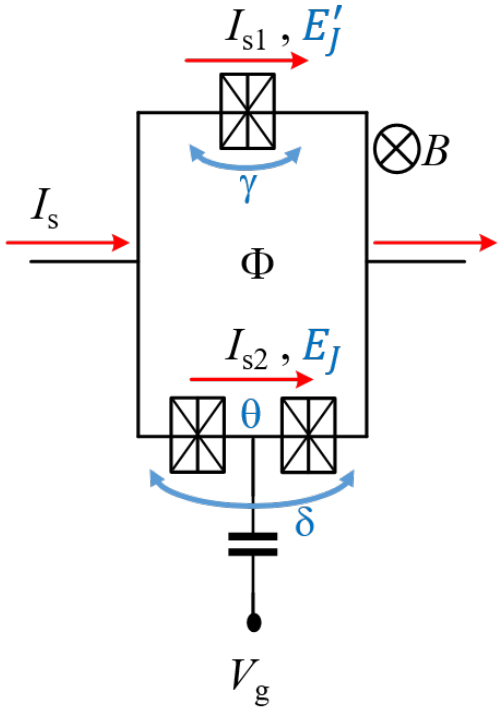


**Figure 5.10:** The defined theoretical parameters of the device.

The experimentally observed results for the gate modulation of the $I_s - B$ characteristics did not show a large change in $I_s$ due to the switching of the SCPT. We try to understand its origin here. In the model in 5.2, the current $I_{s2}$ was derived on the basis of a perturbation theory assuming $E_J/E_c \ll 1$. This means that only neighboring charge states of the most stable charge state are considered. In order to involve more charge states, we consider the whole system theoretically assuming two junctions in the SCPT are identical. The Hamiltonian of the SCPT-embedded loop device can be expressed

$$H = 4E_c(n - n_g)^2 - E_J \cos(\delta/2)\cos\theta - E_J{}' \cos\gamma. \tag{5.7}$$

The first two terms are the electrostatic and the Josephson coupling Hamiltonians of the SCPT in the loop. The third term is the Josephson coupling Hamiltonian of the single junction in the loop with $E_{\mathrm{J}}'$ being the Josephson coupling energy of the single junction. The phases are defined as in Fig. 5.10. We normalize the Hamiltonian with $4E_{\mathrm{c}}$ as follows.

$$\begin{aligned}\frac{H}{4E_{\mathrm{c}}} &= (n-n_{\mathrm{g}})^2 - \frac{E_{\mathrm{J}}}{4E_{\mathrm{c}}}\cos(\delta/2)\cos\theta - \frac{E_{\mathrm{J}}{}'}{4E_{\mathrm{c}}}\cos\gamma \\ &= (n-n_{\mathrm{g}})^2 - A\cos(\delta/2)\cos\theta - B\cos\gamma.\end{aligned} \tag{5.8}$$

A and B are defined to $E_{\mathrm{J}}/4E_{\mathrm{c}}$ and $E_{\mathrm{J}}{}'/4E_{\mathrm{c}}$, respectively. We define a normalized Hamiltonian of the SCPT part as,

$$\begin{aligned}E \equiv \frac{H}{4E_{\mathrm{c}}} + B\cos\gamma &= (n-n_{\mathrm{g}})^2 - A\cos(\delta/2)\cos\theta \\ &= (n-n_{\mathrm{g}})^2 - F(\delta)(e^{i\theta}+e^{-i\theta}).\end{aligned} \tag{5.9}$$

$F(\delta)$ is defined as $(A\cos(\delta/2))/2)$. Here, we consider a magnetic flux $\Phi$ and use a phase relation $\delta = \gamma + \phi$, $\phi = 2e\Phi/\hbar = 2\pi\Phi/\Phi_0$. The Hamiltonian matrix with four charge states $|\text{-}1\rangle$, $|0\rangle$, $|1\rangle$, $|2\rangle$ of the right term of eq. (5.9),

$$\begin{bmatrix} (-1-n_{\mathrm{g}})^2 & -F & 0 & 0 \\ -F & n_{\mathrm{g}}^2 & -F & 0 \\ 0 & -F & (1-n_{\mathrm{g}})^2 & -F \\ 0 & 0 & -F & (2-n_{\mathrm{g}})^2 \end{bmatrix}. \tag{5.10}$$

Here, $|\,n\rangle$ means the charge state where $n$ excess Cooper pairs are in the island.

We calculated the eigenvalues of the Hamiltonian matrix $\epsilon(\delta)$ by using Mathematica, obtained the ground state energy function $\varepsilon_0$,

$$\varepsilon_0 = 4E_{\mathrm{c}}(\epsilon_0(\delta) + B\cos\gamma) = 4E_{\mathrm{c}}\epsilon_0(\delta) - E_{\mathrm{J}}{}'\cos(\delta - 2\pi\frac{\Phi}{\Phi_0}), \tag{5.11}$$

and took its derivative with respect to the phase difference between the two lead electrodes. The current function is defined as

$$I = \left(\frac{2e}{\hbar}\right)\frac{\partial\varepsilon_0}{\partial\delta}. \tag{5.12}$$

We then numerically took the maximum of $I(\delta)$ with respect to $\delta$.

$$I_{\mathrm{s}}^{\max} = \max_{\delta}\{I(\delta)\}. \tag{5.13}$$

We calculated the ground state energy function $\varepsilon_0$ for two to five charge states with a magnetic flux as a parameter and using experimental numerical parameters. For the valley of the Coulomb oscillation, we set $n_{\mathrm{g}} = 0$ and used three or five charge states, $|\text{-}1\rangle$, $|0\rangle$, $|1\rangle$ or $|\text{-}2\rangle$, $|\text{-}1\rangle$, $|0\rangle$, $|1\rangle$, $|2\rangle$, respectively. For the peak of the Coulomb oscillation set $n_{\mathrm{g}} = 1/2$ and used two or four charge states, $|0\rangle$, $|1\rangle$ or $|\text{-}1\rangle$, $|0\rangle$, $|1\rangle$, $|2\rangle$, respectively.

Figure 5.11 shows the results of the critical current simulation with respect to $\Phi_{\mathrm{ext}}$ of the SCPT-embedded loop circuit. In the case of $n_{\mathrm{g}} = 0$ (SCPT off), we used three charge states with $-1 \leq n \leq 1$, $n$ is integer. In the case of $n_{\mathrm{g}} = 1$ (SCPT on), we did the simulation with both two and four charge states with $n = 0, 1$ and $-1 \leq n \leq 2$, respectively. We also did a simulation with five charge states with $-2 \leq n \leq 2$ for $n_{\mathrm{g}} = 0$. But it produced almost the same result with three charge state case. In the calculation, we used the $E_{\mathrm{J}}/E_{\mathrm{c}}$ ratio values in Table 5.1.

In the case of the gate at $n_{\mathrm{g}} = 1$, the red curve represents the results with two charge states, and the green curve with four charge states, respectively. In both cases of samples A and B, the amplitude of the oscillation decreased considerably with four charge states. The characteristics with four charge states should represent more realistic characteristics, and they resemble the observed results in Figs. 5.8 and 5.9. This difference between red and green curves originates from the amount of the included charge fluctuations in the island due to the Josephson coupling at the junction and resultant change in the ground state energy dispersions of the SCPT and, therefore, of the SCPT-embedded loop system.

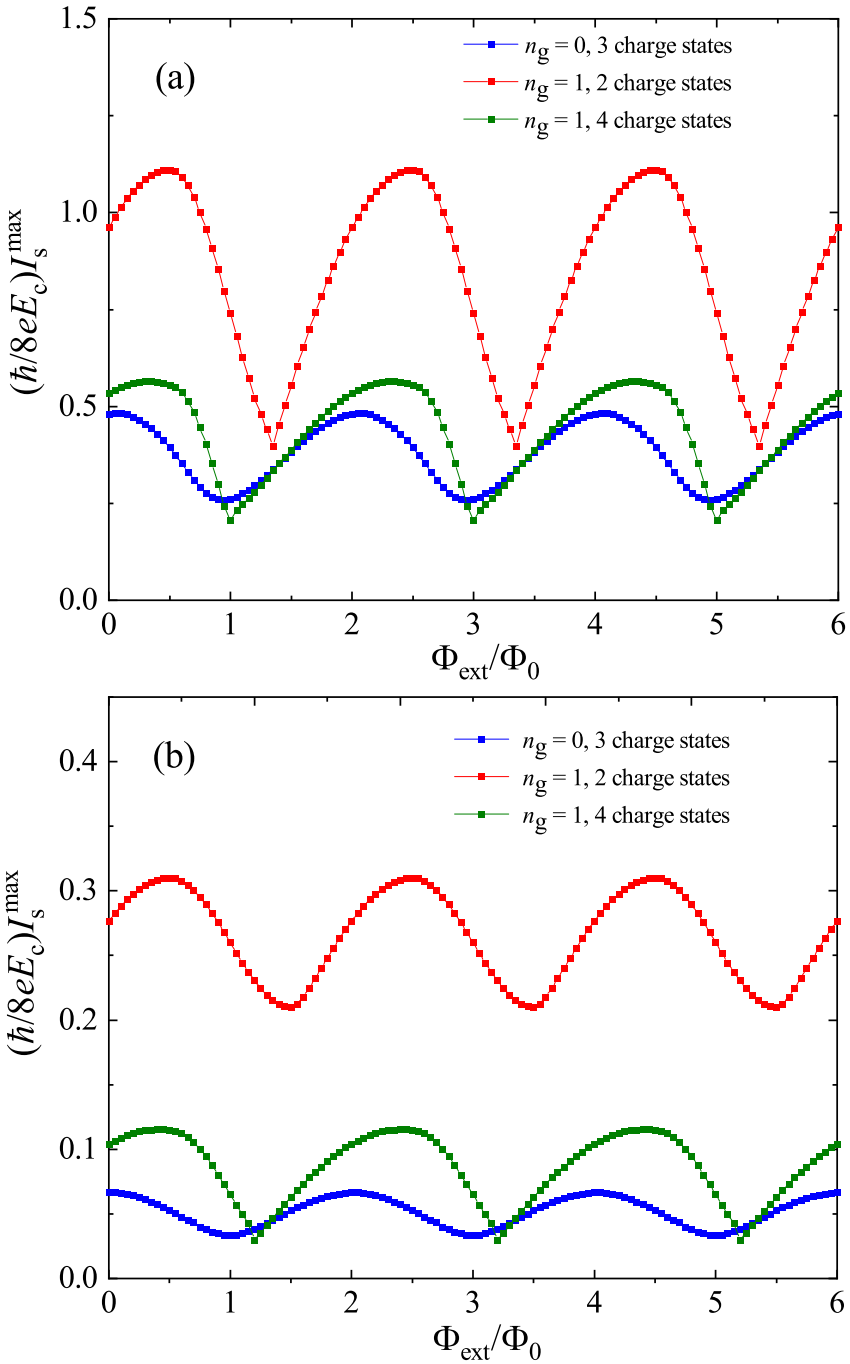


**Figure 5.11:** The maximum supercurrent of the SCPT-embedded loop circuits calculated with the parameters of sample A (a) and sample B (b).

## 5.6 Conclusion

In this chapter, we examined the properties of supercurrent through a SQUID-like loop where one of the branches had a single Josephson junction and the other branch had a SCPT. We observed a periodic modulation of the maximum supercurrent $I_s$ with respect to a magnetic flux through the loop with a period of $\Phi_0$. The supercurrent through the SCPT maintains the superconducting coherence when it modulated with the gate voltage. Thus, we confirmed a superconducting coherence through the SCPT.

We also examined the gate modulation of the $I_s - B$ characteristics. The characteristics didn't show a large change in $I_s$ due to the switching of the SCPT. This result was analyzed through a theoretical consideration including many charge states. The observed results are better understood considering the charge fluctuations due to involvement of many charge states in the SCPT.

These results indicate that a SCPT can be used as a supercurrent switch. However, when one designs a superconducting circuit including SCPTs, it is necessary to consider the charge fluctuations and the change in the characteristic due to it.

# Chapter 6

# Phonon detection using a single Cooper-pair transistor

## 6.1 Introduction

Recently, phononics in mesoscopic and nanometer scales attracts much interest [64–66]. A group in Cornell University used mesoscopic STJs to investigate transport processes of phonons through microstructures made of Si recently [32–35]. To detect phonons, STJs use an increase in the tunnel current caused by tunneling of nonequilibrium quasiparticles in the superconducting electrodes which are generated by dissociation of Cooper pairs absorbing phonons with the energy $\geq 2\Delta$. This detection of phonons by STJs is a traditional method invented in 1960s for macroscopic junctions. Eisenmenger and Dayem first demonstrated generation and detection of phonons by using a $Sn/SnO_2/Sn$ STJs on both faces of a sapphire single-crystal cylinder of a length of approximately 1 cm in 1967 [31]. The subsequent development is summarized in a review by Eisenmenger [28].

In recent years, the effect of nonequilibrium quasiparticles in single Cooper-pair devices and their dynamics were studied to clarify the quasiparticle poisoning effect and the mechanism of damping of the coherent oscillation in superconducting qubits [19, 21, 67, 68]. The elucidated behavior of nonequilibrium quasiparticles provides a path toward development of a sensitive phonon detector.

In this chapter, we show that the magnitude of the supercurrent flowing through

a SCPT is sensitive to the phonon flux with the energy $\geq 2\Delta$ towards the SCPT and can be used as a sensitive phonon detector. We propose a quantitative model of the SCPT detector, experimentally demonstrate its basic operation and show that its sensitivity is approximately $10^3$ times higher than that of the traditional STJ detector.

## 6.2 Proposed Principle of the detector

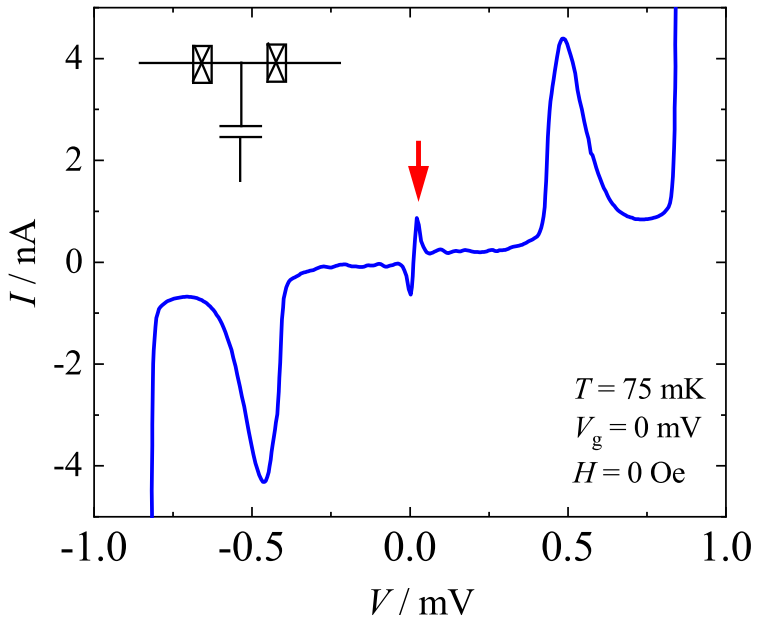


**Figure 6.1:** The current-voltage characteristics of a single Cooper-pair transistor and its schematic device structure. The red arrow indicates the supercurrent that is due to the Cooper-pair tunneling through the two junctions.

Figure 6.1 shows a current-voltage characteristics of a SCPT. The supercurrent peak $I$ (indicated with an arrow) increases or decreases in magnitude depending on the gate voltage $V_{\rm g}$, showing a $2e$ periodic Coulomb oscillation as a function of gate-induced charge number $N_{\rm g} = C_{\rm g}V_{\rm g}/e$ (Fig. 6.2 (b) solid line). The parity of the supercurrent can be state at the odd and even integer of the gate charge. It is well known that the behavior of the supercurrent through the SCPT is largely influenced by the existence of nonequilibrium quasiparticles in the electrodes[19, 21]. In Figure 6.2 (a), the behavior of the system energy as a function of $N_g$ is depicted

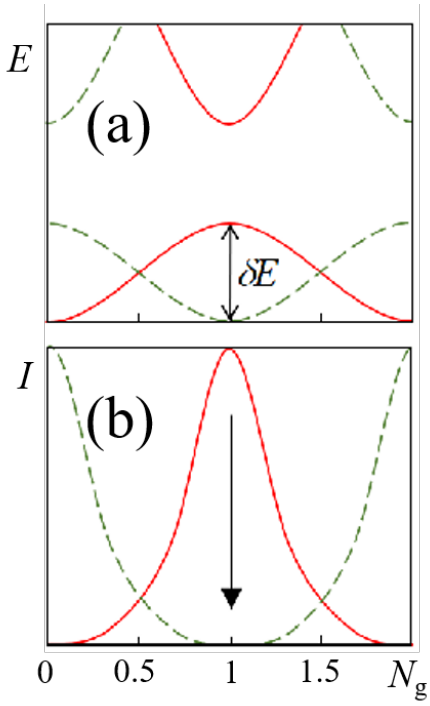


**Figure 6.2:** (a) Schematic diagram of the energy spectrum as a function of gate-induced charge number $N_g$ of a SCPT for even and odd parities. (b) corresponding supercurrent change as a function of $N_g$. When the parity keeps even, the current follows the solid (red) line showing a $2e$ periodicity. When quasiparticles are excited in the electrodes, the parity changes at $N_g = 0.5, 1.5$ and the current characteristic follows the lower branches showing $e$ periodicity.

for even parity (solid line) and odd parity (broken line). (See 2.2 for the parity effect.) When there is no quasiparticles in the island and the parity is even, the system follows the solid line with the change in $N_g$ with a periodicity of $2e$. The supercurrent $I$ shows a peak at $N_g = 2\nu+1$ with $\nu$ an integer. When a quasiparticle tunnels in the island and the parity becomes odd, the energy spectrum and the current characteristic shift by 1 in $N_g$ to the broken lines. As shown in Fig. 6.2 (a), the energy of the system with no quasiparticles in the island follows the solid line as a function of $N_g$ resulting in a $2e$ periodicity in $eN_g$. When a quasiparticle tunnels in the island and the parity of the number of particles becomes odd, the energy of the system follows the broken line. The current at $N_g = 1$ depends on whether a quasiparticle tunnels in the island (odd state, green broken line in Fig. 6.2) or not (even state, red solid line in Fig. 6.2).

When we measure a dc current $I$ with an integration time of the order of $10^{-2}$ s. The observed current is the sum of an averaged current of the current in the even

state $I_e$ and odd state $I_o$ with their probabilities in even state $P_e$ and odd state $P_o$ multiplied [19, 21, 67, 68]:

$$I = P_e I_e + P_o I_o, \tag{6.1}$$

with $P_e + P_o = 1$. The probability $P_e$ is expressed using the even-to-odd $\Gamma_{eo}$ and odd-to-even transition rates $\Gamma_{oe}$ of non-equilibrium quasiparticles, as[68]

$$P_e = \frac{\Gamma_{oe}}{\Gamma_{eo} + \Gamma_{oe}}. \tag{6.2}$$

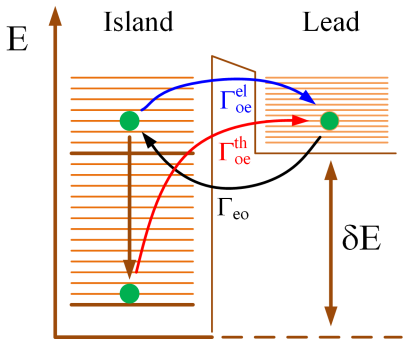


**Figure 6.3:** The even-to-odd and odd-to-even transition processes between the lead electrode and island.

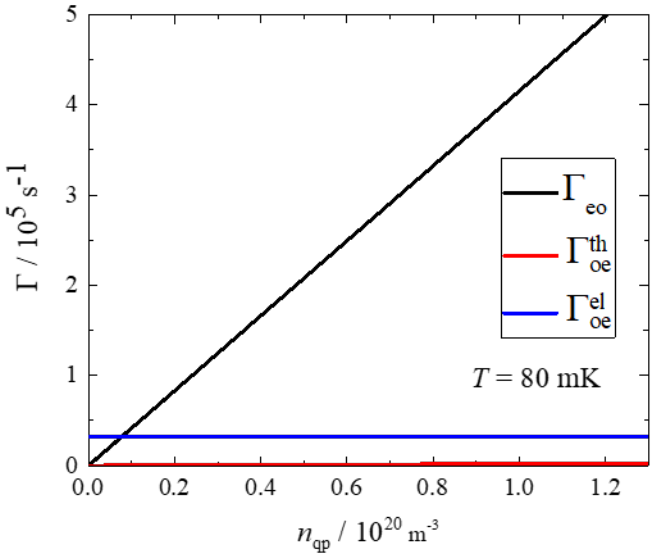


**Figure 6.4:** Transition probabilities for the parity effect (courtesy of H. Shimada), with parameters, $E_c = 57$ $\mu$eV, $E_J = 40$ $\mu$eV, $\Delta = 150$ $\mu$eV, the volume of the island electrode $1.0 \times 10^{-18}$ m$^3$, the density of states at $\epsilon_F$ of Al $1.45 \times 10^{47}$ m$^3$J$^{-1}$.

Shaw et al. calculated the transition rates, gave their expressions and showed that the odd-to-even tunneling probabilities are dominated by unequilibrated quasiparticles, i. e. the process labeled as $\Gamma_{\rm oe}^{\rm el}$ in Fig. 6.3, (cf. the process labeled as $\Gamma_{\rm oe}^{\rm th}$ is by equilibrated quasiparticles), and are approximately independent of the non-equilibrium quasiparticle density $n_{\rm qp}$, the $\Gamma_{\rm eo}$ is approximately proportion to $n_{\rm qp}$ [68],

$$\Gamma_{\rm eo} \simeq K n_{\rm qp} \tag{6.3}$$

$$K = \frac{G_N e^{\Delta/kT}}{e^2 N} \int_{\Delta}^{\infty} dE \frac{E(E+\delta E) - \Delta^2}{\sqrt{[(E+\delta E)^2 - \Delta^2](E^2 - \Delta^2)}} e^{-E/kT}, \tag{6.4}$$

where $N = D(\epsilon_{\rm F})\sqrt{2\pi\Delta kT}$ with $D(\epsilon_{\rm F})$ being the normal-state density of states at the Fermi energy of the electrodes. $G_N$ is the normal-state tunneling conductance and $\delta E$ is the energy difference between even and odd states. An example of $n_{\rm qp}$ dependences of $\Gamma$'s are shown in Fig. 6.4. $\Gamma_{\rm oe}$, can be considered as a constant in the parameter range of our interest[68]. Thus,

$$I = I_{\rm o} + \frac{\Delta I}{1 + (K/\Gamma_{\rm oe}) n_{\rm qp}} \tag{6.5}$$

$$\Delta I = I_{\rm e} - I_{\rm o} \tag{6.6}$$

This result means that, with the increase in $n_{\rm qp}$ starting from zero to $n_{\rm qp} \gg \Gamma_{\rm oe}/K$, the observed current changes from $I = I_{\rm e}$ to $I = I_{\rm o}$ as shown in Fig. 6.2(b) with an arrow.

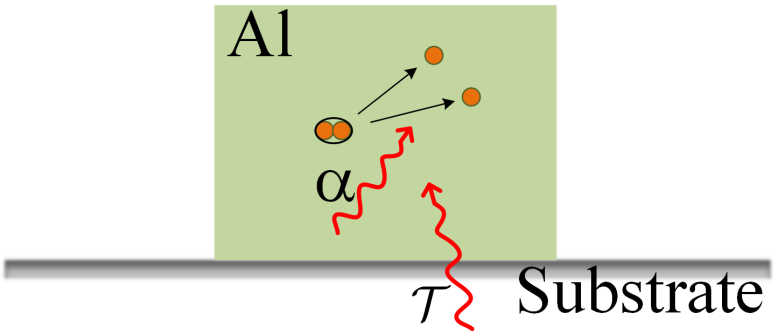


**Figure 6.5:** Schematic of nonequilibrium-quasiparticle generation in the detector Al electrode. The phonons transiting from the substrate into the Al electrode are absorbed in the dissociation process of Cooper pairs into the quasiparticles.

With a phonon flux of $\dot{n}_{\rm ph}$, the nonequilibrium quasiparticles are generated with the rate

$$\dot{n}_{\rm qp,ph} = \mathcal{T}\alpha 2\dot{n}_{\rm ph}, \tag{6.7}$$

in the electrodes of SCPT, including the leads and the island. $\mathcal{T}$ is the acoustic transmission factor for phonons transiting from the substrate into Al, $\alpha$ is the fraction of phonons absorbed in the SCPT electrodes [33]. Here, we assume that there is a characteristic decay time constant, $\tau$, of the nonequilibrium quasiparticle density $n_{\rm qp}$. It will partially represent the escape time of the quasiparticle from the active range of the detector and partially the recombination lifetime. (See the later sections for the detail.) In the steady state condition,

$$\dot{n}_{\rm qp,ph} = \frac{n_{\rm qp}}{\tau}. \tag{6.8}$$

Thus, by combining this relation with eq. 6.5, we obtain a relation to detect the phonon flux with the SCPT supercurrent:

$$I = I_{\rm o} + \frac{\Delta I}{1 + \gamma\dot{n}_{\rm ph}} \tag{6.9}$$

where $\gamma = 2\tau\alpha TK/\Gamma_{\rm oe}$. For small $\dot{n}_{\rm ph}$, by expanding right-hand side of eq. (6.9) with respect to $\gamma\dot{n}_{\rm ph}$, we obtain the following small signal response:

$$\delta I \simeq -\Delta I\gamma\dot{n}_{\rm ph}. \tag{6.10}$$

In this way, the phonon flux is detected by the change in the supercurrent through the SCPT.

To summarize the process, when a flux of phonons with the energy $\geq 2\Delta$ propagates toward the SCPT, the incident phonons break Cooper pairs in the superconducting electrodes of the SCPT and generate quasiparticles. The excited quasiparticles diffuse to the junction. One of them may tunnel in the island and change the parity of the SCPT from even to odd. This makes the supercurrent of SCPT go down from $I_{\mathrm{e}}$ to $I_{\mathrm{o}}$ at $N_{\mathrm{g}} = 1$. The state of the SCPT may go back to even state. But, with the increase in the number of quasiparticles, the probability of the odd state increases and the observed time averaged current decreases.

## 6.3 Experimental methods

In order to examine the above proposed detector operation of the SCPT, we performed an emission-detection measurement of phonons using a SCPT as a detector and a dc-SQUID as a phonon emitter.

The sample consists of a SCPT and a small-area dc SQUID both made of mesoscopic Al/$AlO_x$/Al junctions. The length of the dc-SQUID from the SCPT $d$ were 2, 10, and 20 $\mu$m. The size of junctions for the SCPT were approximately 0.02 $\mu m^2$ and the island's dimensions were 200 nm wide $\times$ 1 $\mu$m long. The size of junctions for the dc SQUID were approximately 0.01 $\mu m^2$ with the dc SQUID loop area was 0.6 $\mu$m $\times$ 3.6 $\mu$m. The samples were fabricated on an oxidized Si surface by using standard electron-beam lithography (EBL) and the electron-beam evaporation Al described in 3.2.

In the measurement, the SCPT and the dc SQUID were connected to two independent measurement circuits as shown in Fig. 6.7. The measurement was performed using a compact dilution refrigerator described in 3.3. To use the SQUID as a phonon emitter as described in detail in the next section, we applied a magnetic flux $\Phi_0/2$ through the loop of the SQUID using a superconducting solenoid, where $\Phi_0$ indicates the flux quantum. With this magnetic flux, the effective Josephson coupling energy $E_J^*$ becomes zero, and we can suppress the Josephson effect between the two electrodes of the SQUID.

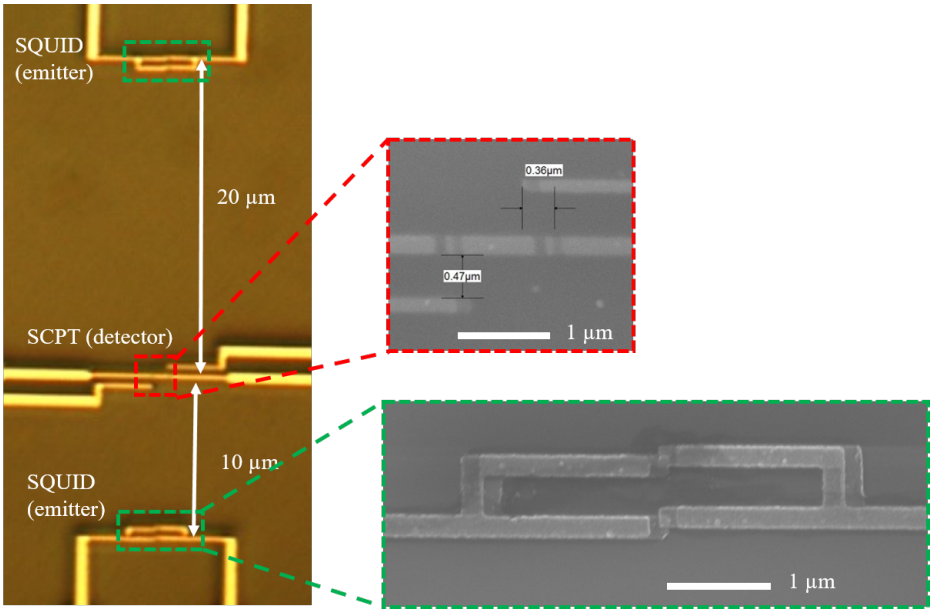


**Figure 6.6:** Microscope image of the device with $d = 10$ $\mu$m and 20 $\mu$m and scanning electron microscopy (SEM) image of the SQUID and the SCPT.

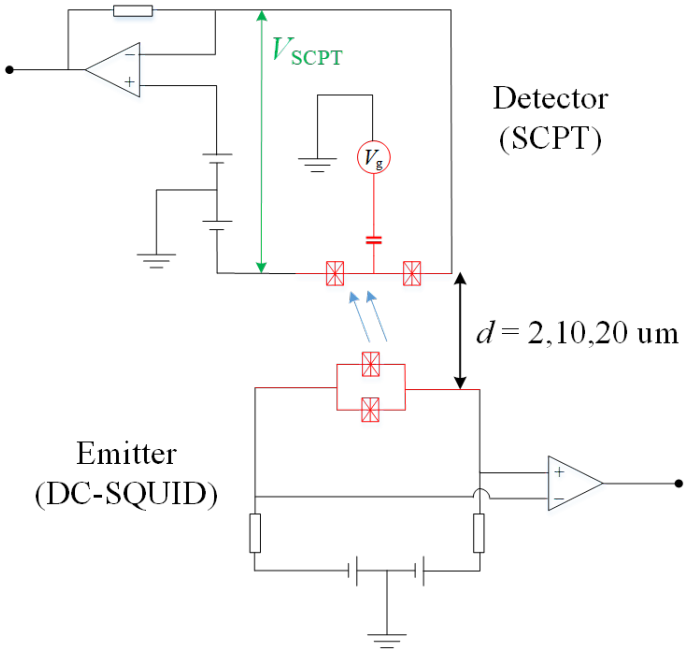


**Figure 6.7:** Schematic configuration of the measurement. The emitter is a dc SQUID with a half flux quantum, $\Phi_0/2$, through the loop. The distance between the emitters and the detector are 2, 10 and 20 $\mu$m. The detector is a SCPT.

## 6.4 Experimental Results

### 6.4.1 Parameters and basic characteristics of the devices

Table 6.1: Parameters of the samples: distance from the SCPT $d$, tunnel resistance $R_{\mathrm{T}}$ of the junction, Josephson coupling energy $E_{\mathrm{J}}$ of the junction, charging energy $E_{\mathrm{c}}$, the $E_{\mathrm{J}}$ to $E_{\mathrm{c}}$ ratio, junction capacitance $C$ and gate capacitance $C_g$.

| Sample | Device | $d$ | $R_{\mathrm{T}}$ kΩ | $C$ fF | $E_{\mathrm{J}}$ $\mu$eV | $E_{\mathrm{c}}$ $\mu$eV | $E_{\mathrm{J}}/E_{\mathrm{c}}$ | $C_g$ aF |
|---|---|---|---|---|---|---|---|---|
| 1 | SCPT | - | 15.3 | 0.50 | 79 | 16 | 0.20 | 13 |
| | SQUID | 2 | 15.5 | 0.50 | 42 | 160 | 0.26 | - |
| 2 | SQUID1 | 10 | 13.0 | 0.70 | 49 | 114 | 0.43 | - |
| | SCPT | - | 12.2 | 0.70 | 40 | 57 | 0.71 | 12 |
| 3 | SQUID2 | 20 | 11.3 | 0.90 | 57 | 89 | 0.64 | - |

The important parameters of all devices are shown in Table 6.1. For the single SCPT, the tunnel resistance $R_{\mathrm{T}}$ and the capacitance $C$ of the junction were obtained from the slope in the asymptotic $I-V$ curve of SCPT at high bias and the offset voltage assuming identical two junctions in the SCPT. The Josephson coupling energy was calculated using the Ambegaokar-Baratoff formula [10] with the superconducting gap $\Delta \simeq 150$–$170$ $\mu$eV of our Al film, which was obtained using the differential conductance characteristics of the SCPT considering the offset voltage because of the charging effect. The gate capacitance, $C_g$, was obtained from the Coulomb oscillation (described below). The charging energy $E_{\mathrm{c}}$ was calculated using the relation $E_{\mathrm{c}} = e^2/2C_\Sigma$ with $C_\Sigma = 2C + C_g$. For the SQUID, the tunnel resistance $R_{\mathrm{T}}$ was obtained from the slope in the asymptotic $I-V$ curve of the SQUID at high bias. The property of junctions in the SQUID were assumed to be the same in each branch.

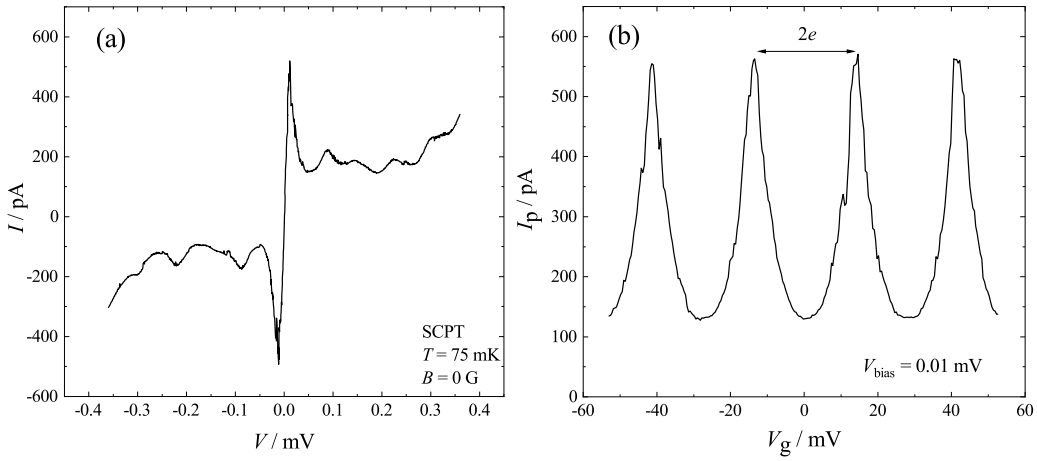


**Figure 6.8:** (a) The $I - V$ characteristics of the SCPT in sample 1 shows the supercurrent peak and (b) the Coulomb oscillation curve of the supercurrent of the SCPT.

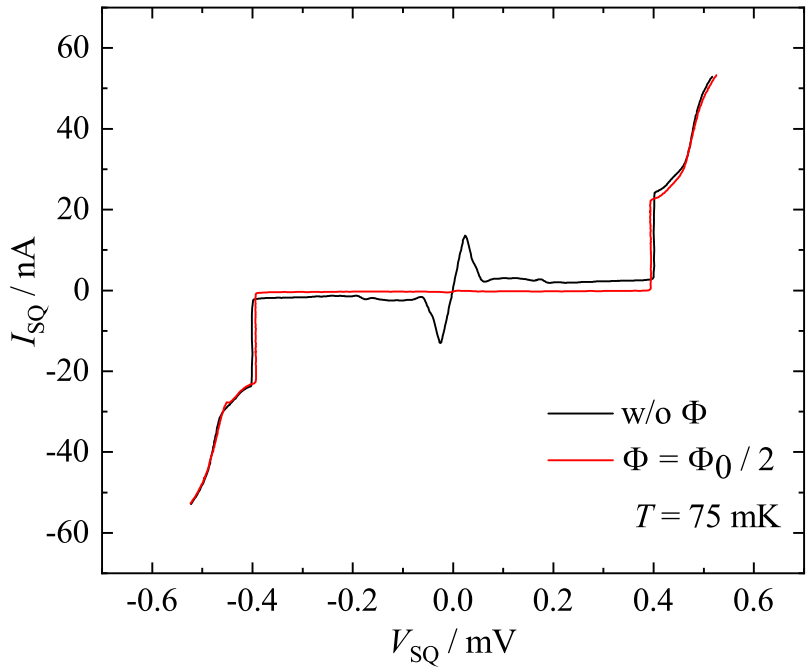


**Figure 6.9:** The current-voltage characteristics of the SQUID in sample 1 with and without application of the magnetic flux of $\Phi_0/2$.

In Fig. 6.8(a), the basic $I - V$ characteristics of the detector SCPT is shown. The Coulomb oscillation of the supercurrent at the voltage bias $V = 0.01$ mV is shown in Fig. 6.8(b). Figure 6.9 shows the $I_{\rm SQ} - V_{\rm SQ}$ characteristics of the SQUID with and without application of the magnetic flux of $\Phi_0/2$. The suppression of the supercurrent is clearly seen with a magnetic flux of $\Phi_0/2$. When the $\Phi_0/2$ is applied the principal transport process is the quasiparticle tunneling at $V_{\rm SQ} \geq 2\Delta/e \equiv V_{\rm th} = 0.39\,{\rm mV}$. When a quasiparticle tunneling occurs, quasiparticles are excited in the electrodes on both sides of the junction. The successive quasiparticle tunnelings generate a steady-state population of quasiparticles in the electrodes, then they relax in energy emitting so-called relaxation phonons and recombine to Cooper-pairs emitting so called recombination phonons. Thus, the SQUID with a $\Phi_0/2$ magnetic flux becomes a source of phonons with the energy of $2\Delta$ or greater without emission of electromagnetic waves caused by the ac Josephson effect. It is well known since 1960s that mostly phonons but photons are emitted when the quasiparticles recombine [29, 30].

### 6.4.2 Change in the Coulomb oscillation due to the quasiparticle tunneling in the emitter

Figure 6.10 shows how the Coulomb oscillation curve evolves with the bias point of the SQUID in sample 1 with $d = 2\,\mu$m. The black dots in Figure 6.10(a) show the bias points on the SQUID for the emission-detection measurement. In Fig. 6.10(b), at the lowest bias voltages on the SQUID, the observed Coulomb oscillation showed $2e$ periodicity. The shape of the oscillation curve changed rapidly when the bias voltage was increased, $V_{\rm SQ} \geq 0.39$ mV ($V_{\rm th}$), where the quasiparticle tunneling starts and the current increases rapidly in the SQUID. At $0.43\ {\rm nA} < I_{\rm SQ} < 0.85$ nA, the peak current decreases rapidly. At the bias current $I_{\rm SQ} > 6$ nA, the oscillation period changes to the $e$ period. It is well known that, as far as $V_{\rm th} \leq V_{\rm SQ} \leq 4\Delta/e$, only recombination phonons contribute to the generation of quasiparticles in the detector electrode [28].

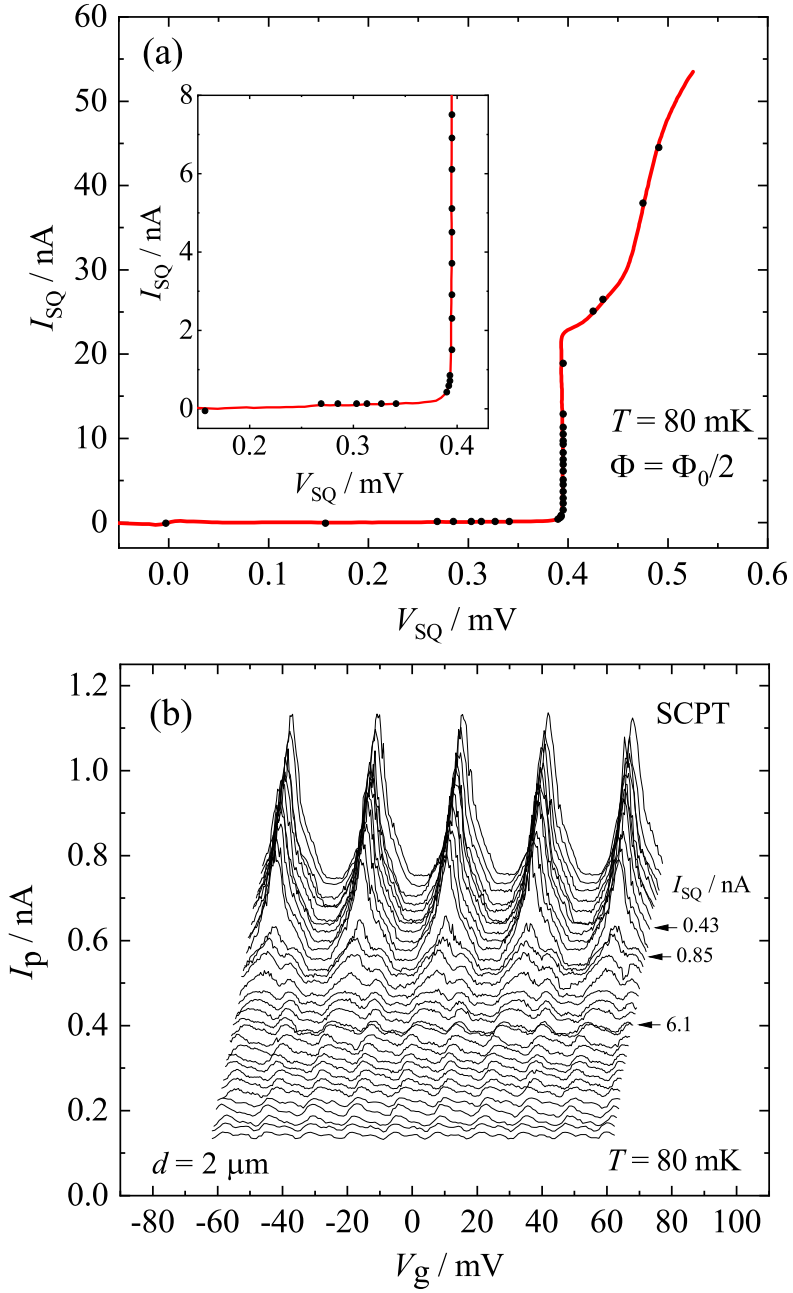


**Figure 6.10:** (a) $I - V$ curve of the SQUID with a half flux quantum in sample 1 at 80 mK. Inset: magnified figure of the threshold range. The black dots show the bias points for the emission-detection measurement. (b) Observed changes in the Coulomb oscillation of the supercurrent of the SCPT. The oscillation period changes from $2e$ in $C_g V_g$ to $e$ as the bias increases in the SQUID. The plot of observed Coulomb oscillation curves corresponding to the bias point of the SQUID had 32 curves. Each curve is shifted by +0.5 mV along the $V_g$-axis and is shifted by +0.02 nA along the $I_p$-axis successively. The bottom curve corresponds to the actual $V_g$ and $I_p$ values.

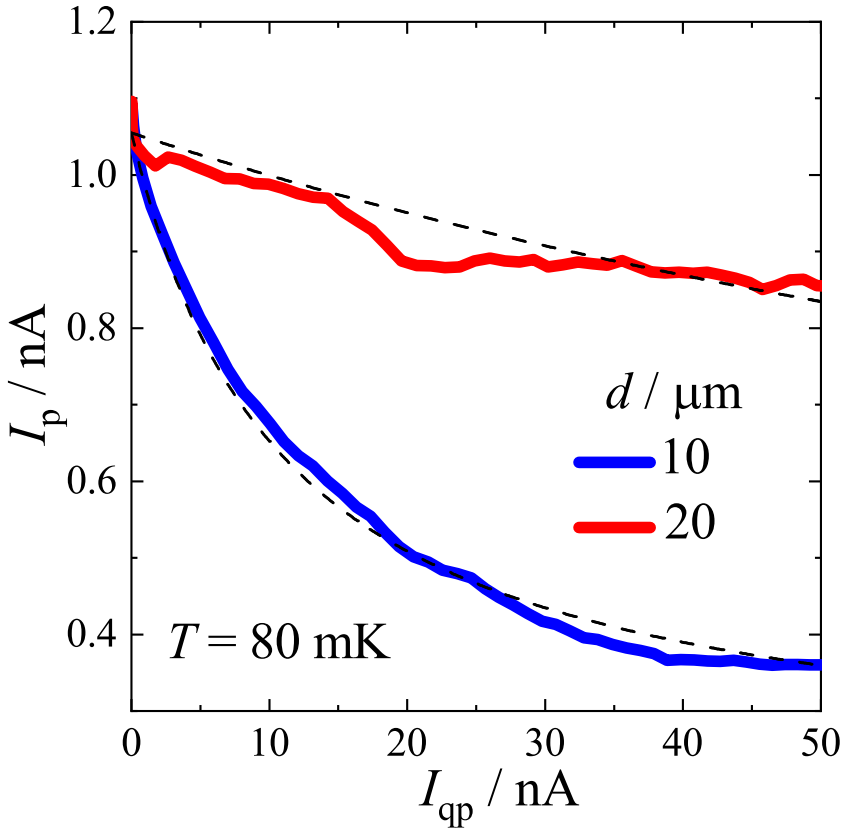


**Figure 6.11:** The SCPT supercurrent-peak change with the quasiparticle current in the SQUID emitter ($d = 10$ and 20 $\mu$m) in samples 2 and 3. The broken lines are theoretical fits. Fitting parameters : $I_o = 0.205$ nA, $\Delta I = 0.85$ nA, $\kappa = 0.9 \times 10^8$ s and $0.7 \times 10^7$ s for $d$ is 10 and 20, respectively.

### 6.4.3 Dependence of the detector current on the emitter current

We then fixed the gate voltage to one of the Coulomb oscillation peaks, monitored its current magnitude $I_{\rm p}$, and scanned the bias current in the SQUID, $I_{\rm SQ}$. The results on samples 2 and 3, where the detector SCPT was common one and two SQUIDs are on its both sides, are plotted in Fig. 6.11. In this plot, we took the quasiparticle-tunneling current $I_{\rm qp} \equiv I_{\rm SQ}(V_{\rm SQ}) - I_{\rm SQ}(0.75V_{\rm th})$ for the horizontal axis instead of $I_{\rm SQ}$. As can be clearly seen, $I_{\rm p}$ decreases monotonically with the increase in $I_{\rm qp}$ for both samples. The slope for $d = 20\,\mu$m is much smaller than for $d = 10\,\mu$m.

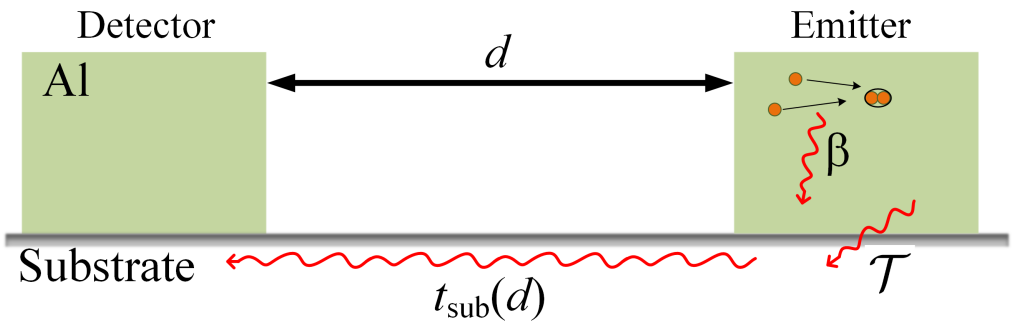


**Figure 6.12:** Schematic of the transmission of phonons generated at the emitter towards the detector range with relevant transmission factors.

Now we apply the theoretical consideration above to the results in Fig. 6.11. With a quasiparticle current $I_{qp}$ in the emitter, quasiparticles are generated on both sides of the junction at a rate of $2I_{qp}/e$, then recombination phonons are generated with a rate $\beta I_{qp}/e$ where $\beta$ accounts for the escape of quasiparticles out of the relevant area. The generated phonons are transmitted to the substrate with a rate $\mathcal{T}$, then transmitted to the detector range with a transmission factor of $t_{sub}(d)$. Thus, $\dot{n}_{ph} = t_{sub}(d)\mathcal{T}\beta I_{qp}/e$ [32]. Combining this with eq. (6.9), we obtain

$$I_p = I_o + \frac{\Delta I}{1 + \kappa I_{qp}} \tag{6.11}$$

with $\kappa = \gamma t_{sub}(d)\mathcal{T}\beta/e$. The broken lines in Fig. 6.11 are fits of eq. (6.11) to the experimental results for the two cases with the fitting parameters of $I_0 = 0.205\,\mathrm{nA}$, $\Delta I = 0.85\,\mathrm{nA}$ and $\kappa = 0.9 \times 10^8$ s for $d = 10\,\mu\mathrm{m}$ and $0.7 \times 10^7$ s for $d = 20\,\mu\mathrm{m}$. The fitting is fairly good demonstrating the validity of the analyzed device operation. The difference in $\kappa$ between $d = 10\,\mu\mathrm{m}$ and $20\,\mu\mathrm{m}$ is reasonable because phonons transmitted through the used substrate should decay with the distance $d$ between SCPT and SQUID.

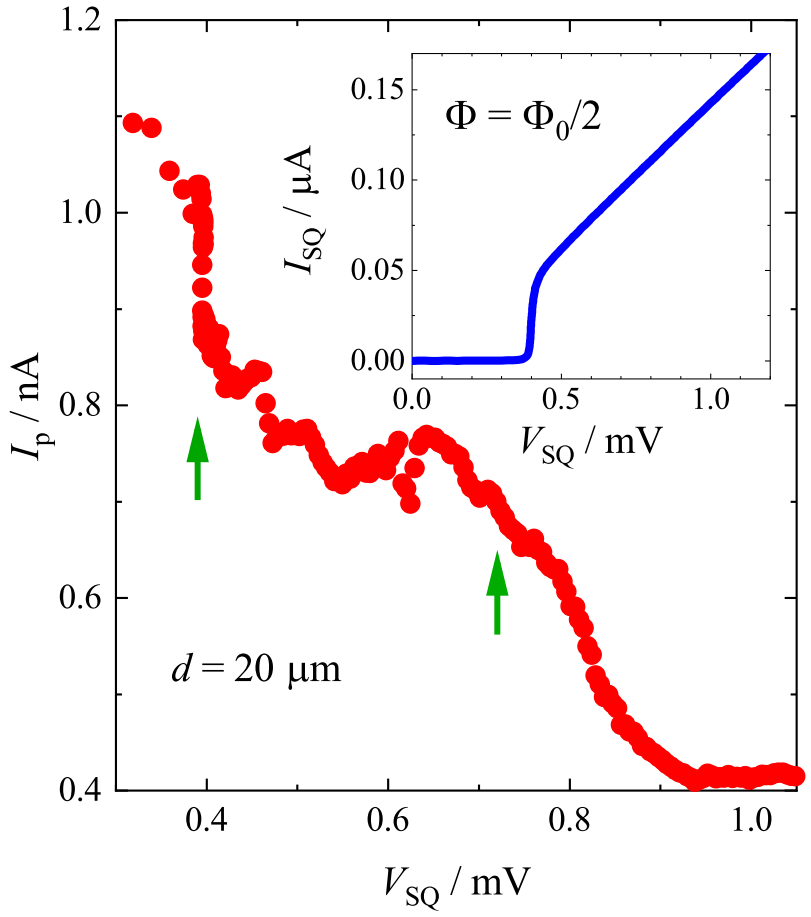


**Figure 6.13:** The SCPT supercurrent-peak change with the voltage in the SQUID emitter ($d = 20$ $\mu$m, sample 3). Inset: $I - V$ characteristic of the SQUID emitter.

### 6.4.4 The structures observed in the $I_p - V_{SQ}$ characteristic

Figure 6.13 shows the change in $I_p$ for $d = 20\,\mu$m in sample 2 as a function of bias voltage $V_{SQ}$ across the SQUID with a half flux $\Phi_0/2$. Clear structures are seen in the $I_p - V_{SQ}$ characteristic. By increasing $V_{SQ}$, one can see a sharp drop of $I_p$ at $\sim 0.40$ mV. Further increasing $V_{SQ}$, $I_p$ shows a monotonic decrease up to $V_{SQ} \sim 0.7$ mV, above which $I_p$ shows a sharp drop again. The former voltage corresponds to the threshold for the quasiparticle tunneling, i.e. $V_{th1} = 2\Delta + E_c$ while the latter should to $V_{th2} = 4\Delta + E_c$. $V_{th2}$ corresponds to the onset of emission of relaxation phonons with $\hbar\omega \geq 2\Delta$ [28] (See also Fig. 2.14(b)).

## 6.5 Discussions

### 6.5.1 Exclusion of thermal effect

The supercurrent $I_p$ can be decreased with the increase in the temperature of the device [69]. However, we can exclude such thermal effect in the results in 6.4. As shown in the inset in Fig. 6.13, at $V_{SQ} \simeq 0.4$ mV, the current in the SQUID starts flowing because of the quasiparticle tunneling. Above $V_{SQ} > 0.4$ mV, the current monotonically increases with the increase in $V_{SQ}$ and, thus, the dissipated power also monotonically increases. If the phonons emitted associated with the quasiparticle tunneling thermalize before reaching the detector, the temperature will also monotonically increases with the increase in $V_{SQ}$. However, we observe a clear structure in the response in the detector as a function of $V_{SQ}$, which accords with the specification of the emitted phonon energies in 6.4.4. This indicates that the nonequilibrium distribution of phonons generated at the emitter is preserved during their transmission to the detector, and that the observed decrease in $I_p$ of the detector is not a thermal effect.

### 6.5.2 Temperature range of the detector operation

The experimental results together with the theoretical consideration described above suggest that the supercurrent branch of the SCPT can be used for phonon detection. Since the device works on the basis of the single charge tunneling, its operation temperature should be $T \ll E_c/k_B$. At non-zero temperature, the thermal quasiparticles in the electrodes make the device work in the same way as the nonequilibrium quasiparticles. With a thermal density of quasiparticles, $n_{qp}^{(th)}$, the dynamic range $\Delta I$ becomes smaller to $\Delta I' = \Delta I/(1 + (K/\Gamma_{oe})n_{qp}^{(th))}$. Thus, $T < T^*$ is required, where $T^*$ is the temperature introduced in Ref. [69], which shows the temperature where the thermal average number of quasiparticles on the island becomes of order 1. At $T = T^*$, the periodicity of the Coulomb oscillation of the supercurrent change to $e$ in a SCPT and $\Delta I \simeq 0$.

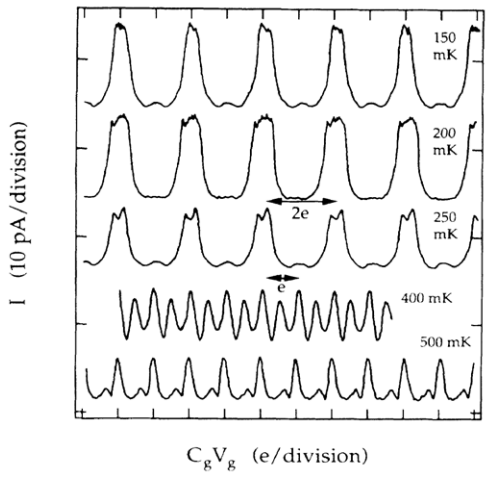


**Figure 6.14:** $I - Q_0$ curves at supercurrent peak for various $T$. The characteristic at near 300 mK does not show the 2e periodicity [69].

### 6.5.3 Sensitivity of the detection

From the result in Fig. 6.11, the sensitivity $\Delta I_p/\Delta I_{qp}$ is approximately 0.03 for $d = 10\,\mu$m and $I_p \simeq 5\,$nA. We compare this sensitivity with that of a traditional STJ detector.

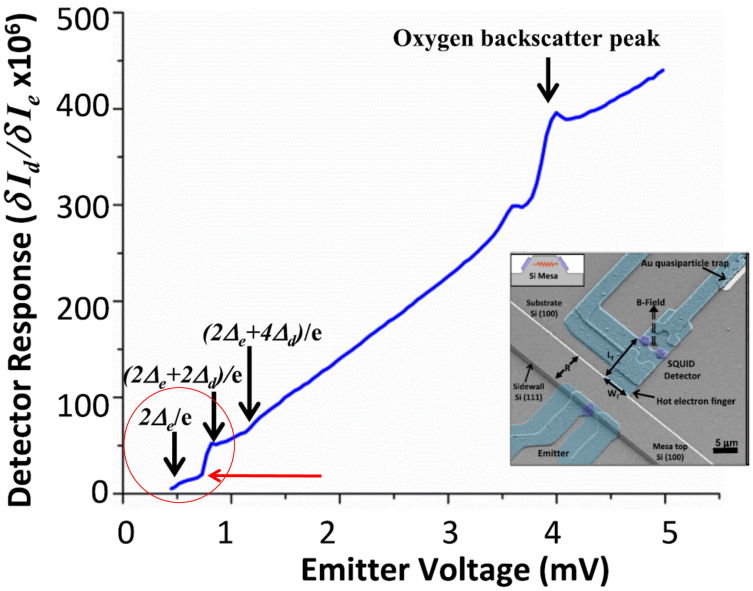


**Figure 6.15:** Differential transfer function $\delta I_\mathrm{d}/\delta I_\mathrm{e}$ of the Cornell University group measure with an ac modulation method [33]. Inset: False-colored SEM micrograph of phonon spectrometer.

Figure 6.15 shows the result on the measurement of differential transfer function $\delta I_\mathrm{d}/\delta I_\mathrm{e}$ of a traditional Al/AlO$_\mathrm{x}$/Al STJ phonon detector as a function of emitter dc bias voltage by the Cornell university group. In their measurement, also an Al/AlO$_\mathrm{x}$/Al STJ was used as the phonon emitter with the emitter-detector distance $d = 10$ $\mu$m. (See also 2.3.3 about STJ.) They used an ac modulation method to measure the detector response $\delta I_\mathrm{d}/\delta I_\mathrm{e}$. At the dc emitter voltage $V_\mathrm{em} = 2\Delta_e$ ($\Delta_e$ being the superconducting gap of the emitter electrode), the quasiparticles start tunneling in the emitter and recombination phonons are emitted, and at the emitter voltage above $V_\mathrm{em} = (2\Delta_e + 2\Delta_d)/e$, also relaxation phonons with the energy $\geq 2\Delta_e$ as well as the recombination phonons are emitted. Thus, the number of phonons generated with a unit current increases in the latter voltages. Our result in Fig. 6.11 corresponds to the case where only recombination phonons are involved. Thus, the sensitivity to compare is the one indicated with the arrow in Fig. 6.15. It is approximately $1 \times 10^{-5}$ [33]. Thus, the present detector has much higher sensitivity, in this sense, by a factor more than $10^3$ nominally than the traditional one.

The Cornell University group placed the emitter and the detector on oblique (111) surfaces on both sides of Si microfabricated mesa, so that phonons can propagate by line of sight from the emitter to the detector. Also the phonon focusing

effect[70] contributes to enhance the transmission factor in their case [32]. In our case, on the other hand, the devices are fabricated on a (100) surface of the $Si/SiO_2$ substrate, the direction of direct propagation of phonons is in <011> direction, and the phonon focusing effect is absent. Also our devices are arranged laterally and out of the line of sight. Thus, we expect the phonon flux reachable to the detector per the same emitter current in our case is much smaller than those in the case of the Cornell University group. The compared sensitivities, thus, include the difference in the phonon propagation factor, $t_{\rm sub}$, which is expected to be smaller in our case. Thus, the sensitivity ratio of the SCPT detector in comparison of the STJ detector can be still higher than $10^3$.

### 6.5.4 Effective range of the devices

In the samples, the SCPT detector and the SQUID emitter themselves have a size approximately 1 $\mu$m, and the connecting Al leads have length of roughly 100 $\mu$m. Thus, we discuss the effectively active range of the devices here. The effective range depends on the active range of the nonequilibrium quasiparticles in the devices. The quasiparticles, once generated in the device, may diffuse in the Al electrode until they recombine to form Cooper pairs or reach the normal metallic contact pads, which serve as quasiparticle traps [71]. The diffusion constant, $D$, of quasiparticle at temperature $T$ is calculated using a diffusion constant $D_{\rm n}$ of electrons in the normal metallic state of the electrode [72]:

$$D = \sqrt{\frac{2k_{\rm B}T}{\pi\Delta}} D_{\rm n}. \tag{6.12}$$

Using available values of $D_{\rm n}$ for Al 60 cm$^2$/s [72] and $\Delta = 160$ $\mu$eV for our Al electrode, we obtain $D = 10$ cm$^2$/s at $T = 80$ mK.

When quasiparticle tunnelings occur at the SQUID junctions, the quasiparticles are generated on both sides of the junctions, and relaxation and recombination occur in the superconducting leads as depicted in Fig. 2.12. The relaxation time, $\tau_{\rm rel}$, is comparatively short and 1 ns [32], and the diffusion length before the relaxation is estimated to be $\sqrt{D\tau_{\rm rel}}$ $\sim$1 $\mu$m. Thus, relaxation phonons are generated around the SQUID junction. Because $k_{\rm B}T \ll \Delta$, thermal quasiparticles are expected to

be absent, and the recombination of nonequilibrium quasiparticles occurs via the self-recombination process [20, 73]. The recombination time, $\tau_{\rm rec}$, is derived from a pulsed quasiparticle- injection measurement in Ref. [20] to be $\sim$100 $\mu$s at 100 mK. Thus, diffusion length before the recombination is estimated to be $\sqrt{D\tau_{\rm rec}}$ $\sim$300 $\mu$m, which covers the whole range of the device and lead structure.

Here we concentrate on samples 2 and 3 to discuss the specific cases. The emitter SQUIDs have successively wider leads from the junctions to the bonding pads as partly shown in Fig. 6.6. They are also designed to be successively farther from the SCPT detector. In a steady state, the wider part is expected to have lower quasiparticle density $n_{\rm qp}$, and lower phonon-emission probability. Therefore, the thinnest leads adjacent to the junctions is most efficient to generate recombination phonons. Thus, as the zeroth approximation, we may consider that part to be the active range of the phonon emitter.

In the case of SCPT detector, nonequilibrium quasiparticles generated at a far part of the lead should have a finite probability to reach the SCPT junction and tunnel in the island electrode before recombination because the diffusion length is sufficiently long. However, also in this case, the lead has a successively wider width to the pads. This conversely gives a diffusion impedance from far side towards the junction [72]. Thus, in this case again, as the zeroth approximation, we may consider that the thinnest leads adjacent to the SCPT junctions is the active range of phonon detection.

### 6.5.5 Quasiparticle decay time

In this subsection, we reconsider the relation between quasiparticle density $n_{\rm qp}$ and the phonon flux due to the emitter in the active region of the electrode more in detail. The dynamics of the quasiparticle and phonon system in a superconducting electrode is expressed in terms Rothwarf and Taylor formula [74]. For the phonon density $n_{\rm ph}$, we consider only phonons with energy $\hbar\omega > 2\Delta$. We include an escape term of quasiparticles from the relevant active region represented with an escape time $\tau_{\rm esc}$ and also an external phonon flux per volume of the Al electrode $F_0$ in the

original formula:

$$\frac{\mathrm{d}n_{\mathrm{qp}}}{\mathrm{d}t} = \zeta n_{\mathrm{ph}} - \frac{n_{\mathrm{qp}}}{\tau_{\mathrm{esc}}} - R n_{\mathrm{qp}}^2, \tag{6.13}$$

$$\frac{\mathrm{d}n_{\mathrm{ph}}}{\mathrm{d}t} = F_0 + \frac{R n_{\mathrm{qp}}^2}{2} - \frac{\zeta n_{\mathrm{ph}}}{2} - \frac{n_{\mathrm{ph}}}{\tau_\gamma}. \tag{6.14}$$

Here, $\zeta$ is the transition probability for the breaking of Cooper pairs by phonons, $R$ is the recombination coefficient of quasiparticles, and $\tau_\gamma^{-1}$ is the transition probability of phonons out of the energy range $\hbar\omega > 2\Delta$ or out of the active region of the electrode. As we argued in the previous discussion, the active range can be assumed to be the thinnest electrodes near the junction, which has the length of the order of 10 $\mu$m, and the escape time is estimated using the diffusion constant to be 0.1 $\mu$s, which is by orders smaller than the recombination time ($\sim$100 $\mu$s). Thus, in the above equations, we omit the recombination term and use the following linearized equations:

$$\frac{\mathrm{d}n_{\mathrm{qp}}}{\mathrm{d}t} = \zeta n_{\mathrm{ph}} - \frac{n_{\mathrm{qp}}}{\tau_{\mathrm{esc}}}, \tag{6.15}$$

$$\frac{\mathrm{d}n_{\mathrm{ph}}}{\mathrm{d}t} = F_0 - \frac{\zeta n_{\mathrm{ph}}}{2} - \frac{n_{\mathrm{ph}}}{\tau_\gamma}. \tag{6.16}$$

In the steady state, we obtain by equating the left-hand sides to be 0,

$$n_{\mathrm{qp}} = \tau_{\mathrm{esc}} \zeta n_{\mathrm{ph}}, \tag{6.17}$$

$$\left(\frac{\zeta}{2} + \frac{1}{\tau_\gamma}\right) n_{\mathrm{ph}} = F_0. \tag{6.18}$$

These give

$$n_{\mathrm{qp}} = \tau_{\mathrm{esc}} \zeta \left(\frac{\zeta}{2} + \frac{1}{\tau_\gamma}\right)^{-1} F_0 = 2\tau_{\mathrm{esc}} \left(1 + \frac{2}{\zeta\tau_\gamma}\right)^{-1} F_0. \tag{6.19}$$

Thus, $\tau$ in eq. (6.8) corresponds to the escape time $\tau_{\mathrm{esc}}$, and $\alpha$ in eq. (6.7) corresponds to $(1 + 2/\zeta\tau_\gamma)^{-1}$.

### 6.5.6 Phonon propagation

How the emitted phonons propagate from the emitter to the detector in the case of lateral arrangement on a Si surface was discussed by the Cornell University group in ref. [32, 33] on the basis of their experimental results. They have claimed that those phonons propagate from the emitter to the backside of the substrate, reflected there towards the surface and reach the detector. If we assume such a propagation path, the large difference in $\kappa$ and, therefore, $t_{\rm sub}$ between $d = 10\,\mu$m and $20\,\mu$m observed in Fig. 6.11 will not be elucidated because the difference in $d$ is $10\,\mu$m while the length of propagation from the surface to the backside of the substrate and back to the surface is 1.05 mm. The difference in $d$ is negligible for the long propagation length. We, thus, claim that the detected recombination phonons propagate nearly ballistically from the emitter to the detector near the surface of the substrate in the present case.

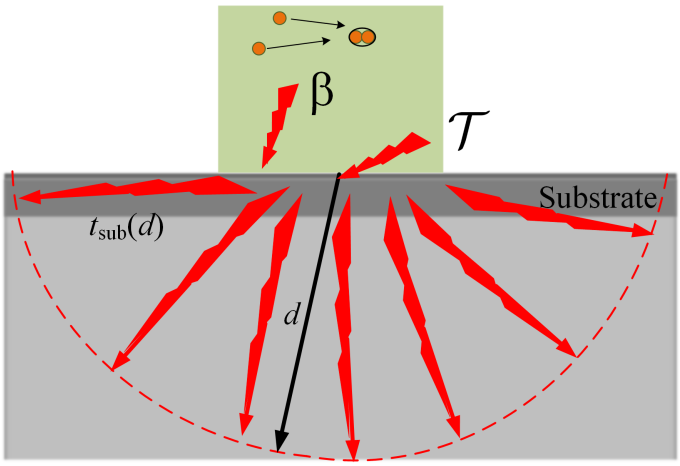


**Figure 6.16:** Schematic figure of isotropic phonon emission to the substrate with related transmission factors.

Assuming an isotropic emission of phonons from the SQUID emitter to the substrate and a uniform decay during the propagation as schematically depicted in Fig. 6.16, we may assume the phonon transmission factor vary with distance $d$ as $t_{\rm sub}(d) \propto d^{-2}\exp(-d/\lambda)$. From the obtained ratio

$$\frac{t_{\rm sub}(10\,\mu{\rm m})}{t_{\rm sub}(20\,\mu{\rm m})} = \frac{\kappa(10\,\mu{\rm m})}{\kappa(20\,\mu{\rm m})} \simeq 13,$$

we obtain

$$\exp\left(\frac{10\mu\mathrm{m}}{\lambda}\right) \simeq \frac{13}{2^2}$$

and the value of the characteristic decay length $\lambda \approx 8.6\ \mu$m. Because the phonon mean free path in a thermally grown amorphous $SiO_2$ at $T \leq 0.1\,\mathrm{K}$ is longer than $100\,\mu$m [75], there should be a decay mechanism of phonons in the present situation.

The existence of the $SiO_2$/Si interface may play a role. As far as the acoustic mismatch is concerned, however, phonons seem to transmit the interface almost perfectly: the acoustic impedances in $SiO_2$, $Z_{SiO_2}$, are $13.1 \times 10^6$ kg/m$^2$s for the longitudinal wave and $8.2 \times 10^6$ kg/m$^2$s for the transverse wave, respectively, from the density of the substance and the sound velocities in it, and those for Si, $Z_{Si}$, $19.8\times10^6$ kg/m$^2$s (longitudinal) and $13.6\times10^6$ kg/m$^2$s (transverse), respectively [76]. These give transmission ratios, $4Z_{SiO_2}Z_{Si}/(Z_{SiO_2}+Z_{Si})^2$, of 0.966 for the longitudinal wave and 0.947 for the transverse wave. However, with other model of transmission through the interface, lower transmission ratios have been estimated [76]. Thus, a leaky propagation within the $SiO_2$ layer repeating reflections at the interface and the surface (Fig. 6.17) may be the fashion of the phonon propagation. Further study is required to fully understand the phonon propagation in the present case. It is very important because many nano-scale devices are integrated on a surface of a semiconductor wafer. Therefore, understanding the phonon propagation between the surface devices is important for their performance.

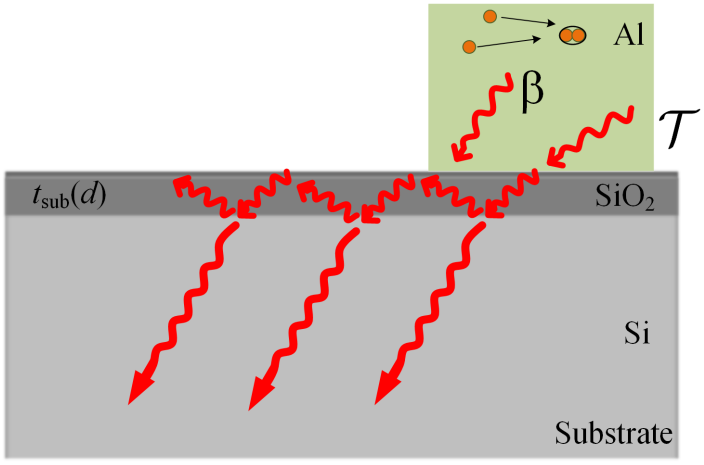


**Figure 6.17:** Schematic figure showing a possible propagation fashion of phonons partially reflected at the $SiO_2$/Si interface.

### 6.5.7 Comparison of features of SCPT and STJ detectors

Table 6.2: Comparison of features of SCPT and STJ detectors

| | SCPT detector | STJ detector |
|---|---|---|
| Spatial resolution | <1 $\mu$m<br>depends on<br>the fabrication design | <1 $\mu$m<br>depends on<br>the fabrication design |
| Operation temperature<br>(required refrigerator) | $< T^*$<br>typ.<300 mK for Al device<br>(dilution refrigerator) | $< T_c$<br><1.2 K for Al device<br>($^3$He refrigerator) |
| Sensitivity$^\dagger$ | $\sim 10^3$ | 1 |
| Phonon energy<br>resolution | None | None |
| Phonon polarization<br>resolution | None | None |
| Josephson effect<br>suppression with<br>a magnetic field | No need | Required |
| Extendability to<br>one phonon detection | possible$^{\dagger\dagger}$ | not possible |

$^\dagger$ the relative sensitivity with respect to the STJ detector
$^{\dagger\dagger}$ See the next subsection

There are many methods to measure a thermal conductance at room temperature using bolometric sensors, laser techniques such as the time-domain thermoreflectance, and scanning thermal microscopy [77]. All these methods do the sensing of a temperature change, and direct phonon detectors are few. In this subsection, we summarize the features of the SCPT phonon detector and compare them with those of the STJ phonon detector.

Table 6.2 is the summary of the comparison. The SCPT detector has a much higher sensitivity than the STJ detector although the SCPT detector needs a lower temperature to operate. It is also convenient for the SCPT detector that it doesn't need a magnetic field to suppress the Josephson effect.

### 6.5.8 Possible improvement

Although we argued that the effective range of the detector should be mainly near the junction up to the thinnest leads with the present structure, a better defined

local phonon detector will be easily fabricated. To make a local phonon detector, Al lead electrodes should be minimized near the junctions and normal metal leads be attached to them. The the active range is definitely defined very close to the junction.

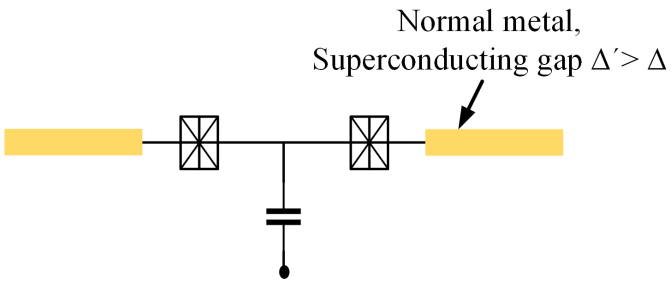


**Figure 6.18:** The improvement method for making a local phonon detector.

The normal metallic lead works as a quasiparticle trap [78]. In this case half the quasiparticles generated in the leads will escape to the normal metallic leads. To prevent this loss of efficiency, we can introduce a superconducting lead which has much larger superconducting gap $\Delta'$ than Al so that the energy of relevant phonons $\hbar\omega$ is in the range $\Delta < \hbar\omega < \Delta'$.

As described in 6.2, the observed dc $I_{\rm p}$ of SCPT is a time average current of $I_{\rm e}$ and $I_{\rm o}$, and $I_{\rm p}$ is fluctuating between $I_{\rm e}$ and $I_{\rm o}$. Every time a quasiparticle tunnels in the island (or a quasiparticle tunnels out of the island) and the parity becomes odd, $I_{\rm p}$ goes down from $I_{\rm e}$ to $I_{\rm o}$ by $\Delta I$. Thus, time-resolved measurement of $I_{\rm p}$ enables a one quasiparticle event. This gives a possibility to detect a single phonon. A method to operate single-electron devices in a radio frequency range was invented in 1998 by Schoelkopt et al [79]. By using this technique, as performed by a group in The University of New South Wales [20], a single phonon event can be detected.

## 6.6 Conclusion

We have proposed a sensitive phonon detection method using the supercurrent branch of a SCPT. We gave a quantitative model of the detection scheme based on the parity effect or quasiparticle poisoning effect of the SCPT and experimentally confirmed its operation with a SCPT that consisted of Al/AlO$_x$/Al mesoscopic

junctions. Through a emission-detection measurement of phonons with a proposed method, we obtained a sensitivity of the phonon detection nearly $10^3$ times as large as that of the traditional STJ method.

The high sensitivity is useful to search for the phonon propagation in the substrate for the nano-scale devices because the absolute magnitude of the thermal dissipation is low in those devices. Further, in superconducting qubit, even a low density flux of phonons with the energy larger than $2\Delta$ of the electrode affects the qubit operation severely by reducing the coherence time. Thus, high-sensitivity phonon detectors will be useful to examine the on-chip environment of the superconducting qubit system. Another feature is that the SCPT detector uses supercurrent, thus, its own dissipation is quite low, which is also a good point for a sensor on a quantum circuit.

We also discussed the operation temperature of the proposed detector and the effective spacial active range of the detector, thus, characterized the detector. We also found that there is a decay characteristic length of 8.6 $\mu$m of the propagation of the detected phonons. Its origin is a left problem to be understood in the future. We also discussed a possible improvement to make a local phonon detector, and to make a fast detection.

# Chapter 7

# Application of the phonon detection : the transport process in a one-dimensional array of mesoscopic Josephson junctions

## 7.1 Josephson junction Array

Arrays of Josephson junctions in one dimensional (1D) or 2D forms have been studied extensively in recent years, both theoretically and experimentally. The Josephson coupling energy and the charging energy characterise the array. For the 1D array, many aspects of the transport processes and quantum state of the system have been indicated in different studies, such as a charge soliton transport [80–82], alternate Cooper pair and quasiparticle transport [83], pinned charge-density wave [84] and Bose glass state [85] for the insulating state of the array, and so on. Further, in capacitively coupled bi-linear arrays of small Josephson junctions, induction of a current from one array to the other and duplication of a current have been observed [86, 87].

In this chapter, we focused on the conducting state of 1D array of such junctions and studied the transport process in terms of the energy dissipation from the array as phonons, which were detected using the SCPT detector described in chapter 6.

## Charge soliton model

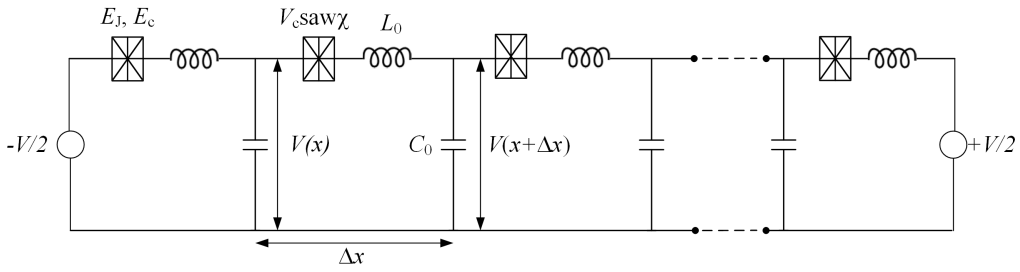


**Figure 7.1:** The equivalent circuit of a 1D array of small Josephson junctions.

Here, we will review the original charge soliton model for 1D array of small Josephson junctions first.

As explained in 2.1 (chapter 2), the quantum character of the Josephson phase $\varphi$ and its conjugate variable $Q$, the charge on the junction electrode, results in a band structure of the energy spectrum of an isolated single small Josephson junction. The energy spectrum becomes periodic with respect to a quasicharge $q$ with a period $2e$. Hence, when the particle state is in the lowest energy band $E_0(q)$, the observable voltage $V_j(q)$ across the junction as function of $q$ is expressed as

$$V_j(q) = \frac{dE_0(q)}{dq} = V_c \text{saw}\left(\frac{2\pi q}{2e}\right), \tag{7.1}$$

and the current is

$$I = \frac{dq}{dt}, \tag{7.2}$$

where $V_c$ is a characteristic voltage associated with the lowest energy band. The saw($q$) is a sawtooth-like $2\pi$-periodic odd function of $q$ with a value between $\pm 1$ [81, 88]. The voltage is a $2e$ periodic function of $q$, therefore, the voltage across the junction oscillates periodically in time with a period of $(2e/I)$ when a constant current $I$ (Eq. (7.2)) is fed to the function. Both $V_c$ and saw($q$) depend on the ratio $E_J/E_c$, where $E_c = e^2/(2C)$. For $E_J/E_c < 1$, the shape is sawtooth-like with

$V_c \simeq e/C$ and for $E_J/E_c > 1$, the shape is sinusoidal and $V_c$ decreases to zero exponentially in the ratio $\sqrt{E_J/E_c}$ [17]. Figure 7.1 shows an equivalent circuit of 1D array of $N$ such small Josephson junctions with inductive element $L$ and a self capacitance of each island between two junctions, $C_0$. Here, we assume the unit element has a length $\Delta x$.

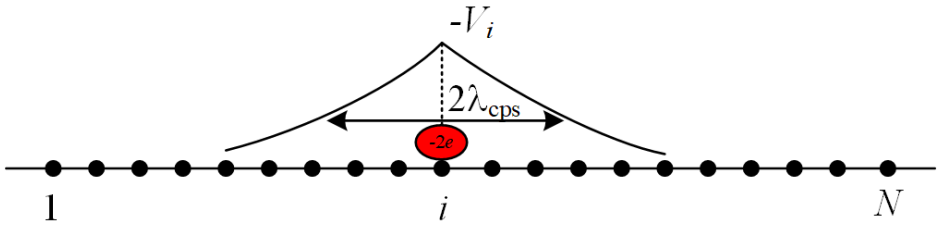


**Figure 7.2:** The Cooper-pair charge soliton. The black dots represent the island electrodes. $\lambda_{\rm cps}$ denotes the charge-soliton length.

The current along the array, $I(x,t)$, and the potential of the electrodes, $V(x,t)$, are functions of the spatial coordinate $x$ along the array. The circuit equations are expressed as

$$V(x+\Delta x,t) = V(x,t) - V_{\rm c}{\rm saw}\chi - L_0\frac{\partial I(x,t)}{\partial t} \tag{7.3}$$

$$I(x+\Delta x) = I(x,t) - C_0\frac{\partial V(x,t)}{\partial t} \tag{7.4}$$

In continuum limit, the current and voltage are related by

$$\partial_x V = -l_0\partial_t I - v_{\rm c}{\rm saw}(\pi q/e), \tag{7.5}$$

$$\partial_x I = -c_0\partial_t V, \tag{7.6}$$

where $l_0 = L_0/\Delta x$ and $c_0 = C_0/\Delta x$ are the distributed inductance and capacitance to the ground conductor, and $v_{\rm c} = V_{\rm c}/\Delta x$ is a critical electric field. Combining eqs. (7.2), (7.5) and (7.6) and a dimensionless quasicharge $\chi = \pi q/e$, together with the saw function being periodic on the interval. one obtains is

$$(1/c^2)\partial_{tt}\chi - \partial_{xx}\chi + (1/\lambda_{\rm cps}^2{\rm saw}(\chi)) = 0 \tag{7.7}$$

where $c = 1/\sqrt{c_0 l_0}$ is the electromagnetic wave velocity and $\lambda_{\rm cps} = \sqrt{2e/(2\pi c_0 v_{\rm c})}$. In the limit $E_{\rm J}/E_{\rm c} > 1$, $\mathrm{saw}(\chi) = \sin(\chi)$ and eq. (7.7) is the sine-Gordon equation, with a well-know Cooper-pair charge soliton solution as depicted in Fig. 7.2. The length $\lambda_{\rm cps}$ characterizes the spatial extent of the potential distribution as in Fig. 7.2 and is called *charge-soliton length*. With an injection and the subsequent passage of a single Cooper-pair charge soliton and antisoliton, each junction performs a single Bloch oscillation of the voltage between $-V_{\rm c}$ and $V_{\rm c}$ across it with a change in its quasicharge by $2e$ according to eq. (7.1) [82].

In a symmetric bias voltage across the array, the voltage that needs to inject a Cooper pair soliton into the array becomes $V_{\rm t} = 2\lambda_{\rm cps} V_{\rm c}$ and $V_{\rm t}$ is given as

$$V_{\rm t} = \frac{2}{\sqrt{\pi}} \sqrt{\frac{e}{C_0} V_{\rm c}} \tag{7.8}$$

This is the original model of a charge transport through a 1D array of small Josephson junctions introduced in Ref. [81].

### Later studies

The dynamics of interplay between the Cooper-pair and quasiparticle in one-dimensional (1D) charge Josephson junction arrays was studied by I. L. Ho et al. using a MonteCarlo simulation based on the perturbative tunneling of Cooper pairs and quasiparticles including an electromagnetic environment [83]. They have claimed that only Cooper-pair tunneling doesn't give the observed $I - V$ characteristic, but accompany of quasiparticle tunneling inside the array is necessary.

Watanabe et al. showed that a current in an array of small Josephson junctions affected the characteristics of a nearby SCPT [89]. Thus, there is a possibility of phonon and also photon emission from the array. We explored it quantitatively in this chapter.

## 7.2 Experimental methods

We produced a sample that consisted of the detector SCPT and the two emitters, 20 JJs array and dc-SQUID. The length $d$ of the detector from the SCPT to the two emitters was 10 $\mu$m. We used the SQUID as a reference for a well-defined phonon source.

The area of single Josephson junction for the SCPT and 20 JJs array were approximately 0.02 $\mu m^2$. The island's dimensions were 200 nm wide $\times$ 1 $\mu$m long. The size of junctions for the dc SQUID were approximately 0.01 $\mu m^2$ with the dc SQUID loop area was 0.6 $\mu$m $\times$ 3.6 $\mu$m. The devices were fabricated with $Al/AlO_x/Al$ tunnel junctions in the same method described in the previous sections.

In the measurement, the detector and the emitter were connected to two independent measurement circuits as shown in fig. 7.4(a) and (b). Bias voltages were applied to the detector and the emitter symmetrically to the ground using symmetrized voltage sources, and the four terminal point scheme was used for the measurement of $I - V$ characteristics of each circuit. In this experiment, the emission-detection measurements were performed for the array-SCPT and SQUID-SCPT pairs, as the result of the SQUID-SCPT pair for the reference.

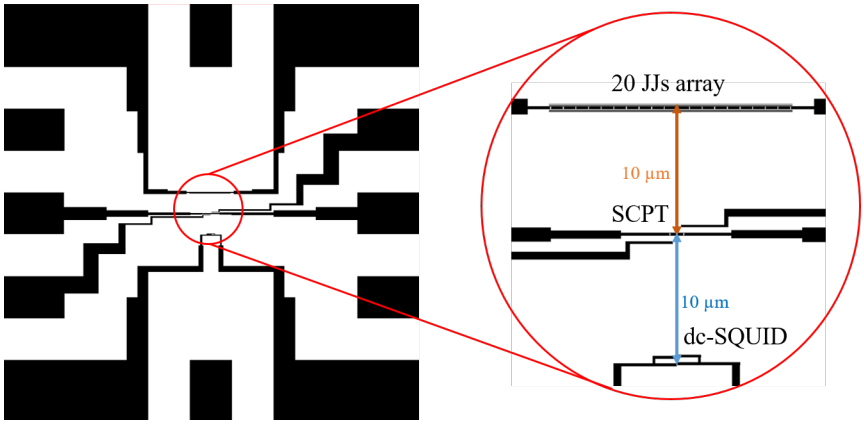


**Figure 7.3:** The pattern design of sample consists of the 20 JJs array, a SCPT, and dc-SQUID devices. The SCPT is a center between the array and SQUID with a length 10 $\mu$m.

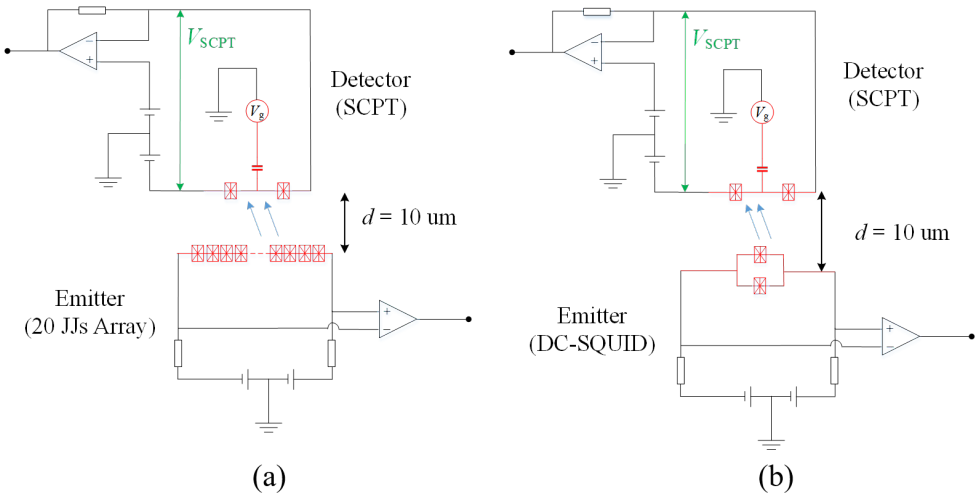


**Figure 7.4:** Measurement scheme for the SCPT detection the phonon propagation from 20 JJs Array (a) and SQUID (b). The distance between the emitter and the detector is 10 $\mu$m.

## 7.3 Experimental Results

Table 7.1: Parameters of the samples: distance from the SCPT $d$, tunnel resistance $R_{\mathrm{T}}$ of the junction, Josephson coupling energy $E_{\mathrm{J}}$ of the junction, charging energy $E_{\mathrm{c}}$, the $E_{\mathrm{J}}$ to $E_{\mathrm{c}}$ ratio, junction capacitance $C$, gate capacitance $C_g$ and the single junction area $A$.

| Sample | Device | $d$ | $R_{\mathrm{T}}$ | $C$ | $E_{\mathrm{J}}$ | $E_{\mathrm{c}}$ | $E_{\mathrm{J}}/E_{\mathrm{c}}$ | $C_g$ | $A$ |
|---|---|---|---|---|---|---|---|---|---|
| | | | kΩ | fF | $\mu$eV | $\mu$eV | | aF | $\mu$m$^2$ |
| | 20JJs array | 10 | 10.1 | 1.1 | 52 | 76 | 0.70 | - | 0.02 |
| 1 | SCPT | - | 10.5 | 0.70 | 56 | 53 | 1.1 | 13 | 0.02 |
| | SQUID | 10 | 15.1 | 0.40 | 42 | 200 | 0.21 | - | 0.01 |

The important parameters of all devices are shown in Table 7.1. We obtained the parameters in the same way as described in the previous sections.

Figure 7.5 exhibits the $I-V$ characteristic and the Coulomb oscillation of a SCPT. Figure 7.5 (a) shows the $I-V$ characteristic of a SCPT. One can see the supercurrent and the JQP peak. The supercurrent value of a SCPT in Fig. 7.5 (a) is about 1.57 nA. Figure 7.5 (b) shows the Coulomb oscillation of a SCPT at bias voltage 12 $\mu$V. The period of the oscillation was $2e$ in $C_{\mathrm{g}}V_{\mathrm{g}}$.

The $I-V$ characteristics of the 20 JJs array is shown in Fig. 7.6. Figure 7.6 (a) show the $I-V$ characteristic of the 20 JJs array at high voltage bias. The superconducting gap voltage width is about -8 mV to 8 mV. The small voltage gap due to the Coulomb blockade of Cooper-pair tunneling of the 20 JJs array is shown in Fig. 7.6 (b). At the threshold of $\pm 0.15$ mV, the Cooper-pair charge (anti)solitons start to tunnel in the array. There is a small Bloch nose structure, namely, back-bending of the $I-V$ curve observed.

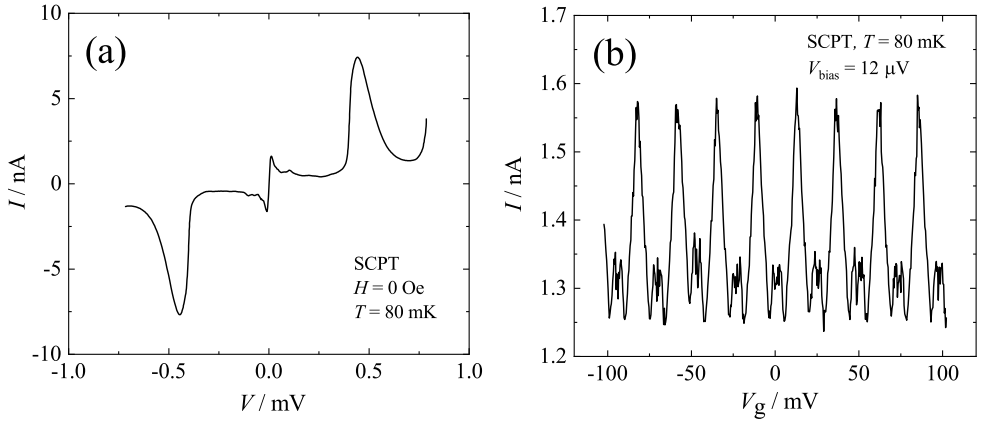


**Figure 7.5:** The $I-V$ characteristic of the SCPT (a) and the Coulomb oscillation of the SCPT with $V_{\text{bias}}$ at 12 $\mu$V (b) at $B = 0$ G and $T = 80$ mK.

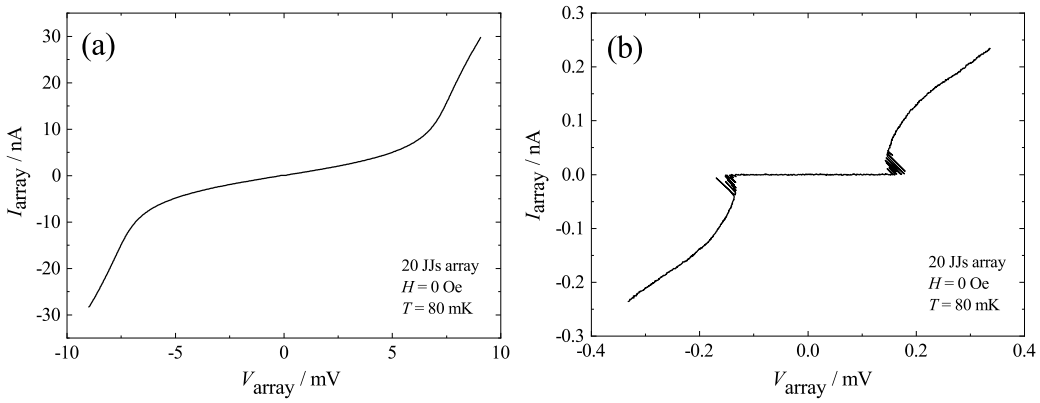


**Figure 7.6:** (a) The $I-V$ characteristic of the 20 JJs array at high voltage bias. (b) The $I-V$ characteristic of the 20 JJs array shows the $V_{\text{gap}}$ of 20 JJs array. It is measured at $H = 0$ Oe and $T = 80$ mK.

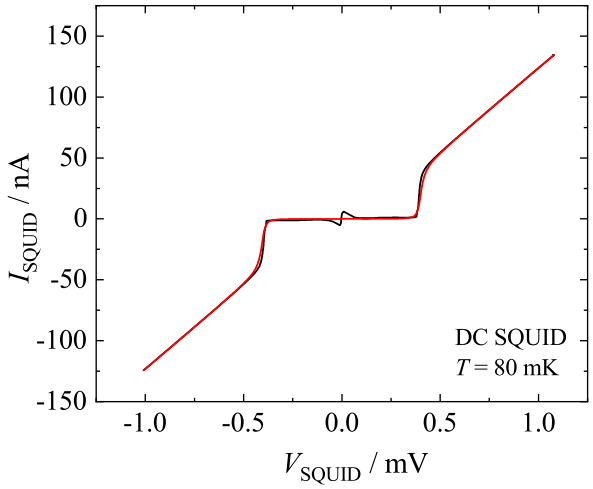


**Figure 7.7:** The $I - V$ characteristic of the dc-SQUID with applied the magnetic field ($\Phi = \Phi_0/2$) (red line) and no applied the magnetic field (black line).

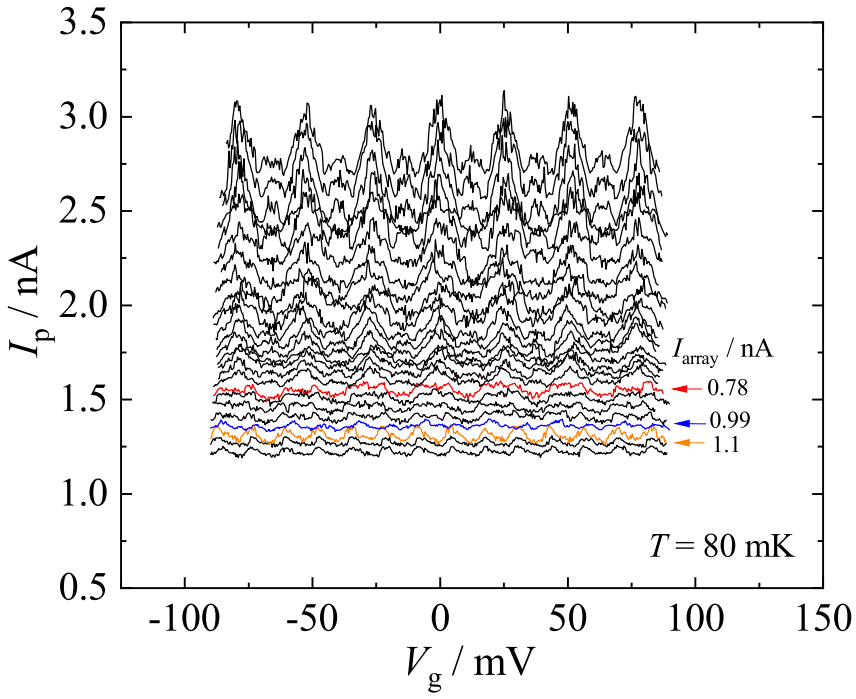


**Figure 7.8:** Observed changes in the Coulomb oscillation of the supercurrent of the SCPT. The oscillation period changes from $2e$ in $C_g V_g$ to $e$ as the bias increases in the array.

Figure 7.7 shows the $I - V$ characteristics of the SQUID with and without application of the magnetic flux of $\Phi_0/2$. When the $\Phi_0/2$ is applied the principal transport process is dominated by the quasiparticle tunneling when $V \geq 2\Delta$. The SQUID with a $\Phi_0/2$ magnetic flux becomes a source of phonons with the energy of $2\Delta$ or greater.

First, we examined whether the current in the array would affect the characteristic of the detector SCPT or not. We monitored the Coulomb oscillation of the supercurrent of the SCPT while changing the bias on the array. As can be seen in Fig. 7.8, the magnitude of the supercurrent starts to decrease as a current in the array. Its $2e$ periodic modulation of the SCPT almost disappears at $I_{\rm array} = 0.78$ nA. Then, at $I_{\rm array} = 1.0$ nA, the oscillation becomes $e$ periodic.

Next, we fixed the gate voltage to one of the Coulomb oscillation peaks, monitored its current magnitude $I_{\rm p}$, and scanned the bias in the array, $I_{\rm array}$. Figure 7.9 (a) is a plot of the measured $I_{\rm p}$ as a function of array current $I_{\rm array}$. With the increase in $I_{\rm array}$, $I_{\rm p}$ monotonically decreases, and almost becomes constant at $I_{\rm array} = \pm 2$ nA. Figure 7.9 (b) is the plot of $I_{\rm p}$ as a function of $V_{\rm array}$. This plot also shows a monotonically decrease in $I_{\rm p}$ with the increase in $V_{\rm array}$. We also performed, as a reference, the same measurement by scanning the bias on the SQUID with a half flux quantum $\Phi_0/2$ through the loop. Figure 7.10 is a plot of $I_{\rm p}$ as a function of $I_{\rm SQUID}$. In this case, $I_{\rm p}$ almost becomes constant when $I_{\rm SQUID} = \pm 30$ nA. Thus, the current in the array is more efficiently decreased $I_{\rm p}$ than the SQUID current by $\sim$ 15 times. Figure 7.11 shows plots of $I_{\rm p}$ as functions of frequencies of quasiparticle tunneling in the SQUID which the frequency is defined by $I_{\rm qp}/e$ (Fig. 7.11(a)) and of Cooper-pair charge soliton injection in the array for which the frequency is defined by $I_{\rm array}/2e$ (Fig. 7.11(b)). This also shows the efficiency of the Cooper-pair charge solitons to decrease $I_{\rm p}$. For example, for $I_{\rm p}$ to be decreased to 1.3 nA, quasiparticle tunneling in the SQUID needs a frequency of approximately 100 GHz while Cooper-pair tunneling needs a frequency of 3 GHz.

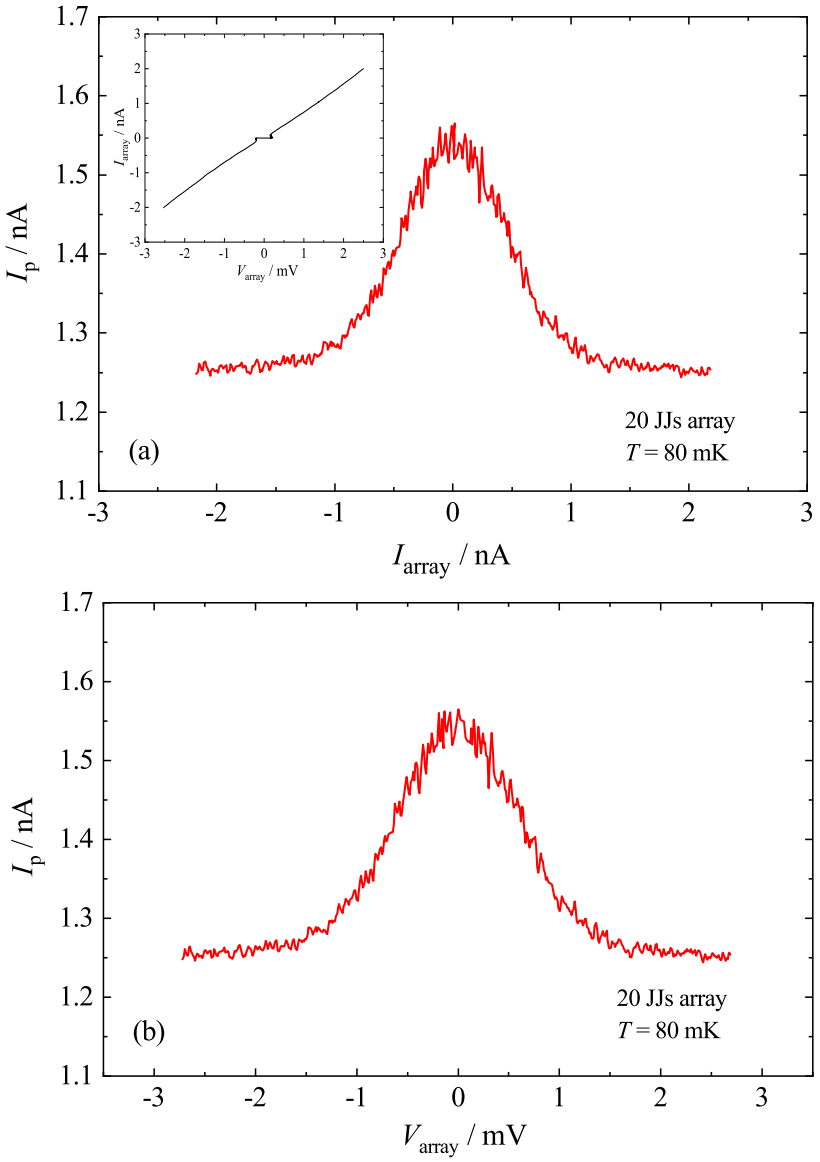


**Figure 7.9:** Plots of the current magnitude $I_p$ with fixing the gate voltage to one of the Coulomb oscillation peaks when scanned the bias current in the array, (a) as a function of array current, (b) as a function of array voltage. Inset of (a): The $I - V$ characteristic of the 20 JJs array.

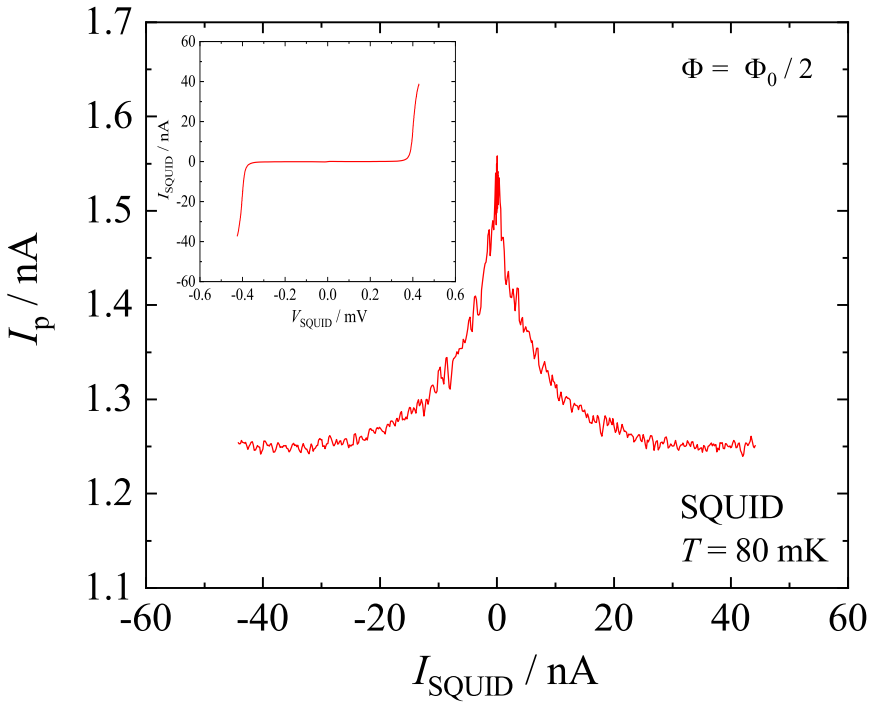


**Figure 7.10:** A plot of the current magnitude $I_p$ with fixing the gate voltage to one of the Coulomb oscillation peaks scanning the bias current in the inset : The $I - V$ characteristic of the SQUID with applied the magnetic flux $\Phi_0/2$.

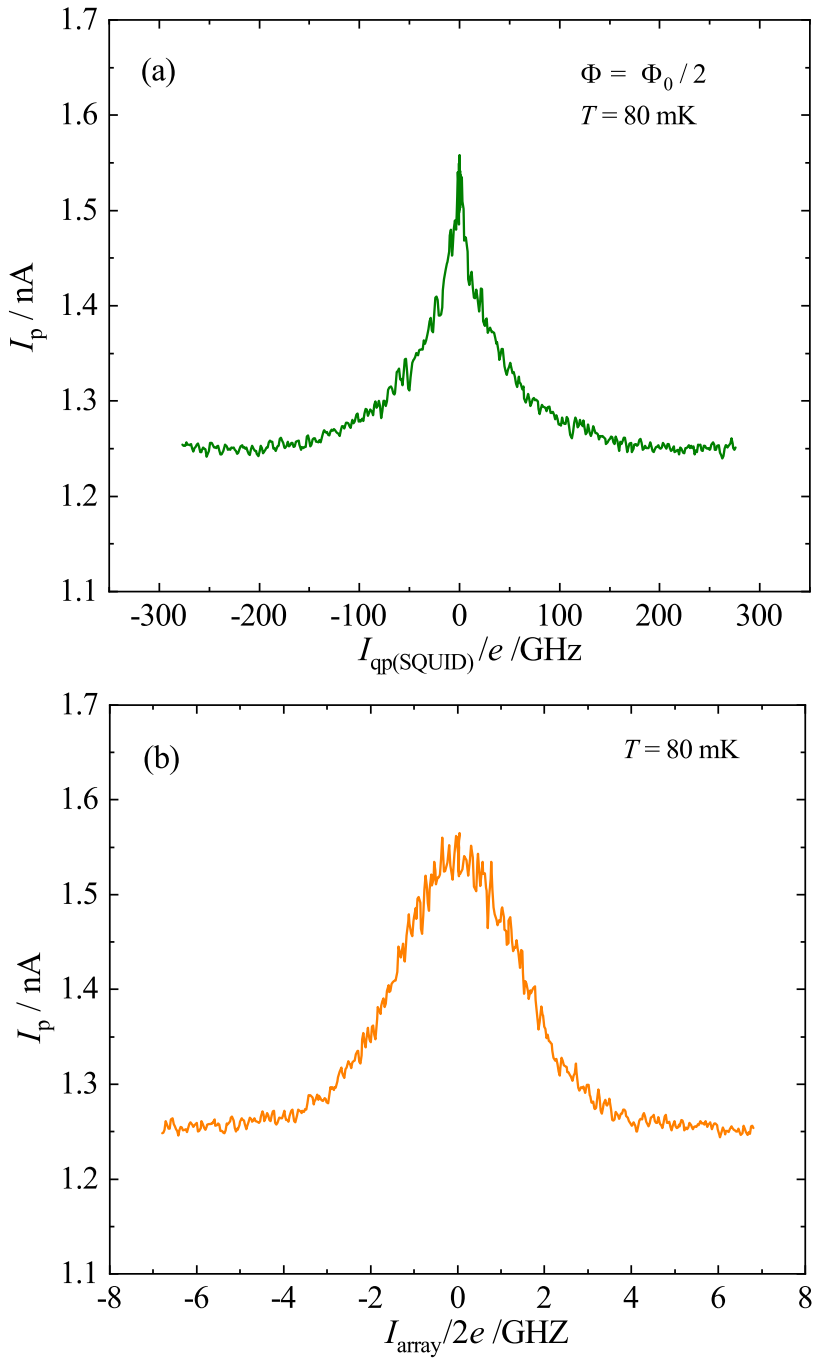


**Figure 7.11:** The plot between the current magnitude $I$ with the fixed the gate voltage of one of the Coulomb oscillation peaks when scanned the bias current in the SQUID (a) and in the array (b), with the frequency of quasiparticle tunneling.

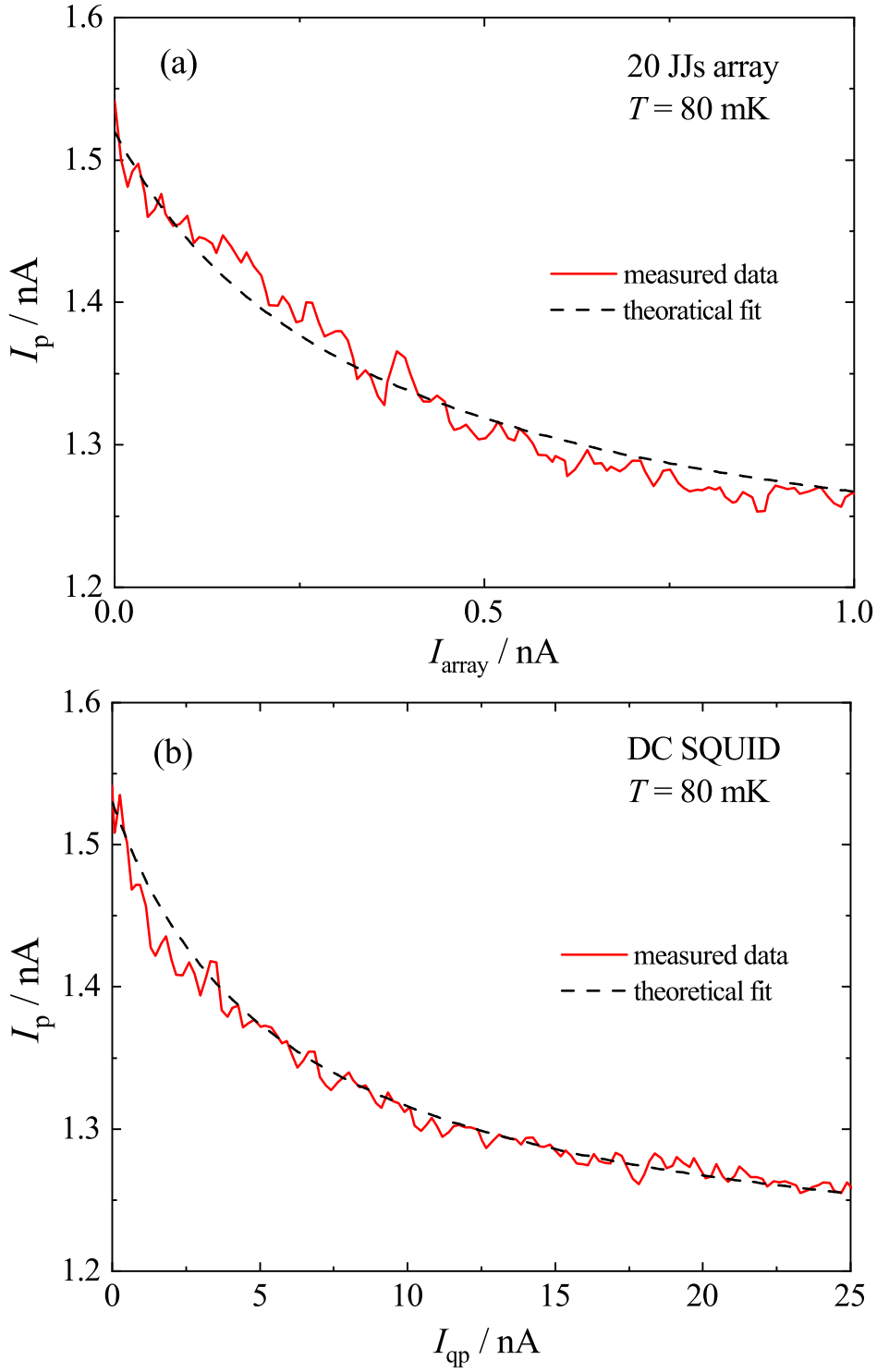


**Figure 7.12:** The SCPT supercurrent-peak change with the array current (a) and with the quasiparticle current from the SQUID emitter (b) ($d = 10$). The broken line: a theoretical. Fitting parameters : $I_o = 1.18$ nA, $\Delta I = 0.34$ nA, $\kappa = 2.9 \times 10^9$ s and $1.7 \times 10^8$ s for the 20 JJs array (a) and the SQUID emitter (b), respectively.

## 7.4 Discussion and Conclusion

What is remarkable in the observed results is the high efficiency of the array current or the Cooper-pair tunneling in the array to decrease $I_{\rm p}$ of SCPT in comparison with the case for the quasiparticle tunneling in the SQUID. To evaluate it quantitatively, we estimated $\kappa$ in eq. (6.11) in both cases by fitting the formula to the experimental results. Figures 7.12(a) and (b) show the results of the fitting. For the result of the SQUID, we took the quasiparticle current $I_{\rm qp}$ as the quantity in the horizontal axis as in chapter 6. The obtained $\kappa$ for the array case, $\kappa_{\rm ar}$ is $2.9 \times 10^9$ s and that for the SQUID case, $\kappa_{\rm SQ}$ is $1.7 \times 10^8$ s. The ratio $\kappa_{\rm ar}/\kappa_{\rm SQ}$=17.

We proceed with analysis assuming that decreasing of $I_{\rm p}$ in SCPT is caused by the array current $I_{\rm array}$ via phonons. As defined in chapter 6, $\kappa = \gamma t_{\rm sub}(d)\mathcal{T}\beta/e$. $\gamma$ is associated with only the detector, and $t_{\rm sub}(d)$ is with the substrate. Because the distance $d$ between the detector SCPT and either emitters is 10 $\mu$m, we may take $t_{\rm sub}(d)$ is the same in both cases. $\mathcal{T}$ is the phonon transmission coefficient from Al to the substrate, which is the same in both the array and the SQUID. Thus, the large difference should be ascribed to the difference in $\beta$'s for the array and for the SQUID. $\beta$ is the phonon generation rate per unit current. Thus, in the array, phonons are by 17 times more efficiently generated than in the SQUID with the same magnitude of the flowing current.

The decrease in $I_{\rm p}$ when the bias on the array is scanned starts as soon as a finite current flows in the array at $V_{\rm th}$, approximately 150 $\mu$V in the present case, which was also observed by Watanabe et al [89]. Because we used a symmetric biasing with respect to ground, the magnitude of the voltage difference between the edge voltage and the ground, $V_{\rm e}$, is estimated to be approximately 75 $\mu$V as schematically demonstrated in Fig. 7.13. If we consider the soliton length in the array, the maximum voltage across the junction is $V_{\rm e}(1 - \exp(-1/\lambda)) = 0.09V_{\rm e} = 7$ $\mu$V in the present case using $C_0 = 9$ aF [90]. Thus, the ac Josephson effect cannot produce a photon with an energy $\geq 2\Delta$ at around $V_{\rm e}$. As far as we observe the $I_{\rm p}$–$V_{\rm array}$ characteristic in Fig. 7.9(b), the dependence of $I_{\rm p}$ on $V_{\rm array}$ is monotonic and with no special structure. This means that we can assume a single origin for this phenomenon and, hence, can exclude the photon effect.

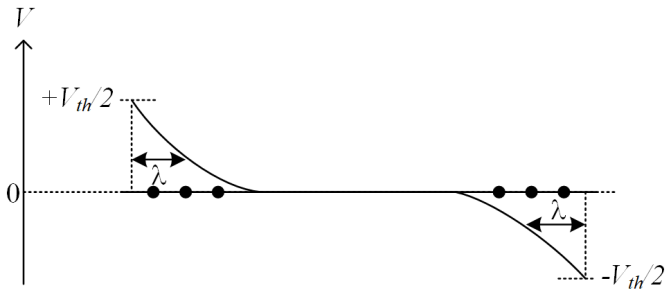


**Figure 7.13:** The voltage distribution over the array for symmetric biasing.

Thus, phonons are the most probable candidate. So far there is no direct prediction of phonon generation with a current in the array of small Josephson junctions. However, the results of simulation by Ho et al. [83] are suggestive. As explained in 7.1, they have claimed that the Cooper-pair tunneling transport inevitably accompanies quasiparticle tunnelings. When a Cooper-pair-soliton and anti-soliton meet at both sides of a junction, there appears a large voltage difference across the junction (Fig. 7.14 (a)), and because of it, Cooper-pair tunneling is prohibited there. Thus, the solitons and anti-solitons accumulate there (Fig. 7.14 (b)) till quasiparticle tunnelings occur and relax the voltage difference. In this case, quasiparticles are accumulated in the electrodes in the array, causing generation of recombination and relaxation phonons. Hence, our result conversely supports this picture of alternate Cooper-pair and quasiparticle tunneling in the conductive state of 1D array of mesoscopic Josephson junctions.

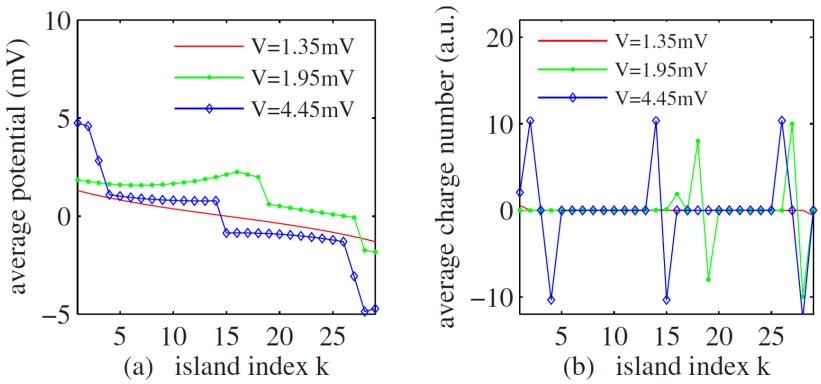


**Figure 7.14:** The results of simulation by Ho el al. [83] Under the CP-only dynamics, the profiles of (a) average potential and (b) average charge number over a period 0.1 ms for individual island at different biases $V = V_{\mathrm{cr,CP}} \cong 1.35$, $V = 1.95$, and $V = 4.45$ mV.

As for the efficiency of the phonon generation, there is a possibility such quasiparticle tunnelings occur multiple times in the array for a single Cooper-pair passage. Also, in the case of array, the generated quasiparticles well localize in the island electrode and the recombination probability is enhanced in comparison with the case in SQUID, where the generated quasiparticles diffuse in the outer electrodes. Further study is required to clarify this point.

# Chapter 8

# Conclusion

The SCPT is the basic single-charge-tunneling device in which dc transport characteristics can be correlated to the duality between charge and phase, and, thus, electrostatic control of a supercurrent is possible. The physics of the SCPT explains the properties of a supercurrent through the SCPT and its gate modulation. The supercurrent of the SCPT can be used for highly sensitive sensing. However, because of the limitation of small supercurrent modulation, it has not been widely applied in practice with other superconducting circuits. In this thesis, we studied possibilities to apply SCPTs to practical electronic devices. In the first part, we studied the possibility to combine the SCPT with other superconducting circuits. In the second part, as a specific practical application of the modulable supercurrent through a SCPT, we proposed and experimentally confirmed a sensitive phonon detection by using the SCPT. We designed the devices and experiments for each application, fabricated them by using the high-resolution electron beam lithography (EBL) technique and the shadow evaporation technique, and the transport measurements were performed at the temperature lower than 100 mK with a dilution refrigerator.

As the first part, in chapter 4, we studied the possibility to increase the modulable supercurrent by using multiple SCPTs connected in parallel having a common gate. We found that the maximum supercurrent $I_{\rm pp}$ that flew through $N$ parallel SCPTs was scaled up almost linearly with the increase in $N$. When the gate voltage modulated at the $I_{\rm p}$ in the SCPT in parallel circuits have the Coulomb oscillations as

in a single SCPT. However, the width of the current peak of the Coulomb oscillation as well as the relative magnitude of valley current $I_{\rm pv}/I_{\rm pp}$ of the oscillation increase with the increase in $N$. These experimental observations were analyzed from the view points of random offset charges and charge state fluctuations. It turns out that the latter is the main origin. Some improvement methods of modulability were discussed. This method gives a way to increase by orders the magnitude of a well gate-modulable supercurrent.

In chapter 5, we studied the property of a SCPT when it is inserted in a dc SQUID geometry. We observed the supercurrent through the SCPT-SQUID loop kept the periodic modulation of the supercurrent with respect to a magnetic flux with a period of $\Phi_0$. Thus, the supercurrent through the SCPT maintains the superconducting coherence, and also it can be modulated with the gate voltage. However, the modulation of the SCPT on and off is not large. Considering the effect of the charge fluctuations in the SCPT, we simulated for two, three and four charge states. The simulation characteristic with four and three charge states show a realistic characteristics of the switching of the SCPT and correspond to the measured $I_{\rm s} - B$ characteristics with the gate modulation. Thus, this study indicates that a SCPT can be used as a supercurrent switch. However, when one designs a superconducting circuit including SCPTs, it is necessary to consider the charge fluctuations and the modulation change due to these charge fluctuations.

In chapters 6 and 7, we focused on the application of a single Cooper-pair transistor as a high sensitive phonon detector. In chapter 6, we proposed a possibility to detect phonons by SCPT on the basis of the parity effect associated with nonequilibrium quasiparticles. We proposed a quantitative model of the detector, explaining the experimental results observed. In the experiment, we examined how the magnitude of the supercurrent flowing through a SCPT varies as a quasiparticle tunneling current in the SQUID emitter is increased. The observed change in the oscillation, particularly, the magnitude of the peak current, is very well fitted to the proposed quantitative model. It turns out that the sensitivity $\Delta I_{\rm p}/\Delta I_{\rm qp}$ in our SCPT for $d = 10$ $\mu$m and $I_{\rm p} \simeq 5$ nA is approximately 0.03. This was about 1000 times higher than that of the conventional detection method using STJ's quasiparticle tunnel current change. From our results of phonon propagation coefficient, we

derived a decay length of phonons of 8.6 $\mu$m. This suggests a propagation mode of phonons on the surface of substrate, which would need further clarification. Because many nanoscale devices are fabricated on the surface of semiconductor wafers, understanding the phonon propagation near the surface is very important for their performance. Our sensitive device is very effective tool to study phonon transport. This is a future problem needed to be studied, including the realization of a well defined local detector as well as a fast detection method.

In chapter 7, we studied the transport process in an one-dimensional array of mesoscopic Josephson junctions through the detection of strong phonon flux with the SCPT detector. The supercurrent through a SCPT detector decreased as a current started to flow in the array in the same way as a quasiparticle current in a SQUID emitter. Therefore, phonons with an energy $> 2\Delta$ are generated by the current in the array. We estimated $\kappa$ in eq. (6.11) for the array case, $\kappa_{\rm ar}$ to be $2.9 \times 10^9$ s and that for the SQUID case, $\kappa_{\rm SQ}$ to be $1.7 \times 10^8$ s. Their ratio is $\kappa_{\rm ar}/\kappa_{\rm SQ} = 17$. We, thus, found that the current in the array was very efficient in generating phonons. These observed results may support the transport process proposed by Ho et al. on the basis of their MonteCarlo simulation, where the interplay between the Cooper-pair and quasiparticles play an important role [83]. We revealed a new aspect of the transport properties of the current in the array of small Josephson junctions experimentally.

# Bibliography


[1] B. Josephson, "Possible new effects in superconductive tunneling," *Phys. Lett.* **1**, p. 251, 1962.

[2] F. Tafuri, *Fundamentals and Frontiers of the Josephson Effect, Chapter 1 Introductory Notes on the Josephson Effect: Main Concepts and Phenomenology.* vol. 286, Edited by Francesco Tafuri, Springer Nature Switzerland AG, 2019.

[3] K. K. Likharev and V. K. Semenov, "RSFQ logic/memory family: A new josephson-junction technology for sub-terahertz-clock-frequency digital systems," *IEEE Trans. Appl. Supercond.* **1**, p. 3, 1991.

[4] W. Nawrocki, *Introduction to Quantum Metrology, Quantum Standards and Instrumentation.* Springer International Publishing Switzerland, Chap.4, p.76, 2015.

[5] L. J. Geerligs, V. F. Anderegg, J. Romijn, and J. E. Mooij, "Single cooper-pair tunneling in small-capacitance junctions," *Phys. Rev. Lett.* **65**, p. 377, 1990.

[6] M. T. Tuominen, J. M. Hergenrother, T. S. Tighe, and M. Tinkham, "Experimental evidence for parity-based 2e periodicity in a superconducting single-electron tunneling transistor," *Phys. Rev. Lett.* **69**, p. 1997, 1992.

[7] Y. Nakamura, Y. Pashkin, and J.-S. Tsai, "Coherent control of macroscopic quantum states in a single-cooper-pair box," *Nature* **398**, p. 786, 1999.

[8] P. W. Anderson and J. M. Rowell, "Probable observation of the josephson superconducting tunneling effect," *Phys. Lett.* **10**, p. 230, 1963.

[9] R. P. Feynman, R. B. Leighton, and M. Sands, *The Feynman's lectures on Physics.* Vol. III, Quantum Mechanics, paragraph 21.9, Addison-Wesley Publishing Company, 1965.

[10] V. Ambegaokar and A. Baratoff, "Tunneling between superconductors," *Phys. Rev. Lett.* **10**, *[Errata* **11**, *p.104 (1963)]*, p. 486, 1963.

[11] K. K. Likharev and A. B. Zorin, "Theory of the bloch-wave oscillations in small josephson junctions," *J. Low Temp. Phys.* **59**, p. 347, 1985.

[12] A. Fulton, P. L. Gammel, D. J. Bishop, L. N. Dunkleberger, and G. J. Dolan, "Observation of combined josephson and charging effects in small tunnel junction circuits," *Phys. Rev. Lett.* **63**, p. 1307, 1989.

[13] P. Hadley, E. Delvigne, E. H. Visscher, S. Lähteenmäki, and J. E. Mooij, "$3e$ tunneling processes in a superconducting single-electron tunneling transistor," *Phy. Rev. B* **58**, p. 15317, 1998.

[14] P.-M. Billangeon, F. Pierre, H. Bouchiat, and R. Deblock, "Ac Josephson effect and resonant cooper pair tunneling emission of a single cooper pair transistor," *Phys. Rev. Lett.* **98**, p. 216802, 2007.

[15] ——, "Emission and absorption asymmetry in the quantum noise of a josephson junction," *Phys. Rev. Lett.* **96**, p. 136804, 2006.

[16] M. Tinkham, *Introduction to Superconductivity, 2nd ed.* Dover, New York, 2004.

[17] A. B. Zorin, "Quantum-limited electrometer based on single cooper pair tunneling," *Phys. Rev. Lett.* **76**, p. 4408, 1996.

[18] L. I. Glazman, F. W. J. Hekking, K. A. Matveev, and R. I. Shekhter, "Charge parity in josephson tunneling through a superconducting grain," *Physica B* **203**, p. 316, 1994.

[19] J. Aumentado, M. W. Keller, J. M. Martinis, and M. H. Devoret, "Nonequilibrium quasiparticles and 2e periodicity in single-cooper-pair transistors," *Phys. Rev. Lett.* **92**, pp. 066 802–1, 2004.

[20] N. A. Court, *Quasiparticle Dynamics in a Single Cooper-Pair Transistor.* PhD thesis, The University of New South wales,, 2008.

[21] J. Aumentado, *Handbook of Nanophysics: Nanoelectronics and Nanophotonics.* Ed. K. D. Sattler, (CRC Press, Boca Raton, 2011) Chap. 16., 2011.

[22] M. T. Bell, L. B. Ioffe, and M. E. Gershenson, "Microwave spectroscopy of a cooper-pair transistor coupled to a lumped-element resonator," *Phys. Rev. B* **86**, p. 144512, 2012.

[23] L. Tosi, D. Vion, and H. le Sueur, "Design of a cooper-pair box electrometer for application to solid-state and astroparticle physics," *Phys. Rev. Applied* **11**, p. 054072, 2019.

[24] D. Vion, A. Aassime, A. Cottet, P. Joyez, H. Pothier, C. Urbina, D. Esteve, and M. H. Devoret, "Manipulating the quantum state of an electrical circuit," *Science* **296**, p. 886, 2002.

[25] D. J. van Woerkom, A. Geresdi, and L. P. Kouwenhoven, "One minute parity lifetime of a nbtin cooper-pair transistor," *Nat. Phys.* **11**, p. 547, 2015.

[26] I. Giaever, H. R. Hart, Jr., and K. Megerle, "Tunneling into superconductors at temperatures below 1k." *Phys. Rev.* **126**, p. 941, 1962.

[27] P. Seidel, *Applied Superconductivity, Handbook on Devices and Applications.* Wiley VCH Verlag GmbH and Co.KGaA, Boschstr. 12, 69469 Weinheim, Germany,, 2015.

[28] W. Eisenmenger, *Physical Acoustics, Chap. 2.* vol. XII, Edited by W. P. Mason, and R. N. Thurston (Academic Press, New York), 1976.

[29] E. Burstein, D. N. Langenberg, and B. N. Taylor, "Superconductors as quantum detectors for microwave and sub-millimeter-wave radiation," *Phys. Rev. Lett.* **6**, p. 92, 1961.

[30] J. R. Schrieffer and D. M. Ginsberg, "Calculation of the quasiparticle recombination time in a superconductor," *Phys. Rev. Lett.* **8**, p. 207, 1962.

[31] W. Eisenmenger and A. H. Dayem, "Quantum generation and detection of incoherent phonons in superconductors," *Phys. Rev. Lett.* **18**, p. 125, 1967.

[32] J. B. Hertzberg, O. O. Otelaja, N. J. Yoshida, and R. Robinson, "Non-equilibrium phonon generation and detection in microstructure devices," *Rev. Sci. Instrum.* **82**, p. 104905, 2011.

[33] O. O. Otelaja, J. B. Hertzberg, M. Aksit, and R. D. Robinson, "Design and operation of a microfabricated phonon spectrometer utilizing superconducting tunnel junctions as phonon transducers," *New J. Phys.* **15**, p. 043018, 2013.

[34] J. B. Hertzberg, M. Aksit, O. O. Otelaja, D. A. Stewart, and R. D. Robinson, "Direct measurements of surface scattering in si nanosheets using a microscale phonon spectrometer: Implications for casimir-limit predicted by ziman theory," *Nano Lett.* **14**, p. 403, 2014.

[35] O. O. Otelaja and R. D. Robinson, "Enhancement of phonon backscattering due to confinement of ballistic phonon pathways in silicon as studied with a microfabricated phonon spectrometer," *Appl. Phys. Lett.* **107**, p. 173102, 2015.

[36] MicroChem, *LOR and PMGI Resists Data sheet.* Technical Data, MicroChem, 2019.

[37] SHIPLEY, *Microposit S1800 Series Photo Resists Data sheet.* Technical Data, SHIPLEY, 2014.

[38] G. J. Dolan, "Offset masks for lift-off photoprocessing," *Appl. Phys. Lett.* **31**, p. 337, 1977.

[39] MicroChem, *NANO*$^{\text{TM}}$*PMMA and Copolymer Data sheet.* Technical Data, MicroChem, 2001.

[40] O. V. Lounasmaa, *Experimental Principles and Methods Below 1K.* Academic Press, New yark: USA, 28, 1974.

[41] Y. Ootuka, T. Uchiyama, and H. Shimada, "One-day dilution refrigerator," *Cryogenics* **33**, p. 923, 1993.

[42] A. Aassime, D. Gunnarsson, K. Bladh, and P. Delsing, "Radio-frequency single-electron transistor: Toward the shot-noise limit," *Appl. Phys. Lett.* **79**, p. 4031, 2001.

[43] C. P. Heij, P. Hadley, and J. E. Mooij, "Charge spectrometry with a strongly coupled superconducting single-electron transistor," *Phys. Pev. B* **64**, p. 245116, 2001.

[44] H. Grabert and M. H. Devoret, *Single Charge Tunneling: Coulomb Blockade Phenomena in Nanostructures.* Plenum: New York and London,, 1992.

[45] R. Deblock, E. Onac, L. Gurevich, and L. P. Kouwenhoven, "Detection of quantum noise from an electrically driven two-level system," *Science* **301**, p. 203, 2003.

[46] Y. Nazarov and Y. Blanter, *Quantum Transport.* Cambridge University Press, Cambridge, 2009.

[47] D. Born, V. I. Shnyrkov, W. Krench, T. Wagner, E. Il'ichev, M. Grajcar, U. Hübner, and H.-G. Meyer, "Reading out the state inductively and microwave spectroscopy of an interferometer-type charge qubit," *Phys. Rev. B* **70**, p. 180501, 2004.

[48] H. Zangerle, J. Könemann, B. Mackrodt, R. Dolata, S. V. Lotkhov, S. A. Bogoslovsky, M. Götz, and A. B. Zorin, "Ground-state characterization of nb charge-phase josephson qubits," *Phys. Rev. B* **73**, p. 224527, 2006.

[49] A. B. Zorin, "Cooper-pair qubit and cooper-pair electrometer in one device," *Physica C* **368**, p. 284, 2002.

[50] A. B. Zorin and Z. Éksp. Teor. Fiz, "Josephson charge-phase qubit with radio frequency readout: Coupling and decoherence," *JETP* **98**, p. 1250, 2004.

[51] P. Agren, J. Waltelr, V. Schöllmann, and D. B. Haviland, *International Workshop on Superconducting Nano-Electronics Devices.* ed. J. Pekola, B. Ruggiero, and P. Silvestrini (Kluwer Academic/Plenum Publishers, New York) p. 25, 2002.

[52] R. Dolata, H. Scherer, A. B. Zorin, and J. Niemeyer, "Single electron transistors with high-quality superconducting niobium islands," *Appl. Phys. Lett.* **80**, p. 2776, 2002.

[53] N. Kim, K. Hansen, S. Paraoanu, and J. Pekola, "Fabrication of nb-based superconducting single electron transistor," *Physica B* **329-333**, p. 1519, 2003.

[54] R. Dolata, H. Scherer, A. B. Zorin, and J. Niemeyer, "Single-charge devices with ultrasmall nb/alox/nb trilayer josephson junctions," *J. Appl. Phys.* **97**, p. 054501, 2005.

[55] D. J. van Woerkom, A. Geresdi, and L. P. Kouwenhoven, "One minute parity lifetime of a nbtin cooper-pair transistor," *Nat. Phys.* **11**, p. 547, 2015.

[56] O. Mukhanov, N. Yoshikawa, I. P. Nevirkovets, and M. Hidaka, *Fundamentals and Frontiers of the Josephson Effect.* Ed. F. Tafuri (Springer) Chap. 16., 2019.

[57] J. Gallop and L. Hao, *Fundamentals and Frontiers of the Josephson Effect.* Ed. F. Tafuri (Springer) Chap. 14., 2019.

[58] S. Nakamura, Y. A. Pashkin, J.-S. Tsai, and N. Kaneko, "Single-electron pumping by parallel sinis turnstiles for quantum current standard," *IEEE Trans. Instrum. Measur.* **64**, p. 1696, 2015.

[59] G. Dillard, "A moving-window detector for binary integration," *Proc. IEEE Trans. Inf. Theory* **13**, p. 616, 1967.

[60] G. E. Johnson, "Constructions of particular random processes," *Proc. IEEE* **82**, p. 270, 1994.

[61] P. W. Anderson, *Lectures on the Many-Body Problem.* vol. 2, ed. E. R. Caianiello (Academic Press) p. 113., 1964.

[62] H. Shimada, T. Koike, K. Kikkawa, H. Konno, R. Kobayashi, Y. Mizugaki, K. Kanomata, M. Miura, and F. Hirose, "Nanoscale tunnel junctions and metallic single-electron transistors via shadow evaporation and in situ atomic layer deposition of tunnel barriers," *Nano Mater.* **4**, p. 1401, 2021.

[63] Y. Pashkin, Y. Nakamura, and J.-S. Tsai, "Implementation of single-electron transistor with resistive gate," *Jpn. J. Apple. Phys.* **38**, p. 406, 1999.

[64] N. Li, J. Ren, L. Wang, G. Zhang, P. Hänggi, and B. Li, "Colloquium: Phononics: Manipulating heat flow with electronic analogs and beyond," *Rev. Mod. Phys.* **84**, p. 1045, 2012.

[65] S. Volz, J. Ordonez-Miranda, A. Shchepetov, M. Prunnila, J. Ahopelto, T. Pezeril, G. Vaudel, V. Gusev, P. Ruello, E. M. Weig, M. Schubert, M. Hettich, M. Grossman, T. Dekorsy, F. Alzina, B. Graczykowski, E. Chavez-Angel, J. S. Reparaz, M. R. Wagner, C. M. Sotomayor-Torres, S. Xiong, S. Neogi, and D. Donadio, "Nanophononics: state of the art and perspectives," *Eur. Phys. J. B* **89**, p. 15, 2016.

[66] J. P. Pekola and I. M. Khaymovich, "Thermodynamics in single-electron circuits and superconducting qubits," *Ann. Rev. Condens. Matter Phys.* **10**, p. 193, 2019.

[67] R. M. Lutchyn and L. I. Glazman, "Kinetics of quasiparticle trapping in a cooper-pair box," *Phys. Rev. B* **75**, p. 184520, 2007.

[68] M. D. Shaw, R. M. Lutchyn, P. Delsing, and P. M. Echternach, "Kinetics of nonequilibrium quasiparticle tunneling in superconducting charge qubits," *Phys. Rev. B* **78**, p. 024503, 2008.

[69] M. T. Tuominen, J. M. Hergenrother, T. S. Tighe, and M. Tinkham, "Experimental evidence for parity-based 2e periodicity in a superconducting single-electron tunneling transistor," *Phys. Rev. Lett.* **69**, p. 1997, 1992.

[70] D. C. Hurley and J. P. Wolfe, "Phonon focusing in cubic crystals," *Phys. Rev. B* **32**, p. 2568, 1985.

[71] N. A. Court, A. J. Ferguson, R. Lutchyn, and R. G. Clark, "Quantitative study of quasiparticle traps using the single-cooper-pair transistor," *Phys. Rev. B* **77**, p. 100501(R), 2008.

[72] V. Savu, L. Frunzio, and D. E. Prober, "Enhancing the energy resolution of a single photon stj spectrometer using diffusion engineering," *IEEE Trans. Appl. Supercond.* **17**, p. 324, 2007.

[73] C. M. Wilson, *The development of single-photon spectrometers using superconducting tunnel junctions.* PhD thesis, Yale University, 2002.

[74] A. Rothwarf and B. N. Taylor, "Measurement of recombination lifetimes in superconductors," *Phys. Rev. Lett.* **19**, p. 27, 1967.

[75] P. D. Vu, J. R. Olson, and R. O. Pohl, "Phonon scattering in thin silica films below 1 k," *J. Low Temp. Phys.* **113**, p. 123, 1998.

[76] P. Jiang, L. Lindsay, X. Huang, and Y. K. Koh, "Interfacial phonon scattering and transmission loss in $> 1$ $\mu$m thick silicon-on-insulator thin films," *Phys. Rev. B* **97**, p. 195308, 2018.

[77] D. G. Cahill, P. V. Braun, G. Chen, D. R. Clarke, S. Fan, K. E. Goodson, P. Keblinski, W. P. King, G. D. Mahan, A. Majumdar, H. J. Maris, S. R. Phillpot, E. Pop, and L. Shi, "Nanoscale thermal transport. ii. 2003–2012," *Appl. Phys. Rev.* **1**, p. 011305, 2014.

[78] R.-P. Riwar, A. Hosseinkhani, L. D. Burkhart, Y. Y. Gao, R. J. Schoelkopf, L. I. Glazman, and G. Catelani, "Normal-metal quasiparticle traps for superconducting qubits," *Phys. Rev. B* **94**, p. 104516, 2016.

[79] R. J. Schoelkopf, P. Wahlgren, A. A. Kozhevnikov, P. Delsing, and D. E. Prober, "The radio-frequency single-electron transistor (rf-set): A fast and ultrasensitive electrometer," *science* **280**, p. 1238, 1998.

[80] Z. Hermon, E. Ben-Jacob, and G. Schön, "Charge solitons in one-dimensional arrays of serially coupled josephson junctions," *Phys. Rev. B* **54**, p. 1234, 1996.

[81] D. B. Haviland and P. Delsing, "Cooper-pair charge solitons: The electrodynamics of localized charge in a superconductor," *Phys. Rev. B* **54**, p. R6957, 1996.

[82] H. Shimada, S. Katori, S. Gandrothula, T. Deguchi, and Y. Mizugaki, "Bloch oscillation in a one-dimensional array of small josephson junctions," *J. Ahys. Soc. Jpn.* **85**, p. 074706, 2016.

[83] I. L. Ho, M. C. Lin, K. Aravind, C. S. Wu, and C. D. Chen, "Transport dynamics with alternate cooper-pair and quasiparticle tunnelings in one-dimensional charge josephson arrays," *J. Appl. Phys.* **108**, p. 043907, 2010.

[84] N. Vogt, R. Schäfer, H. Rotzinger, W. Cui, A. Fiebig, A. Shnirman, and A. V. Ustinov, "One-dimensional josephson junction arrays: Lifting the coulomb blockade by depinning," *Phys. Rev. B.* **92**, p. 045435, 2015.

[85] K. Cedergren, R. Ackroyd, S. Kafanov, N. Vogt, A. Shnirman, and T. Duty, "Insulating josephson junction chains as pinned luttinger liquids," *Phys. Rev. Lett.* **119**, p. 167701, 2017.

[86] H. Shimada and P. Delsing, "Current mirror effect and correlated cooper-pair transport in coupled arrays of small josephson junctions," *Phys. Rev. Lett.* **85**, p. 3253, 2000.

[87] H. Shimada, C. Ishida, and Y. Mizugaki, "Drag current reversal in capacitively coupled arrays of small josephson junctions," *Phys. Rev. Lett.* **109**, p. 196801, 2012.

[88] P. Ågren, K. Andersson, and D. B. Haviland, "Kinetic inductance and coulomb blockade in one dimensional josephson junction arrays," *J. Low Temp. Phys.* **124**, p. 291, 2001.

[89] T. Watanabe, Y. Mizugaki, and H. Shimada, "Long range current correlation for adjacent small josephson junction devices," *NTT. School and Symp. Nanoscale Transport and phoTonics 2019, Nov. 18-22, 2019*, p. PWE25, 2019.

[90] G. M. Kanyolo, K. Takeda, Y. Mizugaki, T. Kato, and H. Shimada, "Cooper-pair tunneling in small josephson junction arrays under radio-frequency irradiation," *J. Low Temp. Phys.***201**, p. 269, 2020.